2012

# Artificial Impedance Surfaces and Wire Media for Absorption and Cloaking

Yashwanth Reddy Padooru

# Artificial Impedance Surfaces and Wire Media for Absorption and Cloaking

By
Yashwanth Reddy Padooru

M. S., The University of Mississippi, University, MS, USA, 2009
B. Tech., Jawaharlal Nehru Technological University, Hyderabad, India, 2006

A Dissertation
Submitted to the Faculty
of The University of Mississippi
in Partial Fulfillment of the Requirements
for the Degree of Doctor of Philosophy
with a major in Engineering Science
in the School of Engineering

The University of Mississippi
December 2012

# ABSTRACT

The main objective of this dissertation is to investigate the ability of utilizing artificial impedance surfaces and wire media for absorption and cloaking applications. The dissertation includes two parts which focus on the electromagnetic wave propagation in absorbers formed by stacked metasurfaces and structured wire media, and electromagnetic wave interaction with the cylindrical cloaking structures.

In the first part, we propose a variety of physical systems that show multiband and wideband absorption properties in the microwave regime. For the multiband absorbers, we propose a simple analytical model to study the absorption properties. Further, using the same circuit model, the physical mechanisms of the observed behaviour is clearly explained in terms of the open/coupled Fabry-Pérot resonators. To design wideband absorbers, we first analyze a single-layer wire medium loaded with an arbitrary material (a thin copper patch with finite bulk conductivity and a graphene patch characterized by its complex surface conductivity) at one end and a ground plane at the other. Based on the properties of the single-layer structure (which acts as a narrowband absorber), we next propose a novel multilayered mushroom structure with thin resistive patches at the wire-medium junctions for wideband absorption. To characterize the wideband properties, here, we derive new additional boundary conditions and solve the scattering problem using an analytical model developed particularly for the problem at hand. We also show a methodology to design these absorbers and explain the wideband absorption mechanisms.

The second part focuses on the application of various metasurfaces for cloaking dielectric and conducting cylinders for plane-wave incidence and for line sources in close proximity. The cloaking mechanism is based on a mantle cloaking technique, wherein the scattered field produced by the object is cancelled by the cloak. The purpose of this work is to design the mantle cloaks using the metasurfaces, to render the objects invisible. The analysis here is carried out using a rigorous analytical model which employs the Lorenz Mie-scattering theory. Two-sided impedance boundary conditions are applied at the interface of the metasurfaces and analytical grid-impedance expressions derived for the planar cases have been successfully used in tailoring the

reactances of the cylindrical surfaces. Further, the analytical results presented in the dissertation are verified using the numerical simulations.

*This work is dedicated to my family.*

# ACKNOWLEDGMENTS

I express my deep sense of gratitude for my advisor Dr. Alexander B. Yakovlev for his constant support and advice in the completion of this work. This work wouldn't have been a reality without his support and encouragement. The discussions with him always provided me great motivation, and his physical view on research has made a deep impression on me.

I would like to thank Dr. George W. Hanson, Dr. Francisco Medina, Dr. Francisco Mesa, Dr. Allen W. Glisson, Dr. Andrea Alù, and Dr. Sunil Mathur for their valuable suggestions, fruitful discussions, and physical interpretations which triggered new ideas and always provided me an opportunity to learn more. Their feedback made papers more readable by an order of magnitude.

I would like to thank the committee members Dr. Atef Z. Elsherbeni, Dr. Mustafa Matalgah, Dr. Ramanarayanan Viswanathan, and Dr. Ajit Sadana for taking their time and serve as committee members in evaluating my dissertation.

I am thankful to the Graduate School at the University of Mississippi for granting me the Summer Graduate Research Assistantship. I acknowledge my colleagues Dr. Chandra S. R. Kaipa, Mr. Ahmed Khidre, Mr. Pai-Yen Chen, Dr. Xuan Hui Wu, Wei Huang for their helpful discussions during the course of my dissertation. I also would like to express my thanks to my friends: Naren, Phani, Sandeep, and Satya who have been extremely helpful and understanding.

I would also like to thank Intel Corporation for giving me an opportunity to work as a Graduate Technical Intern in their research labs.

Last but not the least, I am grateful to my parents and my family for all their support, patience and encouragement.

University, Mississippi — Yashwanth Reddy Padooru
December 2012

# TABLE OF CONTENTS

# List of Tables

# List of Figures

# List of Abbreviations

**ABCs** additional boundary conditions

**AMC** artificial magnetic conductors

**CA** circuit analog

**CCA** capacitive circuit absorber

**EBG** electromagnetic band gap

**FP** Fabry-Pérot

**FSS** frequency selective surface

**HIS** high impedance surface

**PEC** perfect electric conductor

**TEM** transverse electromagnetic

# CHAPTER 1

# INTRODUCTION

Artificial impedance surfaces or metasurfaces consisting of 1-D and 2-D periodic thin metallic elements or frequency selective surface (FSS) elements [1], have been of interest for almost half a century in the antenna and microwave community because of their broad range of applications in the area of military, radio, and satellite communications. With advancements in the fabrication technology of FSS elements, these elements have been used to realize many electromagnetic materials, including artificial magnetic conductors (AMC), electromagnetic band gap (EBG) structures, metamaterials, and other artificial materials. All these materials form building blocks in filters for plane waves, transmission lines, antenna reflectors, antenna ground planes, absorbers, invisibility cloaks, sensors, and other microwave and millimeter-wave devices.

In particular of interest are the electromagnetic absorbing structures, which have been studied for a long time due to their ability to reduce the radar cross-section (RCS) of an object at microwave frequencies. The conventional radar absorbers include Salisbury [2] and Jaumann [3] absorbers, which employ either one or more resistive sheets stacked over each other at a distance of a quarter wavelength (measured at the center frequency of the absorption band). However, due to relatively large thickness, these absorbers are inadequate in practical applications such as stealth

technology for aircraft, missiles, and other vehicles.

Recently, a renewed interest has arisen in designing electrically thin absorbers based on metamaterials [4–12] and high impedance surface (HIS) [13–16]. These structures are artificially engineered materials having various metallic inclusions with dimensions of order $\lambda/10 - \lambda/4$. In particular, the absorbers based on metamaterials can be scaled from microwave [4, 5] to terahertz [6–8], infrared [9, 10], and even to optical [11] regimes through careful design of the constituent inclusions.

The common feature of all of the above single-layer metamaterial and HIS absorbers is that they operate in a single narrow frequency band with high absorption at a specific frequency. One possible way to extend the bandwidth is to use Jaumann absorbers [3] mentioned above. Further improvement in the bandwidth of the Jaumann absorber can be achieved by replacing the homogeneous resistive sheets with lossy band-stop resonating frequency selective surfaces (FSS), resulting in circuit analog (CA) absorbers [1, 17]. However, these absorbers are not usually preferred for practical applications due to the large thickness of Jaumann absorbers and problems associated with the harmonics and anti-resonances of the lossy resonating FSS of the CA absorbers. In [18, 19] it was shown that the capacitive circuit absorber (CCA) method results in designs with large bandwidths and optimal thicknesses in comparison to the Jaumann and CA absorbers. This method is a modification of the CA absorber, wherein the lossy band-stop resonating FSS are replaced by the lossy low-pass FSS (e.g., square patch arrays), and the quarter-wavelength dielectric spacers are replaced by spacers with variable thicknesses. Most of the design procedures of the Jaumann and CA absorbers have been formulated for normal angle of incidence. Only a few design methods have been published considering oblique angle of incidence for different polarizations [20–22]. In [21, 22], absorbing structures based on single-layer mushroom HIS consisting of perfect electric conductor (PEC) patches placed

on top of a metal backed wire-medium slab have been considered. However, these designs behave as materials with a local response, and the absorption is due to a lossy dielectric slab [22] or a resistive sheet placed on top of the structure [21]. Also, in [22] it has been shown that the presence of vias enhances the absorption bandwidth for obliquely incident TM-polarized plane waves.

Also, recently, advantages of using thin metasurfaces has been extensively explored in the study of electromagnetic cloaking. In these studies, the authors utilize the concept of "cloaking by a surface" [23–25], wherein the scattering from a given object (such as planar dielectric slab, 2-D cylinder, and 3-D sphere, among others) is significantly reduced. This technique is based on the scattering cancellation properties of the mantle cloak (realized using an ultra thin conformal and patterned metasurface) characterized by a surface reactance. By adjusting the parameters of the metasurface inclusions, one can achieve the desired surface reactance, which effectively cancels out the scattering from a given object, thus reducing the overall visibility (or in other terms, it can be understood in the sense that the incident field induces currents on the mantle cloak which in turn generates anti-phase fields that cancels out the fields scattered by the object).

Most of the absorbers and the mantle cloaks mentioned above are analyzed using intense and time-consuming numerical simulations [26, 27], which do not provide enough physical insight into the problem. Recently, homogenization methods [28–32] have been proposed to avoid the extensive computations demanded by the numerical simulations. These methods are shown to be very effective in modeling the interaction of electromagnetic waves with artificial materials formed by lattices of periodic metallic or magneto-dielectric inclusions. Homogenization methods are applied when the size of the material inclusions is small compared to the wavelength of the incident wave. In such cases, the microscopic fluctuations are averaged out to obtain smooth

and slowly varying macroscopic quantities that can be used to characterize the long range variations of the electromagnetic waves [33].

In this work, we first start with the analysis of a single resistive sheet placed on top of a stacked metallic mesh/patch arrays and study the absorption mechanisms of the entire multilayer structure. The propagation characteristics are studied using circuit-like models clearly explaining the relevant physical mechanisms of the observed absorption resonances. The analytical expressions of the metasurfaces (sub-wavelength grids comprised of meshes/patches), are obtained from the full-wave scattering problem with the use of an averaged impedance boundary condition, expressed in terms of effective circuit parameters [34,35]. Then, we consider the case of the multilayer wire media loaded with resistive patch arrays and characterize the reflection properties of the entire multilayer structure using the analytical model developed particularly for this problem. Based on charge conservation, here, generalized additional boundary conditions (ABCs) are derived for the interface of two uniaxial wire mediums with thin imperfect conductors at the junction. The reflection properties are studied to show that in such configurations the presence of vias results in the enhancement of the absorption bandwidth and an improvement in the absorptivity performance for increasing angles of an obliquely incident TM-polarized plane wave. The results obtained using the analytical model are validated against full-wave numerical simulations [36].

Next, we study we study analytically mantle cloaks for cylindrical objects using various 1-D and 2-D sub-wavelength periodic FSS elements, such as strips [35], mesh grids and patches [34, 35, 37–39], Jerusalem crosses [40, 41], and cross dipoles [42]. Our method is still based on the mantle cloaking technique proposed in Refs. [23,24], however, here we use a rigorous analytical model to describe the surface impedance of the mantle cloaks. The analysis is based on Lorenz-Mie scattering theory [43], which

employs the two-sided impedance boundary condition applied on the surface of the FSS elements. The analytical expressions for the grid-impedances of the printed and slotted cylindrical FSS cloaks have been taken from the solution of the plane-wave problem derived for the planar sub-wavelength grids [34, 35]. This tremendously facilitates the design of cylindrical cloaks in realizing the required surface reactances, which can be used to reduce the overall scattering from a given object at the desired frequency of interest, and our results are accurately validated with full-wave simulations.

Further, we study a mantle cloaking of cylindrical objects coated with conformal metasurfaces due to an electric line source. The metasurface cloaks are formed by 2-D arrays of slotted (meshes and slot-Jerusalem crosses) and printed (patches and Jerusalem crosses) sub-wavelength frequency selective surface (FSS) elements. The electromagnetic scattering analysis is carried out using the analytical eigenfunction-expansion method which utilizes the two-sided impedance boundary conditions at the interface of the sub-wavelength elements. It is shown that the analytical expressions derived for the planar arrays of sub-wavelength elements may be successfully used to model and tailor the surface reactance of cylindrical conformal mantle cloaks even in a close proximity of the line source to a cloaked object. By proper tailoring of the surface reactance of the cloak, we demonstrate that the field radiated by the line source is almost unperturbed, rendering the object invisible over the range of frequencies of interest (i.e., at microwaves and far-infrared). The analytical model results presented throughout this work are validated using full-wave numerical simulations.

# CHAPTER 2

# CIRCUIT MODELING OF MULTIBAND HIGH-IMPEDANCE SURFACE ABSORBERS IN THE MICROWAVE REGIME

In this chapter we present a simple circuit model to study the absorption of electromagnetic waves by a multilayer structure with a high impedance surface in the microwave regime. The absorber consists of a stack of two-dimensional arrays of sub-wavelength meshes/patches separated by dielectric slabs and backed by a metallic ground plane, with a single resistive sheet placed on the top layer. It is observed the appearance of low-frequency resonances of total absorption, which have been identified as the resonances of Fabry-Pérot type associated with the individual reactively-loaded dielectric slabs (that are strongly coupled through the sub-wavelength grids). It is shown that these resonances lie within certain characteristic frequency band defined by the structural parameters of the absorber. The observed resonances are characterized by studying the electromagnetic field behavior using the circuit model and full-wave numerical program. In addition, we show that the patch array absorber

provides stable resonances with respect to the angle and the polarization of obliquely incident plane waves.

## 2.1 Introduction

Since the invention of the classical Jaumann and Salisbury absorbing structures (see, for a detailed historical review, the book on frequency selective surfaces by B. A. Munk [1]) there have been various absorbers invented, new concepts formalized, and advanced design procedures added to the existing ones. Even nowadays, there is a growing interest in the study of these structures, mainly in the physics community, due to its wide range of applications in the electromagnetic spectrum from microwave to optical frequencies.

In recent years, there has been a considerable interest in the enhancement of performance of absorbers using metamaterials [4, 7–12, 44], because of their peculiar properties not available in conventional materials. In Ref. [4] it has been shown that by using resonant elements (electric ring resonator backed by a cut wire) in the unit cell, absorption of nearly unity can be achieved at microwave frequencies. In that paper, the absorption is obtained by the appropriate choice of effective permittivity and effective permeability, such that the impedance of the absorber is matched to free space [4]. Based on this idea, other possibilities have been put forward to extend the designs to higher frequencies [7–11, 44], and for large incidence angles [7, 9–11, 44]. Also, electrically thin absorbers based on high-impedance surfaces (HIS) [13–16] have been introduced in the microwave regime. Following Ref. [13], an absorption resonance is achieved by combining the properties of the HIS with the absorption of a resistive sheet. In practice, the resistive sheet can be realized using commercially available resistive materials placed on the HIS [14] or with surface-mounted resistive

elements interconnecting the metallic parts of two-dimensional sub-wavelength elements [15, 16]. More recently, ultra-thin absorbers have been introduced, with losses either in the dielectric slab [22] or in the metallic elements of frequency selective surfaces [45, 46].

The common feature of all of the aforementioned absorbing structures is that they operate in a single narrow frequency band with high absorption at a specific frequency (independently of their specific operating frequency regimes). This fact limits their use in applications such as spectroscopic detection and identification of explosives, contaminations, and rare earth ions, which have distinct absorption features at multiple frequencies [47, 48]. To overcome these shortcomings, dual-band metamaterial absorbers [49,50] have been proposed. In these designs, the unit cells of the two single-band resonators were combined together to form a single unit cell with dual-band resonances. Although these absorbers show good absorptivity at dual frequencies, they operate only at the normal incidence of the impinging electromagnetic wave. Hence, wide angle and polarization insensitive multi-band absorbers with two or more absorption peaks are highly desirable.

In this work, we will use the idea of a single-band HIS absorber [13] adapted to a layered environment (with the geometry of a typical configuration shown in Fig. 2.1), and demonstrate that this structure (formed by a stack of 2-D sub-wavelength grid elements) exhibits multiple absorption peaks in the microwave regime. It is important to note that the absorption characteristics that we investigate here are quite different from those described in Refs. [49, 50], wherein the absorption resonances directly depend on the resonances of the unit-cell resonators. In order to achieve these multiple absorption peaks, the resonators in Refs. [49,50] had multiple resonant elements in the unit cell, which led to complex designs of the unit-cell geometry. By contrast, we explore here a completely different physical effect not directly related to

the resonances of the unit cell elements. Based on a circuit theory model, we demonstrate that the absorption resonances are of Fabry-Pérot (FP) type associated with the individual reactively-loaded dielectric slabs that are strongly coupled through the sub-wavelength grid/patch elements.

Circuit models have been used for a long time in the frame of electrical engineering practice with remarkable success. For instance, the problem of propagation of electromagnetic waves through wire media, which has been essential for the development of metamaterial science (wire media behaves as plasma with negative index of refraction at optical frequencies), was addressed several decades ago by using circuit analogies [51,52]. More recently, circuit models for analyzing HIS absorbers [21,22,46] have been proposed with the aim of avoiding the lengthy and cumbersome computations demanded by the numerical simulations. Indeed, problems closely related to the ones treated in this work have been analyzed following the circuit approach presented in Refs. [38, 53, 54]. Also, it should be mentioned that the circuit modeling can be used at optical frequencies [55], with the functionality of inductors, capacitors, and resistors realized using plasmonic and non-plasmonic nanoparticles. Apparently, this strategy, which is well known to the microwave and antenna engineers, has not spread enough among the optics community. Furthermore, since circuit models do not provide exact solutions, they have to be thoroughly validated in each new application, which motivates the study carried out in this work.

Thus, and due to the ease of implementation and direct connection with the physics of the problem, we explore the advantages of the circuit model to explain the absorptivity in multilayer HIS absorbers. The method of analysis is based on the circuit theory model of the stacked sub-wavelength grids [38], wherein the analytical expressions for the grid impedances (admittances) are obtained in terms of the effective circuit parameters from the full-wave scattering problem [34,35]. In this work we

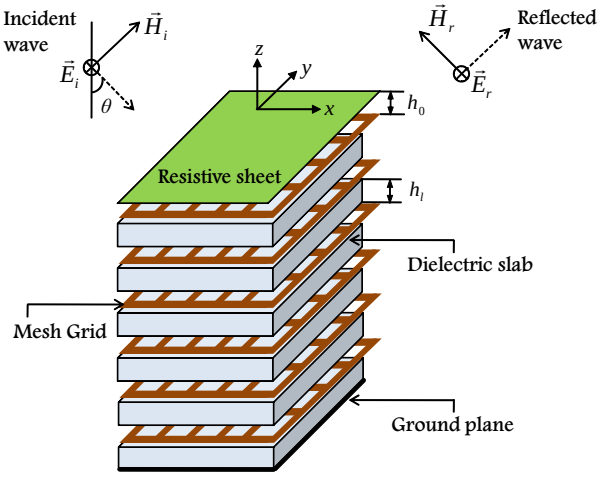


**Figure 2.1.** Exploded schematic of the multilayer HIS absorber formed by mesh grids of sub-wavelength dimensions.

add lumped resistors or a single resistive sheet on the top layer of a stack of grid/patch arrays, and study the absorption mechanisms of the entire multilayer structure. Due to a small electrical size of the unit cell, the grid provides a mechanism for the excitation of higher-order evanescent fields, which spread over a certain distance around the grid. However, if the distance between the adjacent grids is large enough (typically larger than the period of the unit cell), the higher-order mode interactions can be neglected, and the grids interact primarily through the single transverse electromagnetic transverse electromagnetic (TEM) mode. In such a situation, the circuit model gives fairly accurate results, as described in Ref. [38].

In particular, we concentrate on the case of a two-layer HIS formed by mesh grids without and with the resistive sheet, and relate the physical mechanisms of HIS and absorption resonances to the transmission resonances observed in a four-layer structure (without the ground plane) formed by the same mesh grids [38]. Even though the considered configuration is electrically thick when compared to the operating wavelength (greater than a quarter-wavelength in dielectric), we employ this example due to the similarities in the structure and the resonances studied in Ref. [38]. In that paper it has been demonstrated that the transmission spectra for each transmission

band have a number of peaks (as FP resonances) equal to the number of FP cavities (formed by reactively-loaded dielectric slabs). In a similar way, we show now that the multilayer mesh/patch grid absorbers exhibit the same kind of FP-like resonances. It is observed that the resonances of total absorption lie within a characteristic frequency band defined by the lower and upper band edges. These edge frequencies correspond to the first and the last resonance modes, and a comprehensive study of the electromagnetic field distribution associated with these resonances is provided using the circuit model and full-wave commercial solver HFSS [36]. Also, it is observed that the HIS absorber formed by mesh grids is sensitive to the angle and the polarization of the impinging plane waves. In order to overcome this problem, we present a multilayer HIS absorber formed by the patch arrays, with stable resonances for different incident angles and polarizations. In addition, we demonstrate that if a tunable resistive sheet with a wide range of admittance values is chosen, the multilayer patch array absorber is capable of absorbing the plane waves for large incident angles at multiple frequencies.

## 2.2 Circuit model analysis

Consider a plane wave incident on the multilayer HIS absorber as shown in Fig. 2.1. It is assumed that each dielectric layer is homogeneous and isotropic of thickness $h_l$, and characterized with relative permittivity $\varepsilon_l$, $l = 1, 2, ..., m$ and permeability of free space. Provided that for the frequencies of interest the interaction between the grids takes place through a single TEM mode, the circuit model shown in Fig. 2.2 gives an appropriate description of the system in Fig. 2.1. The shunt reactances $Y_{g1}, Y_{g2}, \ldots, Y_{gm}$ (grid admittances) account for the below-cutoff evanescent higher-order modes scattered by the metal grids in each layer. The lossy resistive sheet represented by an admittance $Y_R$, in parallel with the grid admittance $Y_{g1}$, is placed at

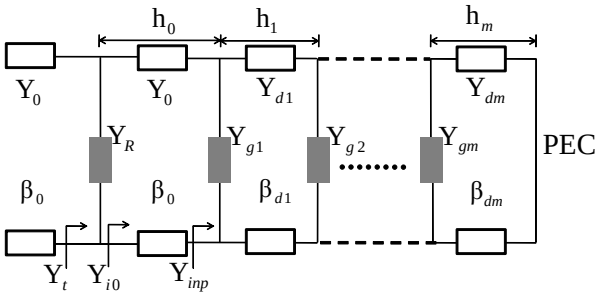


**Figure 2.2.** Transmission-line network for the multilayer structure with sub-wavelength periodic elements; $Y_0$, $\beta_0$ are the characteristic admittance and propagation constant of the air filled region; $Y_{dl}$ and $\beta_{dl}$ are the same parameters for the corresponding dielectric filled regions.

a distance $h_0$ from the multilayer structure. The medium between the resistive sheet and the multilayer structure is assumed to be free space. In practice, the distance $h_0$ is either zero or electrically small (which leaves an air gap). The parameters of the transmission line in Fig. 2.2, propagation constants $\beta_0$ for the air filled section and $\beta_{dl}$ for the dielectric filled sections, and the corresponding characteristic admittances $Y_0$ and $Y_{dl}$ are known in closed form. The expressions for these parameters for TE and TM polarizations are

$$\beta_0 = \frac{\omega}{c} \qquad \beta_{dl} = \beta_0\sqrt{\varepsilon_l - \sin^2\theta} \tag{2.2.1}$$

$$Y_0^{\mathrm{TE}} = Y_0\cos\theta \qquad Y_0^{\mathrm{TM}} = \frac{Y_0}{\cos\theta} \tag{2.2.2}$$

$$Y_{dl}^{\mathrm{TE}} = Y_0\sqrt{\varepsilon_l - \sin^2\theta} \qquad Y_{dl}^{\mathrm{TM}} = \frac{Y_0\,\varepsilon_l}{\sqrt{\varepsilon_l - \sin^2\theta}} \tag{2.2.3}$$

where $Y_0 = \sqrt{\varepsilon_0/\mu_0} \approx 1/377$ S is the intrinsic admittance of free space, $\theta$ is the incidence angle, $\omega$ is the angular frequency, and $c$ is the speed of light in vacuum. Since the size of the unit cell considered in this work is electrically small, accurate estimations for the grid admittances based on the dynamic solution for some periodic structures (patch arrays, mesh grids, among others) are available in the literature. Following Ref. [34], the mesh/patch grid behaves mainly as an inductive/capacitive

load, and the analytical expressions for grid admittance $Y_{gl}$ for TE and TM polarizations can be obtained as follows:

$$Y_{gl}^{\mathrm{TE}} = \frac{1}{j\omega L_{gl}^{\mathrm{TE}}} \quad , \quad L_{gl}^{\mathrm{TE}} = \frac{\eta_0 D}{2c\pi} \ln\Big[\csc\Big(\frac{\pi w}{2D}\Big)\Big] \tag{2.2.4}$$

$$Y_{gl}^{\mathrm{TM}} = \frac{1}{j\omega L_{gl}^{\mathrm{TM}}} \quad , \quad L_{gl}^{\mathrm{TM}} = \frac{\eta_0 D}{2c\pi} \ln\Big[\csc\Big(\frac{\pi w}{2D}\Big)\Big] \left(1 - \frac{\sin^2\theta}{2\varepsilon_l^{qs}}\right) \tag{2.2.5}$$

$$Y_{gl}^{\mathrm{TE}} = j\omega C_{gl}^{\mathrm{TE}} \quad , \quad C_{gl}^{\mathrm{TE}} = \tfrac{2D\varepsilon_l^{qs}}{c\eta_0\pi} \ln\big[\csc\big(\tfrac{\pi w}{2D}\big)\big] \left(1 - \tfrac{\sin^2\theta}{2\varepsilon_l^{qs}}\right) \tag{2.2.6}$$

$$Y_{gl}^{\mathrm{TM}} = j\omega C_{gl}^{\mathrm{TM}} \quad , \quad C_{gl}^{\mathrm{TM}} = \frac{2D\varepsilon_l^{qs}}{c\eta_0\pi} \ln\Big[\csc\Big(\frac{\pi w}{2D}\Big)\Big] \tag{2.2.7}$$

where csc stands for the co-secant function, $\eta_0 = \sqrt{\mu_0/\varepsilon_0} \approx 377\,\Omega$ is the intrinsic impedance of free space, $\varepsilon_l^{qs} = (\varepsilon_l + \varepsilon_{l+1})/2$ for interior grids ($l = 2, 3, ....., m-1$) and $\varepsilon_l^{qs} = (\varepsilon_l + 1)/2$ for the grid located at the upper interface ($l = 1$). The geometrical parameters $D$ and $w$ of the inductive/capacitive grid are defined in Fig. 2.3(b) and Fig. 2.12(b) in the sections to follow.

It is well known that for a HIS structure [56, 57](single-band or multi-band) at resonance, the surface admittance is zero, resulting in a zero reflection phase. In Fig. 2.2, $Y_{\mathrm{inp}}$ corresponds to the input admittance of the HIS structure. Hence, at resonance $Y_{\mathrm{inp}}$ is zero and the admittance of the open-circuit termination of the air-gap section (for small $h_0$) is given by

$$Y_{i0} = \mathrm{j} Y_0 \tan\beta_0 h_0 \approx 0\,. \tag{2.2.8}$$

Thus, the total surface admittance $Y_t$ of the HIS absorber is equal to admittance of the resistive sheet $Y_R$. If $Y_R$ is chosen in such a way that, $Y_R = Y_0^{\mathrm{TE,TM}}$ ($Y_0^{\mathrm{TE,TM}}$ are given in Eq. 2.2.2), then the admittance of the structure is matched to the intrinsic admittance of free space. Under this condition, the incident field is absorbed by the structure and we have reflection nulls ($S_{11} = 0$) or absorption peaks ($\mathcal{A} = 1 - S_{11}^2$).

Since the system is backed by a perfect electric conductor (PEC), no transmission is possible ($S_{12} = 0$) and thus the total incident energy is absorbed by the resistive sheet and dissipated as heat. In practice, dielectric slabs and metal grids have small losses and absorb a fraction of the incident energy.

In general, the formalism of the circuit model presented here can be directly applied to the analysis of wideband absorption properties of multilayer structures with dielectric slabs of different thicknesses and permittivities, and arbitrary sub-wavelength resistive grids (*e.g.*, patch arrays, Jerusalem cross arrays, and others) with the analytical expressions for the grid admittance/impedance available in the literature. [34, 40] However, in this work we focus our attention on the study of FP-type resonances in multilayer structures with identical grids and identical dielectric slabs.

## 2.3 Mesh grid absorbers

In this section, the absorption properties of the multilayer HIS absorbers formed by mesh grids are analyzed using the circuit model formalism given in Section 2.2. Specifically, we study the two-layer mesh grid absorber in order to explain the physical mechanisms of the resonances based on the resonant field behavior using the circuit model and numerical solutions. The resonances corresponding to the lower/upper frequency band edges of the absorption band in a multilayer configuration are explained in terms of the finite number of strongly coupled FP cavities.

### 2.3.1 Two-Layer Mesh Grid Absorber

The absorber (shown in Fig. 2.3) is composed of two identical mesh grids printed on two identical dielectric slabs, with a resistive sheet placed on the top and a PEC ground plane at the bottom. Each mesh grid has the period $D = 5\,\text{mm}$ and strip

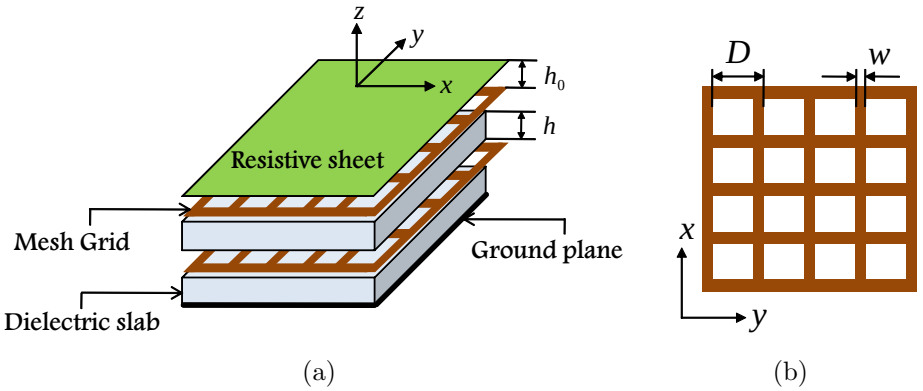


**Figure 2.3.** (a) Exploded schematic of the two-layer mesh grid separated by dielectric slabs, with a resistive sheet placed on the top and a PEC ground plane at the bottom. (b) Top view of mesh grid.

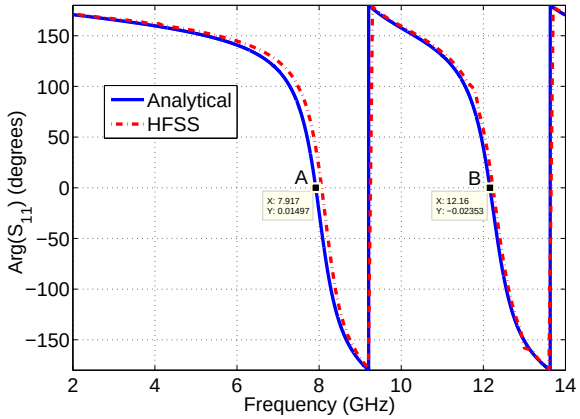


**Figure 2.4.** Reflection phase behavior of the two-layer mesh structure in the absence of resistive sheet, calculated using the circuit model and HFSS.

width $w = 0.15\,\text{mm}$, and each dielectric slab is of thickness $h = 6.35\,\text{mm}$ with relative permittivity $\varepsilon = 3$. The admittance of the resistive sheet $Y_R$ is chosen to be approximately $1/377\,\text{S}$ (for the normal plane-wave incidence). Since for the frequencies of interest (1-20 GHz), the period of the unit cell $D$ is meaningfully smaller than $\lambda_0$ and the separation between the successive grids $h > D$ (higher-order interactions are negligible), the simple circuit model shown in Fig. 2.2 is appropriate for our analysis purposes. Consider the structure shown in Fig. 2.3 without the resistive sheet, and assume that it acts as a HIS at resonance ($Y_{\text{inp}} = 0$), reflecting the incident field

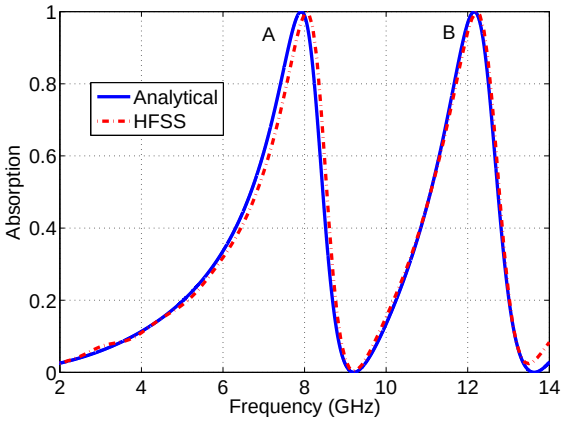


**Figure 2.5.** Absorptivity of the two-layer HIS absorber as a function of frequency, calculated with the circuit model and HFSS.

with zero reflection phase. Since the HIS is impenetrable, in the absence of losses its reflectance is equal to unity. The circuit model results (termed as "Analytical" in the figures) for the reflection phase characteristics of the HIS structure are shown in Fig. 2.4 for the case of normal incidence. These results show a very good agreement with the HFSS results also shown in the figure. Since the lattice in this work is square, the mesh grid (as well as patch grid) is symmetric under rotation of 90 degrees and, therefore, the effective grid admittance (understood in the sense of homogenization) is the same for normal incidence for both TE and TM polarizations, independent of the polarization angle. In Fig. 2.4, it can be observed that the structure has two resonances at 7.917 GHz and 12.16 GHz corresponding to the zero reflection phase, labeled as A and B. It is interesting to note that the HIS structure is equivalent to the antisymmetric excitation (associated with placing a PEC wall in the middle) of the geometry analyzed in Ref. [38]. Thus, following Ref. [38], we have two FP cavities that are strongly coupled through the square holes of each grid; *i.e.*, two reactively loaded dielectric slabs. Also, the observed resonances A and B have the same physical nature as the resonances B and D in the four-layer structure formed with five identical mesh grids in Ref. [38] with the resonance frequencies of 8.06 GHz

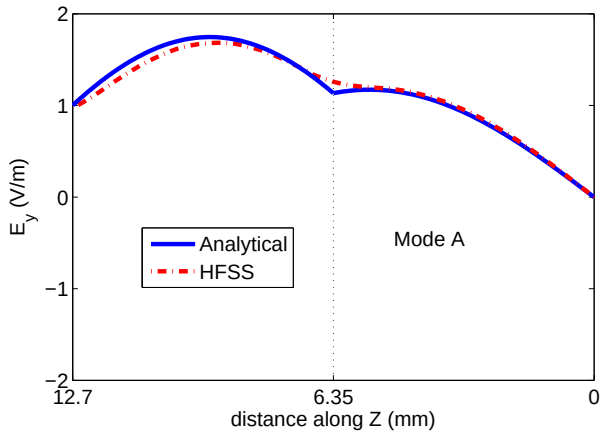


(a)

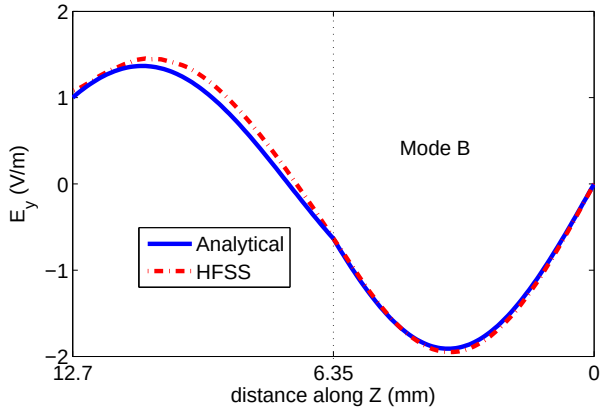


(b)

**Figure 2.6.** Comparison of the analytical and HFSS results of the electric field distributions in the two-layer HIS mesh grid absorber for (a) mode A and (b) mode B. HFSS results are obtained by calculating the field along a line in the *z*-direction through the center of the holes.

and 12.2 GHz, respectively. Now, consider a resistive sheet ($Y_R \approx 1/377\,\mathrm{S}$) placed in a close proximity to the HIS structure. The distance $h_0$ is assumed to be small (air gap of 0.1 mm thickness is used) so that the effect of the air gap can be neglected. In such a case, the structure still retains the same FP-like resonances A and B, however, there is no reflection because of the perfect match of the surface admittance ($Y_t$, in Fig. 2.2) of the absorber to free space. Fig. 2.5 shows the predictions of the analytical model for the case of normal incidence. It is seen that the results of the circuit model

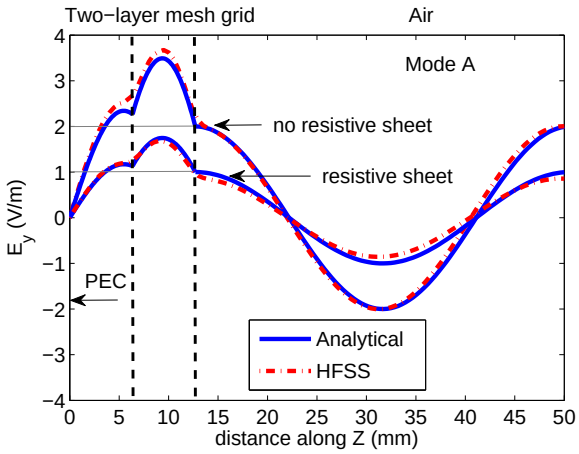


(a)

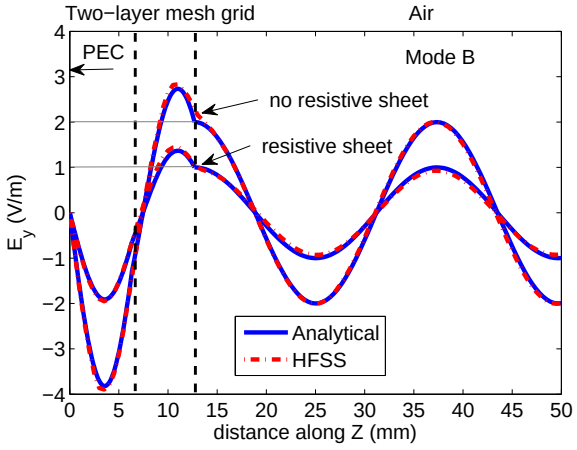


(b)

**Figure 2.7.** Total electric field distributions of the two-layer mesh grid structure with and without the resistive sheet for (a) mode A and (b) mode B. The dotted vertical lines denote the position of the mesh grids.

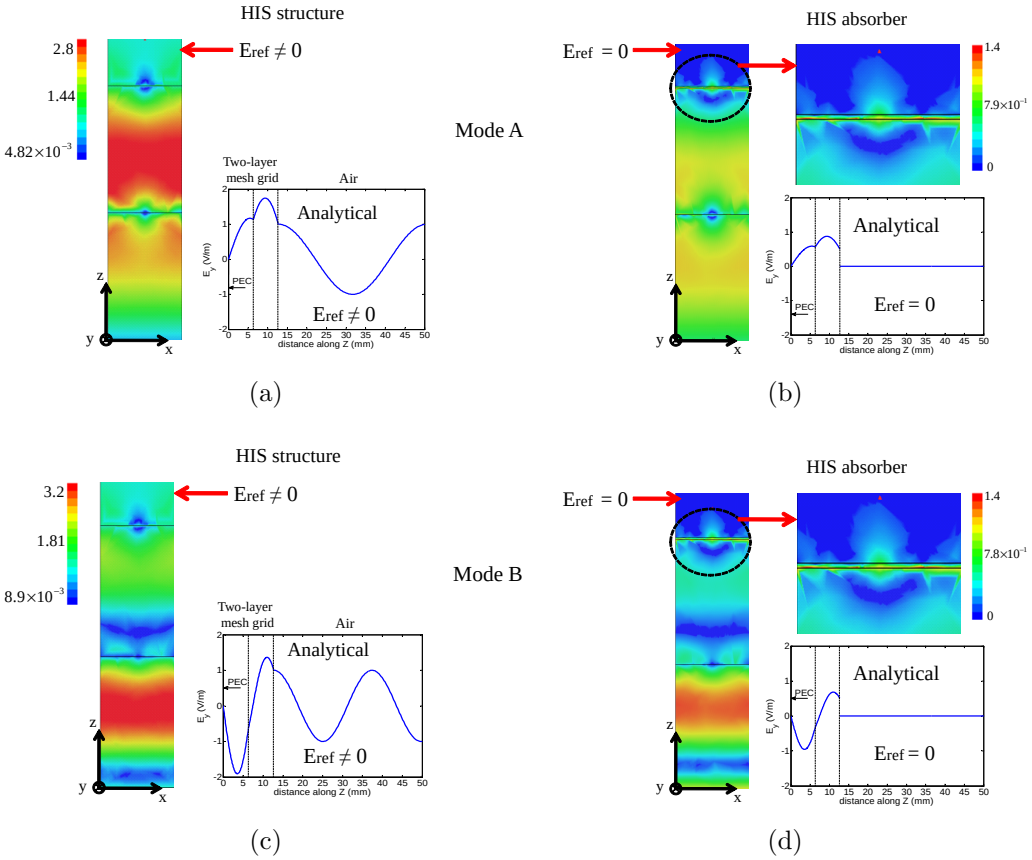


**Figure 2.8.** Reflected electric field distributions of the two-layer mesh grid structure: (a) mode A without the resistive sheet, (b) mode A with the resistive sheet, (c) mode B without the resistive sheet, and (d) mode B with the resistive sheet.

are again in good agreement with the HFSS results. It is worthy to point out that, in the two-layer HIS absorber and the one studied in Ref. [38], the corresponding resonances of absorption and transmission are associated with the perfect match of the surface admittance to the intrinsic admittance of free space. Hence, it is important to verify the field distributions at the resonance frequencies, and at the same time compare the predictions of the circuit model with HFSS.

The electric field distributions based on the results of the circuit model and HFSS, corresponding to the two resonance modes (A and B) of the absorption band are shown in Fig. 2.6. Circuit model results are in a good agreement with the numerical results, which shows that our model captures the electromagnetic details of the structure. For the field distributions corresponding to the first resonance (mode A), there is no low value of the electric field near and over the internal grid, and also the fields in the dielectric layers are in phase with each other. By contrast, for the second resonance (mode B), the field value is relatively low over the internal grid, and the fields in the dielectric layers are out of phase. Also, the observed field distributions in Fig. 2.6 have the same qualitative behavior as the fields in the first two layers (modes B and D) in Ref. [38]. However, in Ref. [38], the dominant TEM mode is transmitted through the structure for the modes B and D (which correspond to transmission peaks), and in the case of a two-layer absorber it is absorbed by the resistive sheet for the modes A and B (absorption peaks).

To understand the physics of absorption in the two-layer HIS absorber (shown in Fig. 2.3), in Fig. 2.7 we compare the total electric field distributions of the HIS structure, with/without the resistive sheet at normal incidence, for the resonant modes using the circuit model and HFSS. The fields are calculated inside the cavities and in the air regions to explain how these structures interact with the incident plane

wave (with the electric field of magnitude 1 V/m peak-to-peak (p-p)). The first observation that can be drawn from Fig. 2.7 is that the field distributions predicted by the circuit model agree well with HFSS. Slight disagreements are expected around the grid positions, because the analytical model calculates the "macroscopic" field (average field over the period), and the HFSS provides the "microscopic" field (near field at each point) of the transverse electromagnetic waves. However, the microscopic and macroscopic fields are comparable for the sub-wavelength mesh grids. [38] The position of the mesh grids are shown by the vertical dotted lines. It can be observed that the field values for the two modes are meaningfully larger in the absence of the resistive sheet, as expected. This is because at resonance, the HIS reflects the field with zero reflection phase ($S_{11} = +1$), and the total electric field is equal to twice the incident field (note that $E_y = 2\,\mathrm{V/m}$ at $z = 12.7\,\mathrm{mm}$). However, in the presence of the resistive sheet the reflected field is absorbed and dissipated as heat, and the total electric field is equal to the incident field (in the air region). It should be noted that for the HIS structure with/without the resistive sheet the fields (incident and reflected) inside the cavities add in phase. Next we study the behavior of the re-

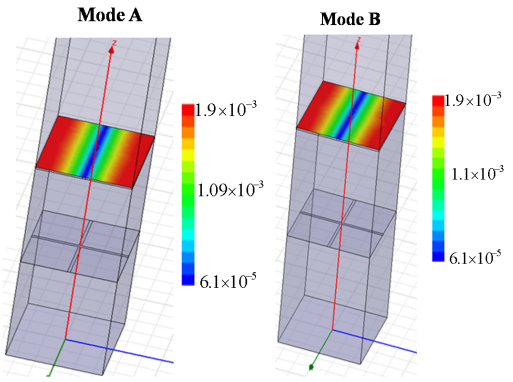


**Figure 2.9.** Simulation results of the surface loss density of the two-layer mesh grid HIS absorber, calculated using HFSS for (a) mode A and (b) mode B.

flected electric field for the modes A and B of the HIS structure (without the resistive sheet) and the absorber (with the resistive sheet). The full-wave simulation results are shown in Fig. 2.8 for the case of normal incidence. In the absence of the resistive sheet, it can be observed from Figs. 2.8(a) and 2.8(c), that the reflected field for the resonance modes A and B is quite significant in the air region. As expected, a region of zero field is observed in the air region in the presence of the resistive sheet as shown in Figs. 2.8(b) and 2.8(d). Since there is no reflected field in the air region, the fields are trapped inside the structure. With the resistive sheet being the only lossy part in the system, it completely absorbs the total (incident and reflected) field. This is shown in Figs. 2.8(b) and 2.8(d) (magnified panels), where a strong concentration of the fields in the region close to the resistive sheet is observed.

In order to further validate this point, we calculate the surface loss density of the resistive sheet for the two resonance modes using full-wave simulations, shown in Fig. 2.9. Due to finite resistivity of the sheet, the surface currents induce resistive losses in the sheet, resulting in the power dissipated as heat.

### 2.3.2 Multilayer Mesh Grid Absorber

In the previous example it has been shown that the two-layer HIS absorber exhibits two FP-like resonances of complete absorption corresponding to the two FP cavities. It is then convenient to study the characteristics of the absorption band and its dependence on the structural parameters. For this purpose we apply the circuit model to study the absorption characteristics in structures formed by a large number of identical layers (mesh grids and dielectric slabs). We consider the field distributions corresponding to the first and the last resonance frequencies since the frequencies related to the lower and upper band edges define the absorption band. It should be noted that non identical dielectric slabs (with a proper choice of permittivity

and thickness) can be used in order to achieve the wide-band, band-pass, and band-stop absorption characteristics. This type of structures have potential applications as multi-band absorbers and filters, although their study is beyond the scope of the present work. Figure 2.10 shows the absorption characteristics of a ten-layer absorber

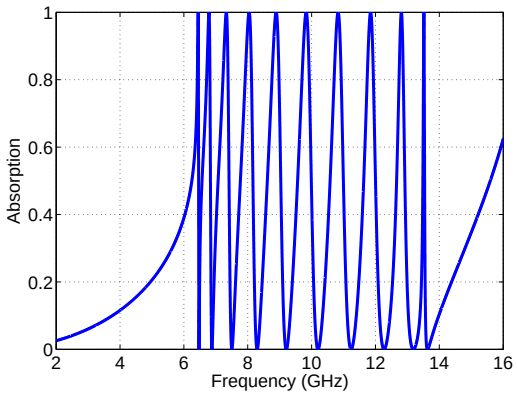


**Figure 2.10.** Analytical results of the absorption in the ten-layer HIS mesh grid absorber at normal incidence.

and all the peaks are within the characteristic frequency band. The absorber is formed by a stack of ten identical mesh grids printed on ten identical dielectric slabs (with the same geometrical dimensions used in the previous example) with a resistive sheet placed on the top and with the last dielectric slab backed by a PEC ground plane. In Fig. 2.10 it can be observed that there are ten peaks (resonances) of absorption (corresponding to the ten FP cavities), with all the peaks within the characteristic frequency band. It should be noted that, with an increase in the number of identical layers, the number of absorptions peaks is equal to the number of dielectric slabs. Also, there are no significant changes in the frequencies corresponding to the lower and the upper resonances of the absorption band with a large number of layers. The frequencies corresponding to the first ($f_{\mathrm{LB}}$) and the last ($f_{\mathrm{UB}}$) resonances for a different number of layers are given in Table 2.1. The field distributions corresponding to the lower/upper frequency band edge of a ten-layer structure are shown in Fig. 2.11.

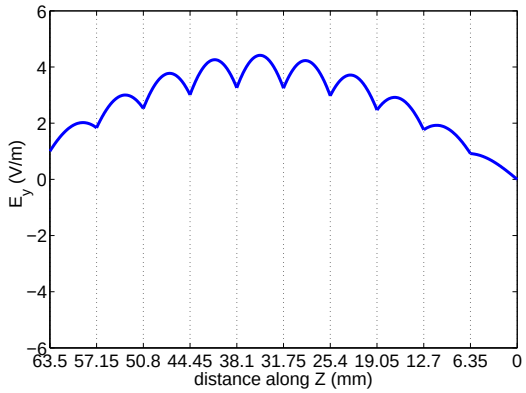


(a)

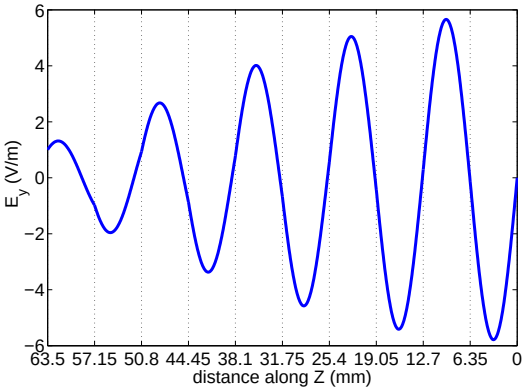


(b)

**Figure 2.11.** Analytical results of the field distributions in the ten-layer HIS mesh grid absorber for (a) first resonance mode and (b) last resonance mode.

**Table 2.1.** Frequencies of the lower and upper band edges with respect to the number of layers.

| No. of Layers | $f_{\mathrm{LB}}$ (GHz) | $f_{\mathrm{UB}}$ (GHz) |
|---|---|---|
| 2 | 7.917 | 12.16 |
| 5 | 6.713 | 13.25 |
| 10 | 6.447 | 13.52 |
| 20 | 6.363 | 13.60 |
| 30 | 6.347 | 13.62 |

Interestingly, the field distributions corresponding to the first and the last resonances are of the same qualitative behavior of the two-layer structure (modes A and B, as shown in Fig. 2.6), irrespective of the number of layers. For the field distribution corresponding to the first resonance, the fields in the successive layers are in phase, and there is a significant contribution from the grids. This means that the frequency corresponding to the lower band edge is dependent on the dimensions of the mesh grid. However, for the field distribution corresponding to the last resonance, the fields in the adjacent layers oscillate out of phase, with no significant contribution from the mesh grids. The frequency corresponding to the upper band edge is equal to the FP condition [58] (half-wavelength) of a single dielectric layer, [38] and is largely independent on the grid. It should be noted that a similar type of field behavior has been observed in Ref. [38], where the analytical expressions for the lower and upper transmission peaks based on the analysis of an infinite structure have been presented.

## 2.4 Patch array absorber

### 2.4.1 Normal incidence

Here we consider a multilayer HIS patch absorber as shown in Fig. 2.12. The structure is formed with identical patch arrays separated by dielectric slabs on a PEC ground plane, with a resistive sheet placed on the top. The analysis is carried out using the

circuit model formalism given in Section 2.2, with the appropriate grid admittance for the patch array given by Eqs. 2.2.6 and 2.2.7 for TE and TM polarizations, respectively. In the previous section, it has been shown that the multilayer mesh grid

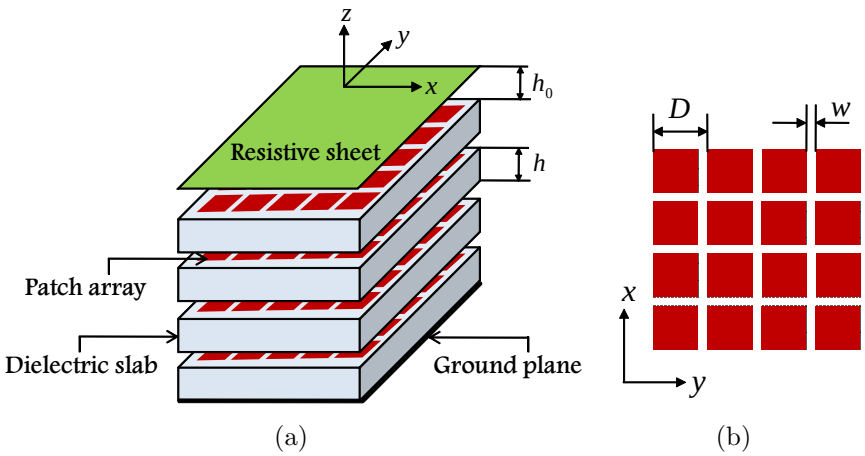


**Figure 2.12.** Exploded schematic of the mutlilayer patch array HIS absorber. (a) 3D view and (b) Top view showing the unit cell dimensions of the patch array.

absorbers exhibit multiple FP-like resonances that lie within a characteristic frequency band. A similar phenomenon is observed in the present case of multilayer HIS patch absorber, with the fields in the dielectric layers coupled through the capacitive grids.

Figure 2.13 shows the analytical results of the absorption characteristics for a ten-layer HIS patch grid absorber formed by ten identical patch grids printed on the corresponding dielectric layers. Each patch array has the period $D = 2\,\text{mm}$ and the gap $w = 0.2\,\text{mm}$, and each dielectric slab is of thickness $h = 2\,\text{mm}$ with relative permittivity 10.2. The admittance of the resistive sheet is chosen to be $1/377\,\text{S}$ for normal incidence. It can be observed that there are ten peaks of complete absorption corresponding to the ten layers (cavities) in the system. The resonance frequencies corresponding to the lower and the upper band edge for a different number of layers are given in Table 2.2. The table shows that with an increase in the number of layers,

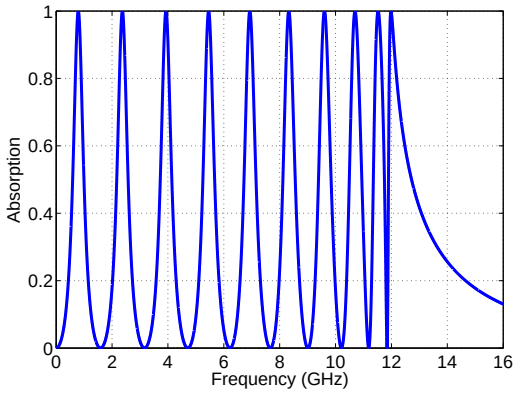


**Figure 2.13.** Analytical results of the absorption peaks in a ten-layer HIS patch absorber at normal incidence.

the lower band edge frequency decreases and the upper band edge frequency remains almost the same. It should be noted that if an infinite number of layers is considered along the $z$-direction (as it was done in Ref. [38]) and the resulting periodic structure is analyzed, then the mesh-loaded slabs behave as a pass-band structure while the patch-loaded slabs behave as a low-pass filter. This is the reason why the first resonance in the patch-loaded structure tends to zero frequency as the number of layers is increased. It is also possible to achieve higher-order pass-bands for the patch-loaded periodic structure. An interesting practical consequence of this behavior is that the first resonance can be tuned to very low frequencies, with the overall thickness of the structure still being electrically small. This is not possible when meshes are used. Also, it is interesting to see that the field distribution for the first resonance in the patch-loaded slabs is extremely smooth (shown in Fig. 2.14(a)) when compared with the ripples appearing in the similar plot for the mesh-loaded slabs (shown in Fig. 2.11(a)). This difference in the field behaviors could be attributed to the fact that the perturbation introduced by the patches is much stronger than the perturbation introduced by the meshes. The electric field distributions corresponding to the first and last resonance modes of the ten-layer structure are shown in Fig. 2.14. The

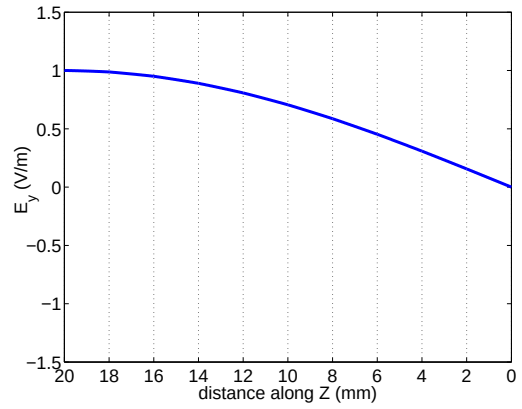


(a)

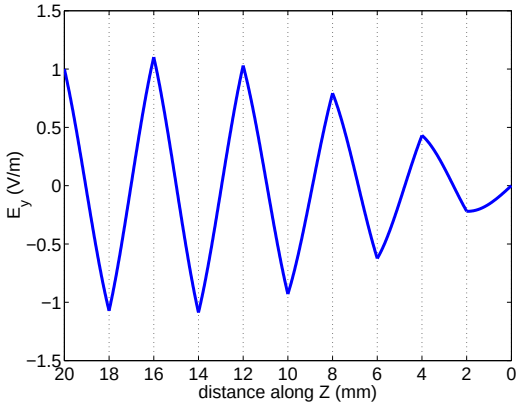


(b)

**Figure 2.14.** Analytical results of the field distributions in the ten-layer HIS patch absorber for (a) first resonance mode and (b) last resonance mode.

analytical results shown in the figure are the averaged fields per period of the patch array (macroscopic fields). It is observed that these resonance modes have the same qualitative behavior for any number of layers. The field distribution corresponding to the first resonance mode is nearly a quarter-wavelength in the entire multilayer configuration. Also, it is seen that this field distribution is of the same qualitative nature associated with the first resonance of the ten-layer structure without the internal patch grids; *i.e.*, the first mode is largely independent of the patch grids. For the last resonance mode the field distribution in each layer (except for the last two layers) is

**Table 2.2.** The lower and upper band edge frequencies with respect to the number of layers.

| No. of Layers | $f_{\mathrm{LB}}$ (GHz) | $f_{\mathrm{UB}}$ (GHz) |
|---|---|---|
| 2 | 3.89 | 10.56 |
| 5 | 1.57 | 11.77 |
| 10 | 0.79 | 11.98 |
| 25 | 0.32 | 12.06 |
| 30 | 0.26 | 12.06 |

nearly a half-wavelength with the electric field crossing the null at the middle of the layer, as shown in Fig. 2.14(b). This resonance is understood as the FP resonance associated with the single cavity (reactively loaded dielectric slab), and is dependent on the choice of the dielectric and patch grid parameters.

### 2.4.2 Oblique incidence

Now we consider the absorption characteristics of the two-layer HIS patch absorber (with the same dimensions used in the previous example) for oblique angles of incidence and different polarizations. The analytical results predict two absorption peaks as shown in Fig. 2.15. It can be observed that there is no significant change in the

**Table 2.3.** Absorptivity ($\mathcal{A}$) as a function of the incident angle and polarization.

| $\theta$ (degrees) | Mode A (GHz) | Mode B (GHz) | $\mathcal{A}$ |
|---|---|---|---|
| TE 0 | 3.88 | 10.55 | 1 |
| TE 30 | 3.93 | 10.66 | 0.99 |
| TE 60 | 4.01 | 10.88 | 0.88 |
| TM 0 | 3.88 | 10.55 | 1 |
| TM 30 | 3.93 | 10.69 | 0.99 |
| TM 60 | 4.03 | 10.96 | 0.88 |

resonance frequencies of the two absorption peaks with the increase in the incidence angle for both polarizations. The reason for the stable resonances can be attributed to the choice of a patch array printed on an electrically thin high-permittivity substrate,

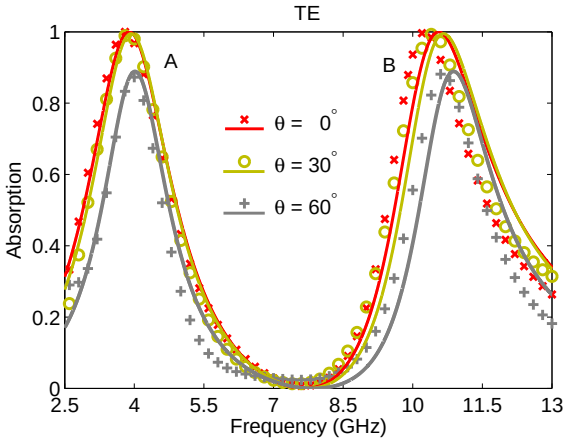


(a)

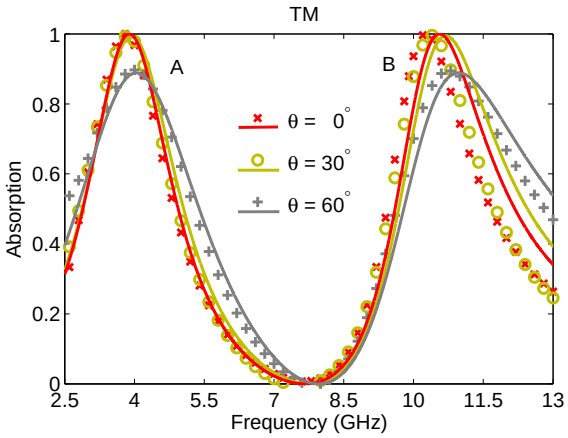


(b)

**Figure 2.15.** Comparison of analytical (solid lines), and full-wave HFSS results (crosses, circles, and plus signs) of absorption for the two-layer patch array HIS absorber at oblique angles of incidence $\theta$, for (a) TE polarization and (b) TM polarization.

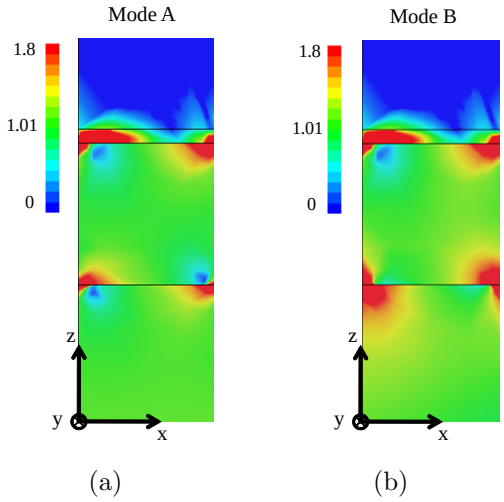


**Figure 2.16.** HFSS results of the reflected field distributions of a two-layer HIS patch absorber for the case of a TM-polarized plane-wave incident at 60 degrees: (a) first resonance mode and (b) second resonance mode.

as reported in Ref. [22]. The explanation offered in Ref. [59] for an angle-independent response could also be used here because the normal polarizability in this structure is negligible in comparison with the tangential polarizability of the patches. However, the surface admittance of the absorber is not perfectly matched to free space at oblique incident angles, thus reducing absorptivity. The values of the absorptivity and resonance frequencies with respect to the incidence angle for both polarization are given in Table 2.3. It should be noted that the two-layer mesh grid absorber studied in Sec. 2.3.1 is electrically thick, and because of the choice of a low dielectric constant it was observed that it is sensitive to the angle and polarization of the impinging plane wave (these results were omitted for the sake of brevity). The alternative explanation given in Ref. [59] is also valid in this case. Total absorption peaks for different polarizations of obliquely incident plane waves can be achieved by employing a tunable resistive sheet. The idea here is to adjust the admittance of the resistive sheet ($Y_R$) in accordance to the admittance of free space for oblique incident angles of TE- and TM-polarized plane waves (given in Eq. 2.2.2). For instance, to

achieve the unity absorption peaks the resistive sheet of the two-layer absorber is adjusted to the value of 1/188.5 S, for the case of a TM-polarized plane wave incident at 60°. Specifically, we have calculated the reflected electric field distributions for the two resonance modes (with the resonance frequencies of 4.03 GHz and 10.96 GHz) of the absorber, and the full-wave simulations are shown in Fig. 2.16. It can be observed that there is no reflected field in the air region (above the resistive sheet) and the field is confined to the absorber.

## 2.5 Conclusion

In this work a simple circuit model has been applied to the analysis of the absorption properties of multilayer structures with sub-wavelength dimensions in the microwave regime. The results obtained by this method are in complete agreement with the numerical simulations. It is observed that at low frequencies the resonances of complete absorption occur, and it is shown that these resonances are of FP type corresponding to the strongly coupled individual reactively-loaded dielectric slabs. The observed resonances have been characterized by studying the electromagnetic field behavior using the circuit model and numerical simulations. For the case of a fishnet absorber, it has been noticed that the number of peaks in the absorption band is equal to the number of dielectric slabs, and all the peaks are within a characteristic frequency band. The lower and upper band edges of the absorption band are explained in terms of the series of strongly coupled FP cavities, and is shown that these band edges are largely independent on the overall length of the structure.

In addition, we show that a two-layer absorber formed by printing patch arrays on an electrically thin high-permittivity substrate is insensitive to the angle and the polarization of the impinging plane wave. Also, it is shown that total absorption for oblique incidence can be achieved by using a tunable resistive sheet.

# CHAPTER 3

# NEW ABSORBING BOUNDARY CONDITIONS AND ANALYTICAL MODEL FOR MULTILAYERED MUSHROOM-TYPE METAMATERIALS: APPLICATIONS TO WIDEBAND ABSORBERS

An analytical model is presented for the analysis of multilayer wire media loaded with 2-D arrays of thin material terminations, characterized in general by the complex surface conductivity. This includes the cases of resistive, thin metal, or graphene patches and impedance ground planes. The model is based on the nonlocal homogenization of the wire media with additional boundary conditions (ABCs) at the connection of thin (resistive) material. Based on charge conservation, new ABCs are derived for the interface of two uniaxial wire mediums with thin imperfect conductors at the junction. To illustrate the application of the analytical model and to validate the new ABCs, we characterize the reflection properties of multilayer absorbing structures. It is shown that in such configurations the presence of vias results in the enhancement

of the absorption bandwidth and an improvement in the absorptivity performance for increasing angles of an obliquely incident TM-polarized plane wave. The results obtained using the analytical model are validated against full-wave numerical simulations.

## 3.1 Introduction

In recent years, characterization of metamaterial structures that constitute wire media has attracted special attention, due to their ability in enabling anomalous phenomena such as negative refraction [60,61] and sub-wavelength imaging [62,63], among others. However, it has been recently shown in [64] that wire media exhibits strong spatial dispersion at microwave frequencies, and that the constitutive relations between the macroscopic fields and the electric dipole moment are non-local [43]. In [65–68], the role of spatial dispersion has been discussed, and it was demonstrated that nonlocal homogenization methods with additional boundary conditions become essential in solving the reflection and transmission problems associated with wire media. Spatially dispersive materials have some advantages that can be successfully exploited for imaging with super resolution [62] and the realization of impedance surfaces [65], among others. However, they can be ineffective for certain applications involving negative refraction [69].

Recently, mushroom structures composed of metallic patches have been shown to suppress (or significantly reduce) spatial dispersion in wire media [70–73]. This is because the presence of metallic patches at the wire ends diminishes charge buildup in such a way that, upon homogenization, the mushroom structure can be treated as a uniaxial continuous Epsilon-Negative (ENG) material loaded with a capacitive grid of patches. However, this is not the case when the patches are thin (resistive), where charge accumulation and diffusion at the wire-to-patch interface becomes important,

and spatial dispersion effects have to be considered, necessitating an additional boundary condition at this interface [74]. Upon homogenization, these charge effects are reflected in the nonlocal slab permittivity.

It is also observed that for some specific values of the thickness (or resistivity) of the thin material patch, the structure acts as an absorber for obliquely incident TM-polarized plane waves. Electromagnetic absorbing structures have been of interest for a long time due to their ability to reduce the radar cross-section (RCS) of an object at microwave frequencies. The conventional radar absorbers include Salisbury [2] and Jaumann [3] absorbers, which employ either one or more resistive sheets stacked over each other at a distance of a quarter wavelength (measured at the center frequency of the absorption band). However, due to relatively large thickness, these absorbers are inadequate in practical applications such as stealth technology for aircraft, missiles, and other vehicles.

Recently, a renewed interest has arisen in designing electrically thin absorbers based on metamaterials [4–12] and high impedance surfaces (HIS) [13–16]. These structures are artificially engineered materials having various metallic inclusions with dimensions of order $\lambda/10 - \lambda/4$. In particular, the absorbers based on metamaterials can be scaled from microwave [4, 5] to terahertz [6–8], infrared [9, 10], and even to optical [11] regimes through careful design of the constituent inclusions.

The common feature of all of the above single-layer metamaterial and HIS absorbers is that they operate in a single narrow frequency band with high absorption at a specific frequency. One possible way to extend the bandwidth is to use Jaumann absorbers [3] mentioned above. Further improvement in the bandwidth of the Jaumann absorber can be achieved by replacing the homogeneous resistive sheets with lossy band-stop resonating frequency selective surfaces (FSS), resulting in circuit analog (CA) absorbers [1, 17]. Also in [18, 19] the capacitive circuit absorber

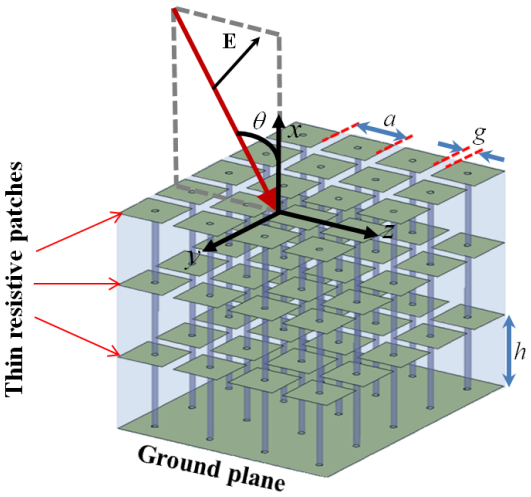


**Figure 3.1.** Geometry of a multilayer mushroom structure formed by periodically loading a grounded wire medium with thin resistive patches.

(CCA) method has been proposed for the design of absorbers with large bandwidths and optimal thicknesses in comparison to the Jaumann and CA absorbers. Most of the design procedures of the Jaumann and CA absorbers have been formulated for normal angle of incidence. Only a few design methods have been published considering oblique angle of incidence for different polarizations [20–22]. In [21,22], absorbing structures based on a single-layer mushroom HIS consisting of PEC patches placed on top of a metal backed wire-medium slab have been considered. However, these designs behave as materials with a local response, and the absorption is due to a lossy dielectric slab [22] or a resistive sheet placed on top of the structure [21]. Also, in [22] it has been shown that the presence of vias enhances the absorption bandwidth for obliquely incident TM-polarized plane waves.

Most of the absorbers are analyzed using time-consuming brute-force numerical simulations [26, 27], which do not provide much physical insight into the problem. Recently, homogenization methods [28–32] have been proposed to avoid the extensive computations demanded by the numerical simulations. These methods are shown to be very effective in modeling the interaction of electromagnetic waves with artificial

materials formed by lattices of periodic metallic or magneto-dielectric inclusions, and can be performed almost instantaneously.

In this work we extend our model [74] (wherein a single-layer mushroom structure with imperfectly conducting patches was considered) to study the absorption characteristics of a multilayered mushroom-type structure composed of thin material patches with a typical geometry as shown in Fig. 1. Aside from [74], in other previous work [68, 73], the vertical wires and patches have been assumed to be perfect electric conductors (PECs), and the present work concerns analysis of multilayer structure (shown in Fig. 1) with thin material (resistive) patches. Further, in [68] generalized additional boundary conditions (GABCs) have been derived for wire media terminated with distributed loads (metallic patch arrays acting as parallel loads to the wires) and lumped loads (arbitrary impedance insertions acting as series loads to the wires) or a combination of both at the junction, with the latter case presented in [75]. Although, the GABCs derived in [68] are applied at the wire-to-patch connection with the finite size of the patch (with certain restrictions imposed on the size of the gap between the patches with respect to the separation of adjacent patch arrays), these boundary conditions are valid only for perfect electric conductor terminations. However, the focus of the present work is on the use of thin material interfaces at the wire medium connections (acting as parallel loads to the wires). Therefore, new ABCs (which generalize [74] to the multilayer case) have to be derived which take into account the finite conductivity of the material at the connection points.

To address this issue, in this work we consider the case of wire media terminated with thin infinite resistive sheets or patch arrays (with $g \ll a$, where $a$ is the period of the patches and the wires, and $g$ is the gap between the adjacent patch elements), and derive ABCs at the connection of wires to a thin resistive sheet. The resulting ABCs are quite different than the previous ones for PEC patches. Based on these

conditions, we then characterize the reflection properties of the multilayer mushroom-type structure (with a typical geometry shown in Fig. 1). The required ABCs for two-sided wire media with thin resistive sheets at the junction have not been presented previously, and is a new contribution of this work. Further, we also aim to show that the presence of vias stabilizes the absorption response (as shown in [21] for a single-layer mushroom structure), enhances the absorption bandwidth (as shown in [22] for a single-layer mushroom structure), and increases the absorption performance for obliquely incident TM-polarized plane waves, making the multilayered mushroom structure an attractive candidate as an absorber.

It should be noted that although a simple transmission-line approach can be used to design some of the wideband absorbers (such as Jaumann, CA, and CCA), the analysis of the characteristics of a complicated structure such as the multilayer mushroom structure (considered in this work) using the transmission-line theory is not feasible. To overcome this drawback, in this work we present a simple analytical model (based on homogenization of wire media with new ABCs at terminations) in order to model the reflection characteristics of the multilayer mushroom structure with thin material patches, and also a design guide for the analysis of wideband absorbers with stable angle characteristics. Moreover, the proposed model produces results almost instantaneously when compared to the full-wave numerical simulations carried out with the use of commercial programs such as HFSS [36].

The chapter is organized as follows. In Section 3.2, the ABCs are derived at the two-sided wire medium connection to a thin resistive sheet, and the formalism of the analytical model is presented for the analysis of the reflection characteristics of the multilayer mushroom-type structure. In Section 3.3 we validate the derived ABCs, and then present the results for the single-layer, two-layer, and three-layer mushroom structure absorbers. Finally in Section 3.4 conclusions are drawn.

## 3.2 Analytical Modelling of Multilayered Mushroom-Type HIS Absorbers

In this section, we present an analytical model for the reflection characteristics of a multilayered mushroom structure. The multilayer structure is formed by a stack of 2-D subwavelength thin conductive/resistive square patch FSS elements separated by dielectric slabs perforated with metallic pins (vias) and backed by a ground plane (with the geometry shown in Fig. 3.1). First, ABCs based on conservation of charge will be derived at the interface of two uniaxial wire mediums with a thin infinite imperfect conductor at the junction. Based on these conditions, the scattering problem of the multilayer structure for a patch array will then be solved for an obliquely incident TM-polarized plane wave, assuming that the gap between the patch elements is small compared to the period ($g \ll a$). The case of TE polarization is not of interest here, because the electric field is orthogonal to thin metallic vias and the interaction is negligible. In the following, a time variation of the form $\mathrm{e}^{j\omega t}$ is assumed and suppressed.

### 3.2.1 Additional Boundary Conditions for a Double-Sided Wire Junction at Wire-to-Sheet Interface

Let us consider a junction between two uniaxial wire mediums with a thin infinite resistive sheet placed at the interface $x = x_0$ with the lattice period $a$ (as shown in Fig. 3.2). In general, the sheet at the junction can be an arbitrary 2-D material such as graphene or a 2-D plasma characterized by a complex surface conductivity. It is assumed that the wires have different radii ($r_1$ and $r_2$) with $r_{1,2} \ll a$, and are embedded in dielectric host media with relative permittivities $\varepsilon_{r,1}$ and $\varepsilon_{r,2}$, respectively. Both the sheet and the difference in the wire media properties (i.e., wire radii and host permittivities) introduce irregularities in the charge and the current distributions

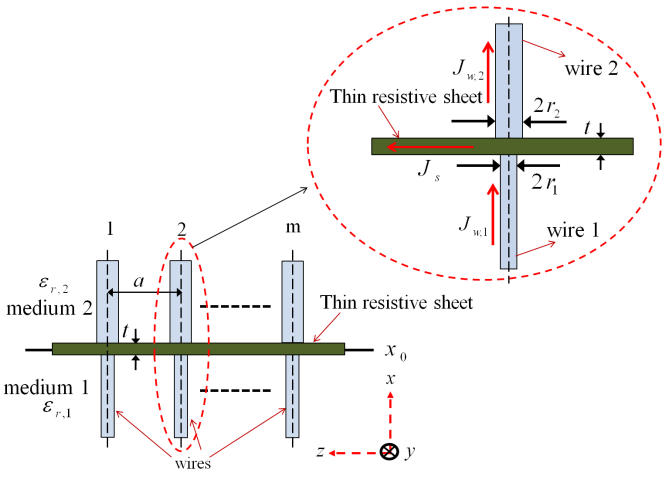


**Figure 3.2.** Geometry of a junction of two wire mediums with a thin infinite resistive sheet at the interface.

close to the junction. We note, however, that the charge/current non-uniformity that arises due to the different wire radii can be neglected when $r_{1,2} \ll a$, which is the case considered here. For simplicity, we assume that the wires are lossless (PEC).

Consider a plane wave incident on the configuration shown in Fig. 3.2. In what follows, the term *microscopic* refers to currents and fields in the microstructure of the medium, i.e., on the wires and sheets of the actual physical structure. The term *macroscopic* refers to fields averaged over the lattice period, i.e., the fields in the equivalent homogenized (continuous) medium. Let $J_{w,1}$ and $J_{w,2}$ be the microscopic current densities induced on the surface of the wires in mediums 1 and 2 (with radii $r_1$ and $r_2$, respectively). Let $\sigma_{2D}$ be the complex *surface* conductivity of the thin resistive sheet (such as graphene sheet with the surface conductivity given in [76]) placed at the interface. For thin materials with *bulk* conductivity $\sigma_{3D}$, the surface conductivity can be written as $\sigma_{2D} = \sigma_{3D}t$, where $t \ll \delta$ is the material thickness and $\delta = \sqrt{2/\omega\mu_0\sigma_{3D}}$ is the skin depth. On the thin conductive sheet, assumed local and isotropic, the microscopic current and the field are related as $J_s(y,z) = \sigma_{2D}E_t$, where $J_s$ is the surface current density and $E_t$ is the tangential electric field on the sheet. It should be noted that the tangential fields on the sheet in mediums 1 and 2

are assumed to be continuous at $x = x_0$, i.e.,

$$E_{t1}(x_0^-) = E_{t2}(x_0^+) = E_t \ . \tag{3.2.1}$$

The surface charge densities $\rho_{s1}$ and $\rho_{s2}$ on the PEC wires with radii $r_1$ and $r_2$ are given by $\rho_{s1}(x) = \varepsilon_0\varepsilon_{r,1}E_{n1}(x)$ and $\rho_{s2}(x) = \varepsilon_0\varepsilon_{r,2}E_{n2}(x)$, where $E_{n1}$ and $E_{n2}$ are the normal components of the microscopic electric fields at the wire surfaces. Considering that, at the wire-to-sheet and sheet-to-wire connection points ($x_0^+$ and $x_0^-$), the electric fields normal to the wires are the same as the tangential fields on the thin resistive sheet, we can write

$$E_{n1}(x_0^-) = E_{t1}(x_0^-) = \rho_{s1}(x_0^-)/(\varepsilon_0\varepsilon_{r,1}) \tag{3.2.2}$$

$$E_{n2}(x_0^+) = E_{t2}(x_0^+) = \rho_{s2}(x_0^+)/(\varepsilon_0\varepsilon_{r,2}) \ . \tag{3.2.3}$$

In addition, we have the continuity equation for the wires $\rho_{si} = -(1/j\omega)\mathrm{d}J_{w,i}(x)/\mathrm{d}x$ $(i = 1, 2)$. At the connection points ($x_0^+$ and $x_0^-$), the surface charge densities can be written as

$$\rho_{s1}(x_0^-) = -(1/j\omega)(\mathrm{d}J_{w,1}(x)/\mathrm{d}x)|_{x_0^-} \tag{3.2.4}$$

$$\rho_{s2}(x_0^+) = -(1/j\omega)(\mathrm{d}J_{w,2}(x)/\mathrm{d}x)|_{x_0^+} \ . \tag{3.2.5}$$

From Fig. 3.2, using Kirchoff's current law (conservation of charge) at the junction of two wire mediums with thin resistive sheet at the interface, we have

$$J_s = J_{w,1} - J_{w,2} \ . \tag{3.2.6}$$

Using (3.2.1), the surface current density can be expressed as

$$\begin{aligned} J_s &= \sigma_{2\mathrm{D}}E_t = \sigma_{2\mathrm{D}}E_{t1}(x_0^-) = \sigma_{2\mathrm{D}}E_{t2}(x_0^+) \\ &= \sigma_{2\mathrm{D}}\left[E_{t1}(x_0^-) + E_{t2}(x_0^+)\right]/2 \ . \end{aligned} \tag{3.2.7}$$

Equating now (3.2.6) and (3.2.7) and using (3.2.4)-(3.2.5) in the expression for the tangential fields (3.2.2)-(3.2.3) we obtain the following ABC:

$$\frac{\sigma_{2\mathrm{D}}}{2j\omega\varepsilon_0}\left[\frac{1}{\varepsilon_{r,1}}\frac{\mathrm{d}J_{w,1}(x)}{\mathrm{d}x}\bigg|_{x_0^-}+\frac{1}{\varepsilon_{r,2}}\frac{\mathrm{d}J_{w,2}(x)}{\mathrm{d}x}\bigg|_{x_0^+}\right]+\left[J_{w,1}(x_0^-)-J_{w,2}(x_0^+)\right]=0\,. \quad (3.2.8)$$

By enforcing the continuity of tangential fields at the thin conductive sheet interface (3.2.1), we obtain the second ABC for the microscopic wire current:

$$\frac{1}{\varepsilon_{r,1}}\frac{\mathrm{d}J_{w,1}(x)}{\mathrm{d}x}\bigg|_{x_0^-}-\frac{1}{\varepsilon_{r,2}}\frac{\mathrm{d}J_{w,2}(x)}{\mathrm{d}x}\bigg|_{x_0^+}=0\,. \quad (3.2.9)$$

In Section 3.2.2, it will be shown that the ABCs (3.2.8) and (3.2.9) are essential in solving the reflection problem of a multilayered mushroom structure. Also, it is worth noting that the conditions (3.2.8) and (3.2.9) derived in this section are applicable to the cases of different conductivities of the thin conductive patch at the wire-medium junction, provided the gap between the patch elements is much smaller than the period $g \ll a$.

For the limiting case of the identical wire media on either side of the thin resistive sheet interface at $x_0$ (i.e., $\varepsilon_{r,1}=\varepsilon_{r,2}=\varepsilon_r$ and $r_1=r_2=r$), the ABCs (3.2.8) and (3.2.9) in this case can be obtained by enforcing the continuity of surface charge densities and using the Kirchoff's current law at the connection points $x_0^+$ and $x_0^-$, i.e., $\rho_{s1}(x_0^-)=\rho_{s2}(x_0^+)=\rho_s=\varepsilon_0\varepsilon_r J_s/\sigma_{2\mathrm{D}}=(\rho_{s1}(x_0^-)+\rho_{s2}(x_0^+))/2$ and $J_w(x_0^-)=J_s+J_w(x_0^+)$

In the limiting case of $\sigma_{2\mathrm{D}}\to 0$, (transparent sheet) we have a continuous wire-medium slab with simple continuity conditions for the current: $J_w(x_0^+)=J_w(x_0^-)$ and $\mathrm{d}J_w(x)/\mathrm{d}x|_{x_0^+}=\mathrm{d}J_w(x)/\mathrm{d}x|_{x_0^-}$. For $\sigma_{2\mathrm{D}}\to\infty$, we have a perfect electric conducting ground plane with the ABC for wire microscopic currents given by $\mathrm{d}J_w(x)/\mathrm{d}x|_{x_0^+}=\mathrm{d}J_w(x)/\mathrm{d}x|_{x_0^-}=0$, i.e., the derivative of each of the wire currents is independently zero at the connection points. This result is consistent with the result of the single-sided wire-medium junction with a conducting ground plane [66]. In addition, with the assumption that $g \ll a$, the above result has been successfully used for characterizing various mushroom-type structures, which include a single-layer mushroom

structure terminated with PEC patches [71, 72] and a multilayer mushroom structure [73] for characterizing negative refraction. However, for moderate and large gaps between the patches these boundary conditions give inaccurate results. To overcome this issue GABCs similar to those proposed in [68] (for the PEC patches) have to be considered:

$$\left.\frac{\mathrm{d}J_w(x)}{\mathrm{d}x}\right|_{x_0^+} + \left.\frac{\mathrm{d}J_w(x)}{\mathrm{d}x}\right|_{x_0^-} = \frac{2C}{C_0}\left[J_w(x_0^+) - J_w(x_0^-)\right] \tag{3.2.10}$$

$$\left.\frac{\mathrm{d}J_w(x)}{\mathrm{d}x}\right|_{x_0^+} - \left.\frac{\mathrm{d}J_w(x)}{\mathrm{d}x}\right|_{x_0^-} = 0 \tag{3.2.11}$$

where $C$ is the capacitance of the wires and $C_0$ is the capacitance of the metallic patch which depends on the period $a$ and gap $g$ (the values of $C$ and $C_0$ are defined in [68]). These ABCs are accurate for moderate and large gaps between the patches, provided the distance $h$ between the metallic patches in adjacent layers is much greater than $g$. When the gap between the patches reduces and $C_0 \to \infty$, we have a perfect electric conducting ground plane with the ABCs (3.2.10), (3.2.11) reduce to $\mathrm{d}J_w(x)/\mathrm{d}x|_{x_0^+} = \mathrm{d}J_w(x)/\mathrm{d}x|_{x_0^-} = 0$, which is the same expression obtained above from (3.2.8), (3.2.9) when $\sigma_{2D} \to \infty$. However, the GABCs (3.2.10), (3.2.11) apply to the modeling of wire media with metallic (PEC) terminations, whereas the ABCs (3.2.8), (3.2.9) obtained in this work deals with thin material (resistive) terminations (however, gap capacitance is not accounted for).

Further, it is interesting to note that the ABCs (3.2.8) and (3.2.9) derived in this section for the double-sided wire medium are generalizations of the simpler (single-sided) case studied in [74], i.e., one can obtain the ABC given in [74] by letting either $J_{w,1} = 0$ or $J_{w,2} = 0$. For example, for the case of wires in the half-space $x < x_0$, the ABC reads

$$J_{w,1}(x_0^-) + \frac{\sigma_{2\mathrm{D}}}{j\omega\varepsilon_0\varepsilon_{r,1}}\frac{\mathrm{d}J_{w,1}(x)}{\mathrm{d}x}|_{x_0^-} = 0 \tag{3.2.12}$$

which corresponds exactly to the ABC derived in ( [74], Eq. (5)). Therefore, while a

single ABC is sufficient to describe the electromagnetic phenomenon of a single-sided wire-medium junction, the general case of a double-sided junction requires two ABCs, and the fact that the termination is resistive rather than metallic leads to the new ABCs presented in this work. In relation to the ABCs (3.2.8) and (3.2.9), below we summarize some of the ABCs developed in literature for terminated wire media. In [71–73], the ABCs are valid for single-sided and double-sided wire media terminated with PEC patches, which does not take into account the gap capacitance, i.e., are valid only for $g \ll a$. In [68], the ABCs are valid for wire media terminated with PEC patches for moderate and large gaps between the patches, i.e., takes into account the gap capacitance. In [74], the ABCs are derived for single-sided wire media terminated by thin resistive sheets and are applicable to resistive patches, provided $g \ll a$, i.e., does not take into account the gap capacitance.

### 3.2.2 Scattering Problem of the Multilayered Mushroom-Type Absorber

In order to illustrate the application of the new ABCs (3.2.8) and (3.2.9), here we study the scattering problem of a multilayered mushroom structure with the geometry as that shown in Fig. 3.3 ($a$ is the period of the patches and vias). It is assumed that each dielectric layer, perforated with thin metallic vias of radius $r_l \ll a$, is homogeneous and isotropic of thickness $h_l$, characterized by relative permittivity $\varepsilon_{r,l}$ and permeability of free space, and loaded with 2-D periodic thin conductive patches of conductivity $\sigma_{2\mathrm{D},l}$ at the interface $d_l, l = 1, 2, \ldots, m$. The objective is to obtain the reflection characteristics of the structure for a TM plane-wave incidence. It should be noted that the ABCs (3.2.8) and (3.2.9) derived in Section 3.2.1 are applicable to resistive patch arrays when the gap between the patch elements is much smaller than the period ($g \ll a$) since they are derived for an infinite sheet.

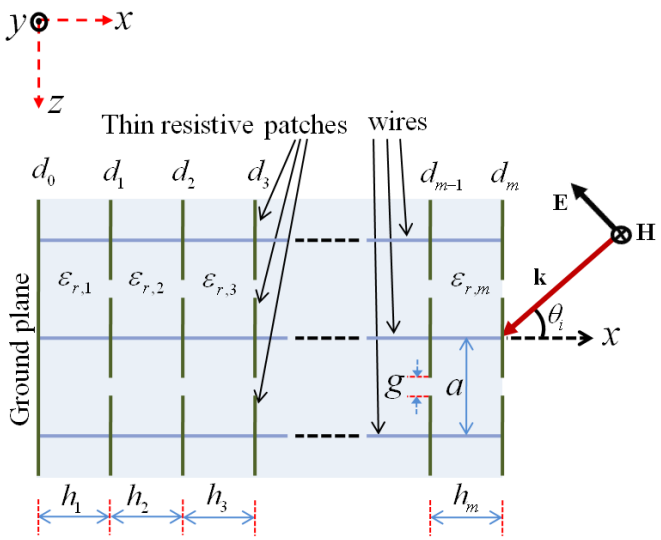


**Figure 3.3.** Schematic of a generic multilayer mushroom structure formed by periodically loading grounded wire medium with thin resistive square patches (side view).

Consider a time-harmonic plane wave incident on the multilayer mushroom structure shown in Fig. 3.3. Each wire-medium slab is characterized by the nonlocal dielectric function [64, 65] $\varepsilon_{\text{eff},l} = \varepsilon_0\varepsilon_{r,l}\,[\varepsilon_{xx,l}(\omega,k_x)\hat{x}\hat{x} + \hat{y}\hat{y} + \hat{z}\hat{z}]$, where $\varepsilon_{xx,l}(\omega,k_x) = 1 - k_{p,l}^2/(k_{h,l}^2 - k_x^2)$, $k_{h,l} = k_0\sqrt{\varepsilon_{r,l}}$ is the wavenumber in the host material, $k_0$ is the wavenumber in free space, $k_{p,l}$ is the plasma wavenumber which depends on the period and radius of the vias: $k_{p,l}^2 = (2\pi/a^2)/[\ln(a/2\pi r_l)+0.5275]$, and $k_x$ is the $x$-component of the wave vector $\mathbf{k} = (k_x, 0, k_z)$. Let $J_{w,l}$ be the surface current densities induced on the metallic wires. It is known that for a TM plane-wave incidence, the wire medium excites both transverse electromagnetic (TEM) and TM$^x$ modes, and thus, following [65], the electric and magnetic fields in the air region ($x > d_m$) are given by

$$\eta_0 H_y = \mathrm{E}^{\gamma_0(x-d_m)} + R\,\mathrm{E}^{-\gamma_0(x-d_m)} \tag{3.2.13}$$

$$E_z = \frac{-j\gamma_0}{k_0}\left[\mathrm{E}^{\gamma_0(x-d_m)} - R\,\mathrm{E}^{-\gamma_0(x-d_m)}\right] \tag{3.2.14}$$

and the fields in the wire-medium slab ($d_{l-1} < x < d_l$) can be written as,

$$\eta_0 H_y^{(l)} = A^+_{\mathrm{TM},l}\,\mathrm{E}^{\gamma_{\mathrm{TM},l}(x-d_{l-1})} + A^-_{\mathrm{TM},l}\,\mathrm{E}^{-\gamma_{\mathrm{TM},l}(x-d_{l-1})} + B^+_{\mathrm{TEM},l}\,\mathrm{E}^{\gamma_{\mathrm{TEM},l}(x-d_{l-1})} + B^-_{\mathrm{TEM},l}\,\mathrm{E}^{-\gamma_{\mathrm{TEM},l}(x-d_{l-1})} \quad (3.2.15)$$

$$E_x^{(l)} = \frac{k_z}{\varepsilon^{\mathrm{TM}}_{xx,l} k_0 \varepsilon_{r,l}} \left[A^+_{\mathrm{TM},l}\,\mathrm{E}^{\gamma_{\mathrm{TM},l}(x-d_{l-1})} + A^-_{\mathrm{TM},l}\,\mathrm{E}^{-\gamma_{\mathrm{TM},l}(x-d_{l-1})}\right] \quad (3.2.16)$$

$$E_z^{(l)} = \frac{-j\gamma_{\mathrm{TM},l}}{\varepsilon_{r,l} k_0} \left[A^+_{\mathrm{TM},l}\,\mathrm{E}^{\gamma_{\mathrm{TM},l}(x-d_{l-1})} - A^-_{\mathrm{TM},l}\,\mathrm{E}^{-\gamma_{\mathrm{TM},l}(x-d_{l-1})}\right] - \frac{j\gamma_{\mathrm{TEM},l}}{\varepsilon_{r,l} k_0} \left[B^+_{\mathrm{TEM},l}\,\mathrm{E}^{\gamma_{\mathrm{TEM},l}(x-d_{l-1})} - B^-_{\mathrm{TEM},l}\,\mathrm{E}^{-\gamma_{\mathrm{TEM},l}(x-d_{l-1})}\right] \quad (3.2.17)$$

where $d_l = h_1 + h_2 + \ldots + h_l$, $l = 1, 2, \ldots, m$, $\eta_0 = \sqrt{\mu_0/\epsilon_0}$ is the free-space impedance, $R$ is the reflection coefficient, $A^{\pm}_{\mathrm{TM},l}$, $B^{\pm}_{\mathrm{TEM},l}$ are the amplitude coefficients of the TM and TEM fields, $\gamma_0 = \sqrt{k_z^2 - k_0^2}$, $\varepsilon^{\mathrm{TM}}_{xx,l} = 1 - k_{p,l}^2/(k_z^2 + k_{p,l}^2)$, $\gamma_{\mathrm{TEM},l} = jk_0\sqrt{\epsilon_{r,l}}$, $\gamma_{\mathrm{TM},l} = \sqrt{k_{p,l}^2 + k_z^2 - k_{h,l}^2}$, and $k_z = k_0 \sin\theta_i$.

To calculate the unknown coefficients, $R$, $A^{\pm}_{\mathrm{TM},l}$ $B^{\pm}_{\mathrm{TEM},l}$, we impose boundary conditions at $x = 0, d_1, d_2, \ldots, d_m$. Since, there are $m$ dielectric layers and $m$ interfaces, we have the total number of unknowns as $4m + 1$ (i.e., four unknowns in each layer corresponds to $4m$, and the remaining unknown is $R$). Hence, $4m+1$ boundary conditions are necessary to calculate the $4m+1$ unknown coefficients. At the thin resistive patch interfaces ($x = d_l^{\pm}$, $l = 1, \ldots, m$), the macroscopic two-sided impedance boundary conditions establish that the tangential electric ($E_z^{(l)}$) and magnetic fields ($H_y^{(l)}$), can be related via a sheet impedance, i.e.,

$$E_z^{(l)}|_{x=d_l^+} = E_z^{(l)}|_{x=d_l^-} = Z_{g,l}\left(H_y^{(l+1)}|_{x=d_l^+} - H_y^{(l)}|_{x=d_l^-}\right) \quad (3.2.18)$$

where $Z_{g,l}$ is the grid impedance of the thin conductive patches [34, 35, 74] given by

$$Z_{g,l} = \frac{a}{(a-g)\sigma_{2\mathrm{D},l}} - j\frac{\pi}{2\omega\varepsilon_0(\varepsilon^{\mathrm{qs}}_{r,l})a\ln\left(\csc\frac{\pi g}{2a}\right)} \quad (3.2.19)$$

where $\varepsilon_{r,l}^{\mathrm{qs}} = (\varepsilon_{r,l} + \varepsilon_{r,l+1})/2$ for interior patches ($l = 1, 2, \ldots, m-1$) and $\varepsilon_{r,m}^{\mathrm{qs}} = (\varepsilon_{r,m} + 1)/2$ for the patch located at the upper interface ($l = m$). This gives $2m$ boundary conditions. At the ground plane interface ($x = 0^+$), we have two more boundary conditions [65]: i) tangential macroscopic total electric field vanishes ($E_z^{(1)}|_{x=0^+} = 0$) and ii) derivative of current is zero ($\mathrm{d}J_{w,1}(x)/\mathrm{d}x|_{x=0^+} = 0$), [66], or in terms of macroscopic fields,

$$\left[ k_0 \varepsilon_{r,1} \frac{\mathrm{d}E_x^{(1)}(x)}{\mathrm{d}x} - k_z \eta_0 \frac{\mathrm{d}H_y^{(1)}(x)}{\mathrm{d}x} \right]_{x=0^+} = 0 \,. \tag{3.2.20}$$

Following [74], the boundary condition at the top patch interface, $x = d_m^-$, can be written as

$$J_{w,m}(d_m^-) + \frac{\sigma_{2\mathrm{D},m}}{j\omega\varepsilon_0\varepsilon_{r,m}} \frac{\mathrm{d}J_{w,m}(x)}{\mathrm{d}x}\bigg|_{d_m^-} = 0 \tag{3.2.21}$$

or, equivalently, the following macroscopic field condition:

$$\left(1 + \frac{\sigma_{2\mathrm{D},m}}{j\omega\varepsilon_0} \frac{\mathrm{d}}{\mathrm{d}x}\right) \left[ k_0 E_x^m(x) - \frac{k_z \eta_0}{\varepsilon_{r,m}} H_y^m(x) \right]_{d_m^-} = 0. \tag{3.2.22}$$

This gives the total number of $2m + 3$ conditions, clearly insufficient to calculate the $4m + 1$ unknown coefficients, which makes apparent the need of the ABCs derived in Section 3.2.1.

At the junction of two wire mediums with thin conductive patches at the interfaces ($x = d_l^{\pm}, l = 1, \ldots, m-1$) it is necessary to impose the ABCs (3.2.8) and (3.2.9), in addition to the boundary condition (4.2.1):

$$\frac{\sigma_{2\mathrm{D},l}}{2j\omega\varepsilon_0} \left[ \frac{1}{\varepsilon_{r,l}} \frac{\mathrm{d}J_{w,l}(x)}{\mathrm{d}x}\bigg|_{d_l^-} + \frac{1}{\varepsilon_{r,l+1}} \frac{\mathrm{d}J_{w,l+1}(x)}{\mathrm{d}x}\bigg|_{d_l^+} \right] + \left[ J_{w,l}(d_l^-) - J_{w,l+1}(d_l^+) \right] = 0 \tag{3.2.23}$$

$$\frac{1}{\varepsilon_{r,l}} \frac{\mathrm{d}J_{w,l}(x)}{\mathrm{d}x}\bigg|_{d_l^-} - \frac{1}{\varepsilon_{r,l+1}} \frac{\mathrm{d}J_{w,l+1}(x)}{\mathrm{d}x}\bigg|_{d_l^+} = 0 \,. \tag{3.2.24}$$

In terms of macroscopic fields, (3.2.23) and (3.2.24) can be rewritten as

$$\left(1+\frac{\sigma_{2\mathrm{D},l}}{2j\omega\varepsilon_0}\frac{\mathrm{d}}{\mathrm{d}x}\right)\left[k_0E_x^{(l)}(x)-\frac{k_z\eta_0}{\varepsilon_{r,l}}H_y^{(l)}(x)\right]_{d_l^-} = \left(1-\frac{\sigma_{2\mathrm{D},l}}{2j\omega\varepsilon_0}\frac{\mathrm{d}}{\mathrm{d}x}\right)\left[k_0E_x^{(l+1)}(x)-\frac{k_z\eta_0}{\varepsilon_{r,l+1}}H_y^{(l+1)}(x)\right]_{d_l^+} \quad (3.2.25)$$

$$\frac{\mathrm{d}}{\mathrm{d}x}\left[k_0E_x^{(l)}(x)-\frac{k_z\eta_0}{\varepsilon_{r,l}}H_y^{(l)}(x)\right]_{d_l^-} = \frac{\mathrm{d}}{\mathrm{d}x}\left[k_0E_x^{(l+1)}(x)-\frac{k_z\eta_0}{\varepsilon_{r,l+1}}H_y^{(l+1)}(x)\right]_{d_l^+}. \quad (3.2.26)$$

Since there are $m-1$ layers of two-sided wire-medium junctions, we have $2(m-1)$ boundary conditions and hence, the total number of boundary conditions are equal to $4m+1$. Using the boundary conditions (3.2.18), (3.2.20), (3.2.22), (3.2.25), and (3.2.26), we can easily obtain a linear system for the $4m+1$ unknowns of the problem. This system can be solved either numerically or analytically for the unknown field coefficients, $A_{\mathrm{TM},l}^{\pm}$ and $B_{\mathrm{TEM},l}^{\pm}$, and the reflection coefficient $R$.

## 3.3 Numerical Results and Discussions

In this section, we first validate the proposed ABCs for the junction of two-wire media separated by thin resistive patch arrays by comparing the analytical model results with the full-wave numerical simulations. Then we study wideband absorption characteristics of single-layer, two-layer, and three-layer mushroom structures (with the geometries shown in Figs. 3.11, 3.17, and 3.22, respectively) for obliquely incident TM-polarized plane waves. More remarkably, by employing the proposed structure, we show that vias can be used to increase the bandwidth and enhance absorptivity for the TM-polarized oblique incidence, by utilizing the resonances of the mushroom and wire-medium HIS structures. The results obtained using the analytical model for all the three structures are confirmed with lengthy full-wave numerical simulations.

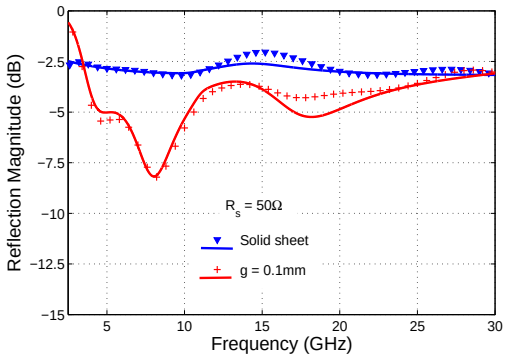


(a)

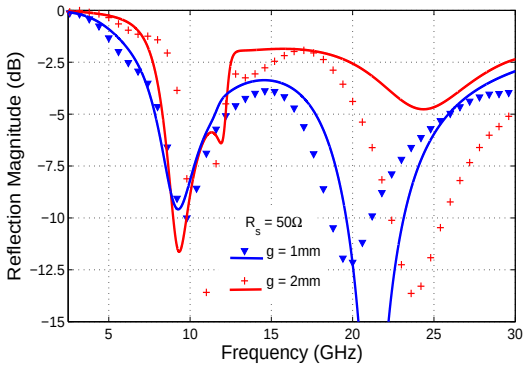


(b)

**Figure 3.4.** Comparison of analytical (solid lines) and full-wave HFSS results (symbols) of the reflection coefficient for the two-layer mushroom HIS absorber (with geometry and parameters shown in Fig. 3.17) with $R_{s1} = R_{s2} = 50\ \Omega$, $\theta = 45°$: (a) solid sheet and $g_1 = g_2 = 0.1$ mm and (b) $g_1 = g_2 = 1$ mm and $g_1 = g_2 = 2$ mm.

### 3.3.1 Validity of the Analytical model

Since the ABCs proposed in this work are derived for the interface of the wire media separated by a thin infinite (continuous) resistive sheet at the junction, they have to be thoroughly verified while applying to the resistive patch connections, wherein the gap $g$ between the patches plays an important role. To understand the effect of $g$ on the applicability of the proposed ABCs, here we consider a two-layer mushroom structure (with the geometry and parameters given in Fig. 3.17), and study its reflection magnitude behavior for varying resistivity $R_s$ and $g$ of the resistive patch arrays using

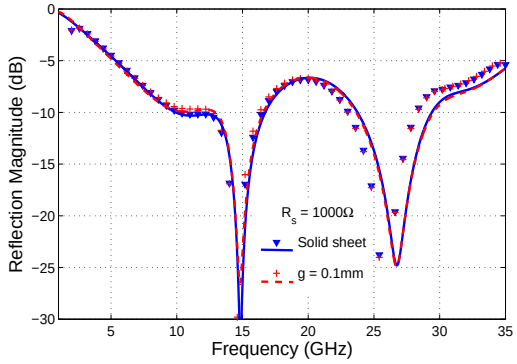


(a)

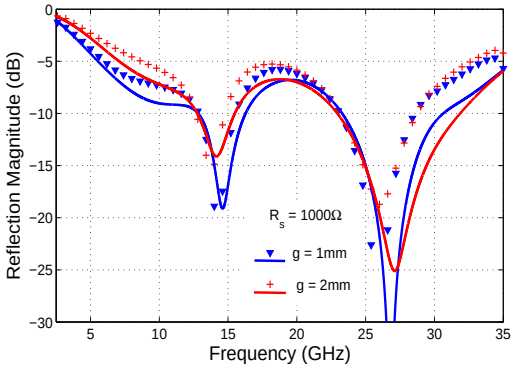


(b)

**Figure 3.5.** Comparison of analytical (solid lines) and full-wave HFSS results (symbols) of the reflection coefficient for the two-layer mushroom HIS absorber (with geometry and parameters shown in Fig. 3.17) with $R_{s1} = R_{s2} = 1000\ \Omega$, $\theta = 45°$: (a) solid sheet and $g_1 = g_2 = 0.1$ mm and (b) $g_1 = g_2 = 1$ mm and $g_1 = g_2 = 2$ mm.

the analytical model given in Section 3.2. Here $R_s$ is the sheet resistance, which depends on the bulk conductivity $\sigma_{3D}(\mathrm{S/m})$ of the material, i.e., $R_s = 1/\sigma_{2D} = 1/(\sigma_{3D}t)$. From (3.2.19) one can represent the grid impedance of the lossy patch array as a series RC circuit $(R_g - \mathrm{j}/(\omega C_g))$, where the real value corresponds to $R_g$ (resistance per unit cell) given by $a/((a-g)\sigma_{2D})$ or $R_s a/(a-g)$ and the imaginary value corresponds to $-1/(\omega C_g)$ (capacitive impedance) whose value can be obtained from (3.2.19). We first consider the case of oblique incidence $\theta = 45°$, with a low value of resistivity fixed in both the layers, i.e., $R_{s1} = R_{s2} = R_s = 50\ \Omega$ and study the reflection magnitude behavior versus frequency for increasing values of $g$. It is assumed here that

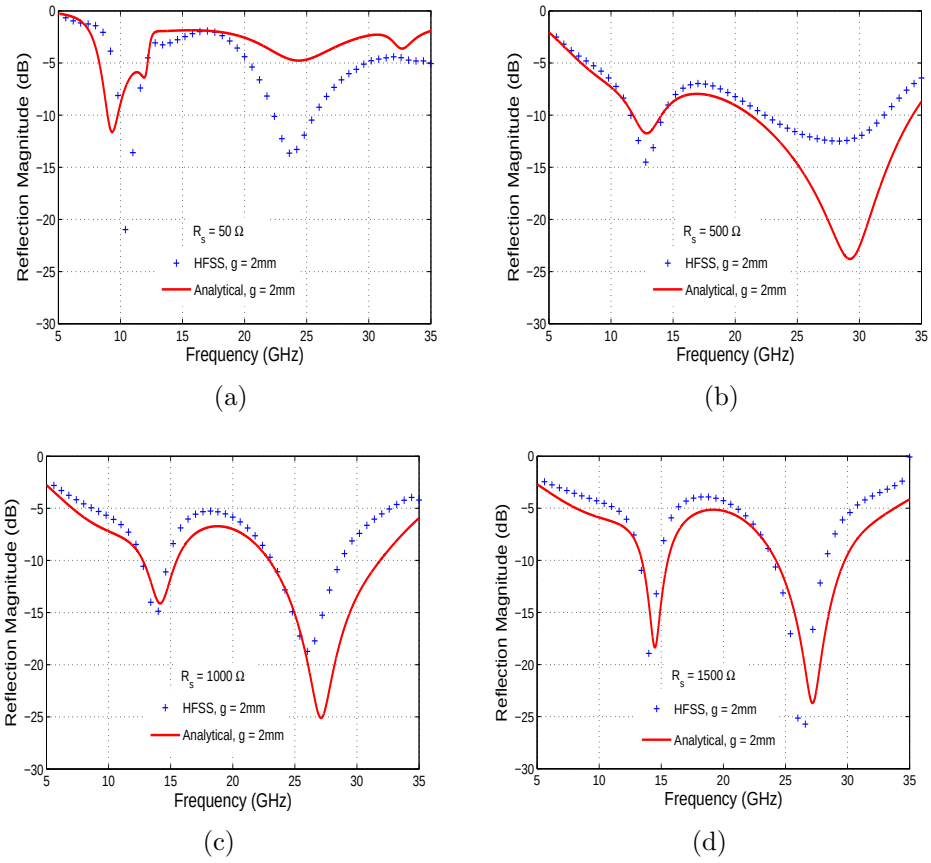


**Figure 3.6.** Comparison of analytical (solid lines) and full-wave HFSS results (symbols) of the reflection coefficient for the two-layer mushroom HIS absorber (with geometry and parameters shown in Fig. 3.17) for different resistivities of the patch arrays with $g_1 = g_2 = 2$ mm, $\theta = 45°$: (a) $R_{s1} = R_{s2} = 50\ \Omega$, (b) $R_{s1} = R_{s2} = 500\ \Omega$, (c) $R_{s1} = R_{s2} = 1000\ \Omega$, and (d)$R_{s1} = R_{s2} = 1500\ \Omega$.

$g$ takes the same value in both the patch array layers ($g_1 = g_2 = g$). The results are shown in Figs. 3.4(a) and 3.4(b). It is clear that, for solid sheet and for $g = 0.1$ mm (Fig. 3.4(a)), the analytical model results are in good agreement with the full-wave simulation results. However, as $g$ increases (i.e., for 1 mm and 2 mm cases), one can notice the discrepancies between the analytical model and numerical simulation results (Fig. 3.4(b)). This is due to the fact that the capacitive impedance (i.e., the imaginary part of the grid impedance expression) of the patch array dominates the resistivity of the patches, and since the ABCs (3.2.8) and (3.2.9) derived in this work does not take into account the capacitance of the patches for large gaps, the analytical

model results are not accurate. In the next scenario, we choose a high value of resistivity for the patch arrays in both the layers, and study a similar behavior as that shown in Fig. 3.4. The results are plotted in Fig. 3.5 for various values of $g$. It can be noticed that as $g$ increases, the reflection magnitude behavior calculated using the analytical model agrees well with the numerical results, even for large values of $g$ (e.g., for $g =$ 2 mm). In fact, for the same mushroom structure considered above with the PEC patches, with period $a$ and gap $g$ comparable to the separation $h$ between the patch arrays in the adjacent layers, the ABCs (3.2.10), (3.2.11) may give inaccurate results. However, (3.2.10), (3.2.11) give accurate results provided $h \gg g$. Surprisingly, the ABCs (3.2.8) and (3.2.9) obtained in this work are valid even when $g$ is large and comparable to $h$, though the conditions are derived for solid resistive sheets. This is due to the fact that the resistivity of the patch arrays dominates over the capacitive impedance. Further, it can be noticed from Fig. 3.5 that the reflection magnitude behavior does not show much variations for increasing values of $g$. This is again due to the fact that the value of capacitive impedance of the patch arrays with large gaps (even though it is large when compared to patch arrays with small gaps) is small when compared to the resistivity. In such a case, one can approximate the behavior of these patch arrays using a solid sheet of large resistivity.

To further clarify the effect of resistivity, in Fig. 3.6 we show the variation of reflection magnitude behavior versus frequency for different values of the sheet resistivities of the patch arrays of a similar structure studied in Figs. 3.4 and 3.5, however, for a fixed large gap value, i.e., for $g_1 = g_2 = g = 2$ mm. It can be noticed that with an increase in the sheet resistivity of the patch arrays, the analytical model results starts to agree with the numerical simulation results. This clearly demonstrates that when the resistivity of patch arrays is dominant over the capacitive impedance, the proposed ABCs give accurate results.

Thus, it is clear from the above analysis that for large gaps, as long as the capacitive impedance is less dominant than the resistivity of the patch arrays, the ABCs derived for the wire-sheet-wire connections can be accurately used to model wire-patch-wire junctions (for e.g., $R_s = 1000\ \Omega$ and $g = 2$ mm, as shown in Fig. 3.5(b)), however, for small gaps, the ABCs derived are valid for any resistivity of the patch arrays (for e.g., $R_s = 50\ \Omega$ and $g = 0.1$ mm, as shown in Fig. 3.4(a), and $R_s = 1000\ \Omega$ and $g = 0.1$ mm, as shown in Fig. 3.5(a)). Further, in the case of patch arrays with very small gaps, the behavior could be well approximated using a solid sheet even if sheet resistivity is low or high (and still large enough to dominate the reactive part of the impedance), however, for patch arrays with large gaps, the replacement of the patch array by a solid sheet is only valid when the sheet resistivity is sufficiently large.

### 3.3.2 Single-layer mushroom structure with thin metal or graphene patches

As a first example, a single-layer mushroom-type HIS structure with geometry shown in Fig. 3.7 is chosen. In this configuration, the patches are copper and have a thickness of 60 nm. The parameters of the structure are: $a = 2$ mm, $g = 0.2$ mm, $h = 1$ mm, $r_0 = 0.05$ mm, and $\varepsilon_r = 10.2$. The analysis is performed for an obliquely incident TM-polarized plane wave. Fig. 3.8(a) shows the comparison of reflection magnitude behaviors calculated using HFSS and the proposed homogenization model for a TM-polarized plane wave incident at 30° to the normal. Also, in Fig. 3.8(a) we have included the result obtained using the wire-PEC ABC ( [66]). Clearly, one can notice the difference between the results obtained using the ABC of the wire-PEC interface and the new ABC (GABC, wire-thin-metal interface - see (3.2.12)). In fact, the result obtained using the GABC is in good agreement with the HFSS [36] result. Fig. 3.8(b) shows the behavior of reflection magnitude for a metal patch with

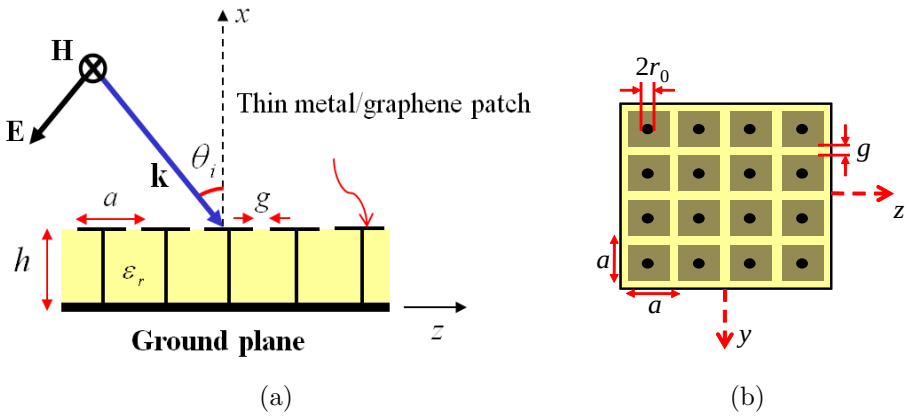


**Figure 3.7.** (a) Mushroom-type wire-medium structure with thin metal/graphene patches: (a) Side-view showing incident TM plane wave and (b) Top view of the structure.

$\sigma_{3D}t = 0.058$ S ( e.g. $t = 20$ nm and $\sigma_{3D} = 2.9\times10^6$ S/m). The remaining parameters are the same as those considered in the previous example. Again, the results obtained using the new ABC (wire-thin-metal interface) are in good agreement with the HFSS results, whereas the results obtained using the old ABC (wire-PEC interface [66]) deviate from the HFSS results. Fig. 3.9 shows the reflection magnitude behavior for the mushroom structure loaded with graphene patches with a chemical potential of $\mu_c = 0.5185$ eV [see [76] for the surface conductivity of graphene] for a plane wave incident at $\theta = 45°$. For example, at $f = 11.96$ GHz the complex surface conductivity, $\sigma_{2D} = 0.0304 - j0.0011$ S. Clearly, excellent agreement is seen between the GABC and the HFSS results. As is obvious, the ABC-PEC [66] and local model [71] results give significant errors since this ABC assumes that the surface charge at the tip of the wires or at the wire-patch interface vanishes. This may hold true for the wire-PEC interface, but does not apply for the wire-thin-metal/graphene interface. This is because at the wire-thin-metal interface, charge accumulation and diffusion takes place and the fields completely penetrate the metal. Hence, a new ABC (GABC) is required to obtain the correct result.

Referring to Fig. 3.9, one can notice that the nonlocal model result (ABC-PEC)

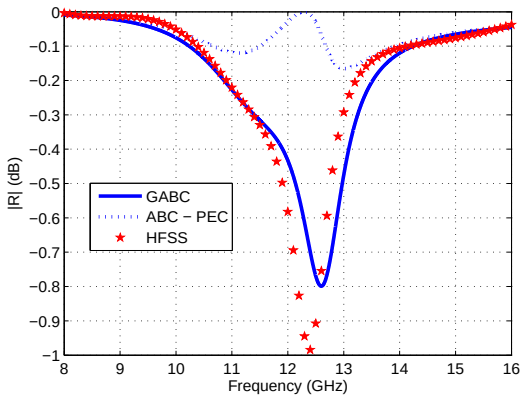


(a)

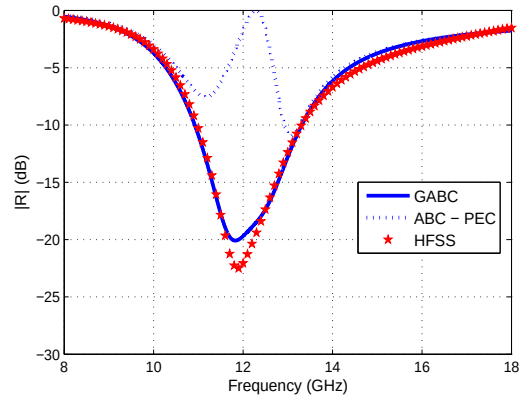


(b)

**Figure 3.8.** Reflection coefficient for a TM-polarized plane wave incident at $\theta = 30°$. (a) Copper patches with thickness 60 nm. (b) A material patch with $\sigma_{3D}t = 0.058$ S.

and the local model result agree well with each other. This is because, for the large chemical potential 0.5185 eV considered in this example, it seems that the spatial dispersion effects in the wire media are reduced, and the mushroom structure can be treated as a uniaxial continuous Epsilon-Negative material loaded with PEC patches (although this is not the case with the GABC, which sees the interface in a correct manner).

Overall Figs. 3.8 and 3.9 show the effectiveness of the new ABC. Hence, when a PEC wire is connected to a thin-metal patch, as is the case considered here, the new ABC is the good choice to obtain the correct result.

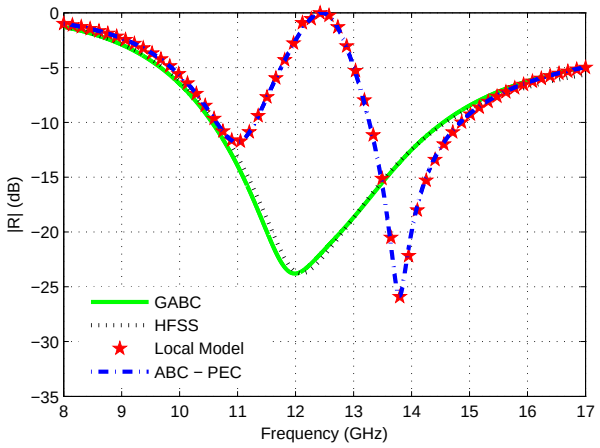


**Figure 3.9.** Reflection coefficient of the mushroom structure loaded with graphene patches with $\theta = 45°$.

To understand the behavior (effects of spatial dispersion) of the grounded wire-medium slab loaded with graphene patches, in Fig. 3.10 we plotted the normalized wire current along the vias for different values of bias ($\mu_c$). It can be noticed that for zero bias ($\mu_c = 0$) the current is quite nonuniform and as the bias increases, the current becomes more and more uniform. This is because, for the case of zero bias the patch is almost transparent or in other words its conductivity ($\sigma_{2D}$) is very small (can be seen in Fig. 3.10) and behaves as a dielectric material rather than a metal. As the bias increases, the conductivity increases and the properties of the patch will be close to that of a metal (since, it is known that for a vias truncated with a PEC patch the current is uniform [71]). Hence, the current starts to become more and more uniform, indicating that the spatial dispersion effects are negligible and the wire-medium slab can be treated as a uniaxial continuous Epsilon Negative material [71,72] loaded with patches. However, it should be noted that, despite the uniformity of the current for the case of $\mu_c = 0.5185$ eV, the homogenization model still needs an ABC to model the graphene patch mushroom structure, indicating that spatial dispersion effects are important for this structure. This is because, at the patch-to-wire interface, diffusion and accumulation of charge occurs (unlike at a wire-to-PEC interface, where surface

charge vanishes) and an ABC is required to capture the physics.

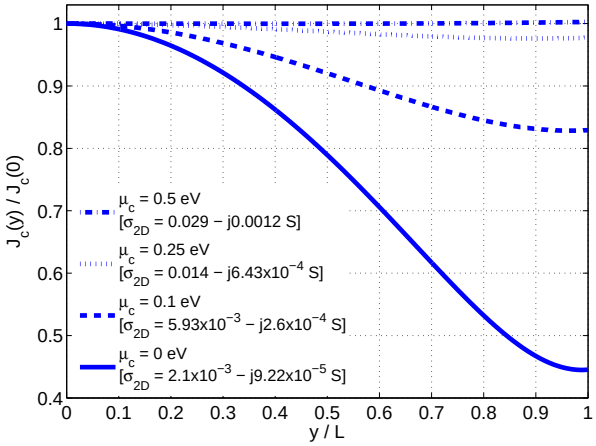


**Figure 3.10.** Normalized wire current for a graphene patch mushroom structure for different values of bias at $f = 14$ GHz.

By observing Figs. 3.8 and 3.9, one can notice a dip in the reflection magnitude curves for some values of the conductivity or the thickness of the metal patch. This behavior of showing reflection nulls allows the mushroom structures with thin-metal/graphene patches to be used in absorber applications. By properly selecting the parameters of the mushroom structure, one can easily obtain either a narrow band or even a wideband absorber. More on the design and analysis of realizing the absorbers is explored in the next section.

### 3.3.3 Single-Layer Mushroom Structure with Thin Resistive Patches

To demonstrate the performance of the proposed absorber (the multilayered mushroom structure shown in Fig. 3.1), we begin with the analysis of the reflection properties of the single-layer mushroom structure shown in Fig. 3.11 composed of an array of thin resistive patches printed over a grounded dielectric slab perforated with metallic vias.

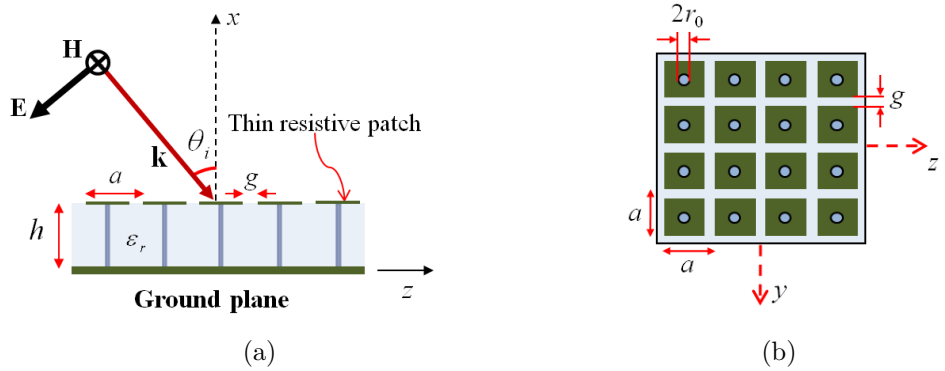


**Figure 3.11.** (a) Single-layer mushroom-type HIS absorber with thin resistive patches. (b) Top view of the structure.

Although this structure is similar to the one studied in [74], we employ this example to show that the mushroom structure (with resistive patches), when designed properly, enhances the absorption bandwidth for increasing angles of the obliquely incident TM-polarized plane wave. To show this effect, we consider the following parameters in the design of the absorber: $a = 6.8\,\text{mm}$, $g = 0.5\,\text{mm}$, $h = 3.5\,\text{mm}$, $r_0 = 0.08\,\text{mm}$, $\varepsilon_r = 2.5$, and $R_s = 106.54\,\Omega$. The rationale behind the choice of this particular value of $R_s$ will be discussed later in this section. Figure 3.12 shows the reflection coefficient for the incident angles of 30°, 45°, and 60°. The results ob-

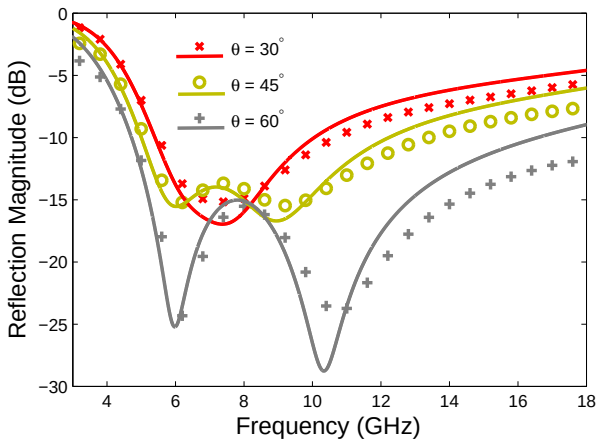


**Figure 3.12.** Comparison of analytical (solid lines) and full-wave HFSS results (crosses, circles, and plus signs) of the reflection coefficient for the single-layer mushroom HIS absorber excited by a TM-polarized plane wave at oblique angles of incidence $\theta$.

tained using the analytical model described in Section 3.2 (for the limiting case of single-sided wire-to-patch junction), and in [74], agree well with the full-wave HFSS results. In order to demonstrate the advantage of the mushroom-type absorber, in Fig. 3.13 we present the behavior of the reflection coefficient for a similar structure without vias, with the parameters listed above. In the absence of vias, the absorber can be easily modeled using a simple circuit theory model given in [34,37,38]. Again, the results obtained using the circuit model are in good agreement with the HFSS results. It is observed that for large angles of incidence, the absorption bandwidth is

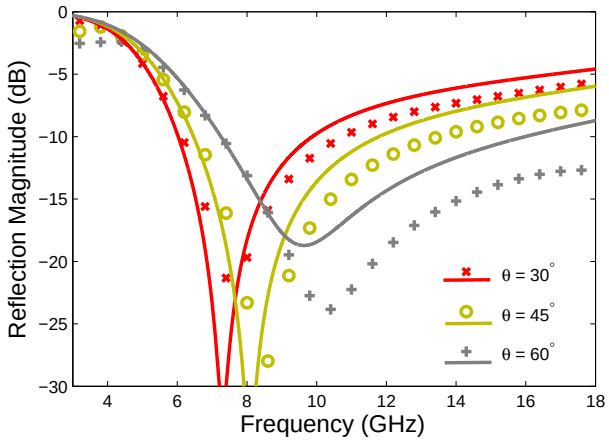


**Figure 3.13.** Comparison of analytical (solid lines) and full-wave HFSS results (crosses, circles, and plus signs) of the reflection coefficient for the single-layer HIS absorber (without vias) excited by a TM-polarized plane wave at oblique angles of incidence $\theta$.

increased in Fig. 3.12 as compared to the case of the same structure without the vias (Fig. 3.13). In Fig. 3.12 it is noticed that the lower frequency bound of the absorption band (around 6 GHz) is stable, which is in complete contrast to the behavior of the structure without vias (Fig. 3.13). This frequency stability can be attributed to the increased interaction of the incident wave with the vias. Furthermore, it is shown in Fig. 3.12 that the enlargement of the absorption band allows to maintain good absorption at the center frequency of the band for different angles of incidence, providing better performance with respect to the structure without vias.

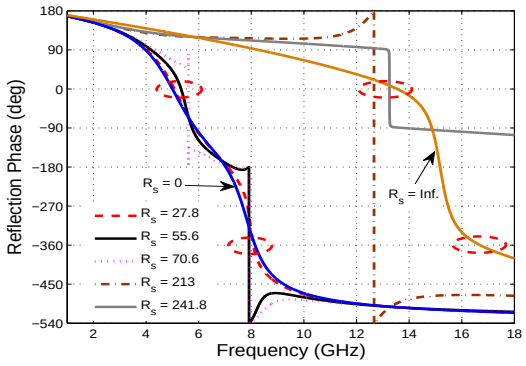


(a)

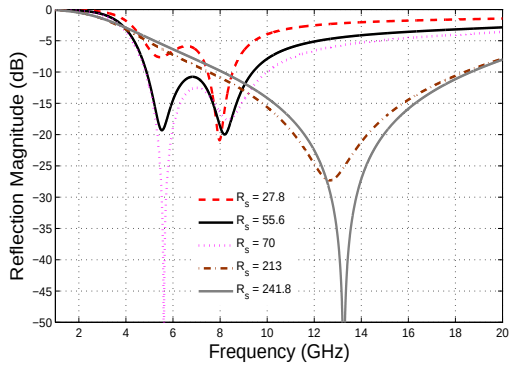


(b)

**Figure 3.14.** (a) Phase and (b) magnitude of the reflection coefficient of the single-layer mushroom structure for different values of sheet resistivity $R_s$ (in $\Omega$), $\theta = 45°$.

To understand the physical reasons of the wideband absorption in the mushroom structure, in Fig. 3.14, we show the reflection properties (phase and magnitude) for a TM-polarized plane wave incident at 45°, for different resistive values (for $R_s$ ranging from 0 to $\infty$; i.e., from the PEC patch to the transparent patch) of the thin resistive patch arrays using the analytical model. Starting with the PEC patch case (i.e., $R_s = 0$ or $\sigma_{3D}t = \infty$), the reflection phase behavior shows two resonances (shown in red circles in Fig. 3.14(a)) corresponding to the 0° or 360° phase (acting as a HIS), consistent with the result of the HIS discussed in [71, 72]. These resonances are such that one lies above the plasma frequency ($f_p/\sqrt{\varepsilon_r} = 6.28\,\text{GHz}$) and the other lies below $f_p/\sqrt{\varepsilon_r}$. However, this is not the case for the structure without vias,

where there is only one HIS resonance. The additional resonance of the mushroom structure, along with the proper choice of resistivity of the patch arrays and the fact that obliquely incident TM-polarized plane waves interact strongly with the vias, will be used to design wideband absorbers with enhanced absorption. With the increase in the resistive sheet values, one can notice in Fig. 3.14(a) the deviation of the reflection phase behavior from the actual HIS performance. The reason for this behavior is quite simple: a change in the sheet resistivity values affects the grid impedance [see Eq. (3.2.19)] of the patch array, which further changes the surface impedance of the mushroom structure. This deviation of the reflection phase behavior (resonances) is referred to as perturbed HIS behavior. Also, increasing the resistivity of the patch arrays increases the losses in the structure. As a result, a fraction of the total energy of the incident wave will be absorbed, depending on the values of the sheet resistivity (shown in Fig. 3.14(b)). For example, a value of sheet resistivity of $R_s = 27.8\,\Omega$, whose reflection magnitude behavior shows two reflection minima (dashed red curve in Fig. 3.14(b)), corresponds closely to the two perturbed HIS resonances (Fig. 3.14(a)).

By slowly increasing the sheet resistivity, there is a shift in the absorption levels of the two reflection minima (i.e., one of the reflection minima deepens, and the other minima either subdues or remains the same). This is due to match/mismatch of the surface impedance of the structure to the free-space impedance at those frequencies. In particular, for the sheet resistivity values of $70.6\,\Omega$ and $241.8\,\Omega$, we have perfect absorption for one of the reflection minima (at frequencies 5.612 GHz and 13.25 GHz, respectively). Under this condition the zero reflection phases shown in Fig. 3.14(a) correspond exactly to these frequencies. This proves the fact that the reflection minima shown in Fig. 3.12, for the case of $R_s = 106.54\,\Omega$ are nothing but the perturbed HIS resonances of the actual HIS structure with PEC patches. Hence, by utilizing

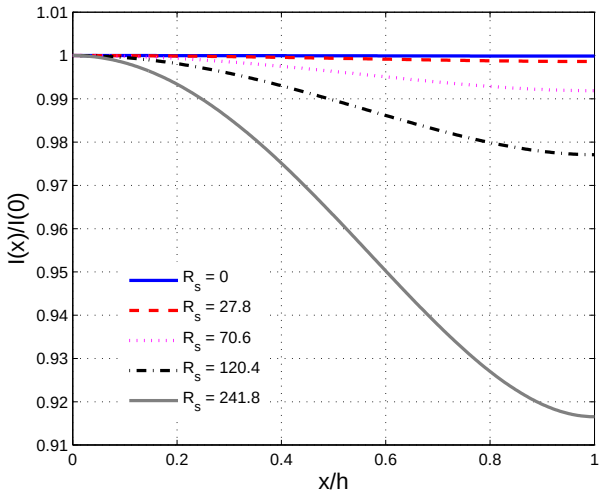


**Figure 3.15.** Normalized wire current in the single-layer mushroom structure for different values of sheet resistivity $R_s$ (in $\Omega$) at $f = 7\,\text{GHz}$, $\theta = 45°$.

the two resonances of the mushroom structure, along with the proper choice of resistivity of patch arrays, the absorption bandwidth is enlarged. This is not noticed in the structure without vias, where a single resonance of the HIS exists, and hence, the absoption band is narrow. With further increase in the resistivity of the patch arrays (as $R_s \to \infty$ $[\sigma_{3D}t \to 0]$ the patch array is fully transparent), we reach the case of the wire-medium slab (bed-of-nails) [72], which shows two resonances corresponding to zero phase (acting as a HIS). Therefore, it is obvious that for any value of $R_s$ between 0 and $\infty$, one should observe the perturbed HIS behavior of either the mushroom structure with PEC patches, $R_s = 0$, or the structure with transparent patches, $R_s = \infty$.

To validate that the resonances observed in the mushroom HIS absorber considered in this section are the perturbed HIS resonances of the mushroom HIS structure with PEC patches, we studied the current distribution for various resistivities, with $R_s$ varying from 0 to $\infty$. Figure 3.15 shows the normalized wire current in the single-layer mushroom structure at $f = 7\,\text{GHz}$. For small values of $R_s$ (i.e., from 0 to $120.4\,\Omega$) it is observed that the wire current is uniform, indicating that spatial dispersion effects

are almost negligible. This is consistent with the study reported in [74], where it was shown that for large values of $\sigma_{2D}$, the current distribution is uniform (which shows that spatial dispersion is reduced; however, an ABC [74, eq. (6)] is necessary in the analytical model). Since, the values of $R_s$ are small ($R_s = 0$ to $120.4\,\Omega$), current distribution is uniform (similar to the case of mushroom structure with PEC patches [71,72]), and the phase behavior of the perturbed structure is close to that of the mushroom structure with PEC patches (blue curve in Fig. 3.14(a)), the resonances of the perturbed structure (absorber) observed in Fig. 3.14(a) (with corresponding magnitudes in Fig. 3.14(b)) are indeed the perturbed HIS resonances of the mushroom structure with PEC patches.

In [22], an absorber composed of PEC patches on a lossy grounded dielectric slab perforated with metallic vias was studied to enhance the absorption bandwidth for the obliquely incident plane wave. We investigated this structure using the methodology described above (i.e., the reflection properties, phase and magnitude, are analyzed with increasing losses in the dielectric slab) and in fact it is observed that the wideband absorption is due to the perturbed HIS resonances rather than to the utilization of the plasma resonance, as suggested by the authors in [22].

Since the patch arrays are the only lossy components in the absorber shown in Fig. 3.11, their sheet resistivity value constitutes an important factor in the performance of the absorber. Hence, selecting a proper value of $R_s$ is the key in the design of wideband absorbers. One way of obtaining an optimum value of $R_s$ for a wideband absorber is to use numerical optimization techniques, which is beyond the scope of this work. Given that the analytical model provides results almost instantaneously, it provides a reliable, fast, and efficient solution in selecting an optimum sheet resistance of the patch arrays. The idea is to obtain a certain range for $R_s$ (in the range between the PEC case and wire-medium slab case) for each of the angles

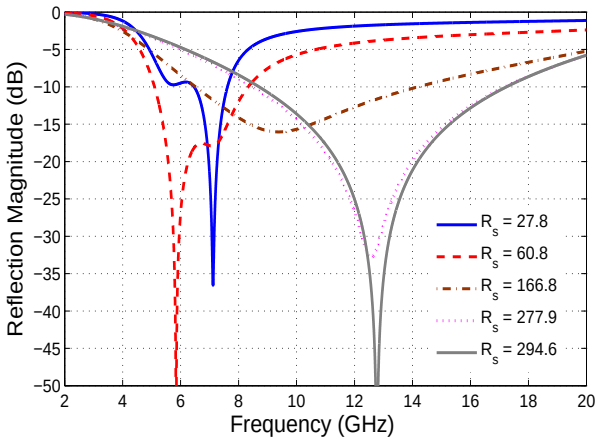


**Figure 3.16.** Reflection magnitude of the single-layer mushroom structure for different values of sheet resistivity $R_s$ (in $\Omega$), $\theta = 30^{\circ}$.

of incidence, where perfect reflection nulls are noticed for one of the two perturbed HIS resonances of the structure.

Figure 3.16 shows the reflection coefficient for a TM-polarized plane wave incident at 30°. Starting from the case of PEC patch array (i.e., $R_s = 0$), the sheet resistivities are increased gradually up to $R_s = \infty$. Since, the reflection magnitudes for $R_s = 0$ and $\infty$ are 1 (i.e., 0 dB), their behavior is not shown here. It is observed that the absorption behavior takes different forms depending on the value of $R_s$. By varying the value of $R_s$ one can notice the change in the absorption level of one of the reflection nulls associated with the perturbed HIS resonances (similar to the case of 45°, discussed above). Based on this observation, we fix the range for $R_s$ where perfect reflection nulls can be obtained. From Fig. 3.16 it is clear that for sheet resistivities corresponding to $R_s = 60.8\,\Omega$ and $294.6\,\Omega$, we have perfect reflection nulls at frequencies 5.845 GHz and 12.77 GHz, respectively. Hence, the range of $R_s$ for the plane wave incident at 30° is given to be (60.8 to 294.6) $\Omega$. A similar procedure is repeated for 45° and 60°, and the ranges for $R_s$ are found to be $(70.56 - 241.8)\,\Omega$ and $(94.03 - 146.38)$ $\Omega$, respectively. Then, based on these values of $R_s$, a unique range that fits for all angles of incidence (up to 60°) can be found: $(94.03 - 146.38)$ $\Omega$

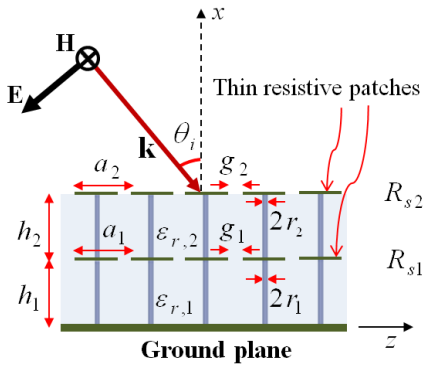


**Figure 3.17.** Two-layer mushroom-type HIS absorber with thin resistive patches. Structural parameter used in this work: $h_1 = h_2 = 3.2\,\text{mm}$, $\varepsilon_{r,1} = 2.2$, $\varepsilon_{r,2} = 1.33$, $r_1 = r_2 = 0.05\,\text{mm}$, $a_1 = a_2 = 5\,\text{mm}$, $g_1 = g_2 = 0.1\,\text{mm}$, $R_{s1} = 196\,\Omega$, $R_{s2} = 1078\,\Omega$.

for the case under study. A further optimization procedure limited to the above range gives us an optimum value of $R_s = 106.54\,\Omega$, which is the one used in the absorber design in Fig. 3.11.

### 3.3.4 Two-layer Mushroom Structure with Thin Resistive Patches

The absorber described in Section 3.3.3 is a single-layer structure with only a few degrees of freedom available to be used for the design of an absorber over a wider range of frequencies. To improve the performance of the single-layer structure by increasing the degrees of freedom, a two-layer structure with the geometry shown in Fig. 3.17 is considered. The absorber consists of two resistive patch arrays separated by dielectric slabs perforated with metallic vias, with a ground plane at the bottom. For simplicity, in this work, we consider the case of wires with the same radii. The parameters of the dielectric slabs used in the design together with the dimensions and sheet resistivity values of the square patches are given in the caption of Fig. 3.17.

The reflection coefficient of the absorber for oblique angles of incidence obtained by the analytical model is shown in Fig. 3.18, and compared with the HFSS results. The comparisons illustrate the effectiveness of our model, where a good agreement

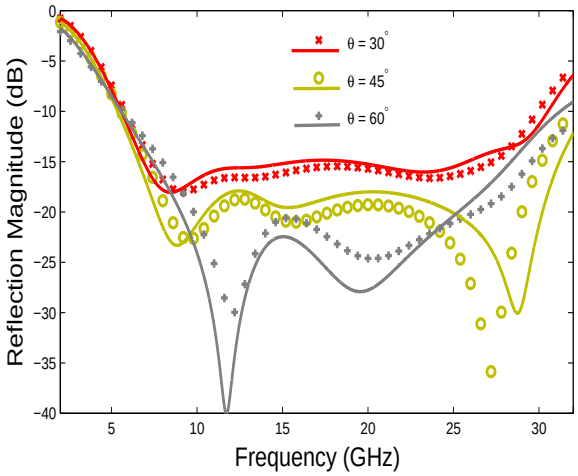


**Figure 3.18.** Comparison of analytical (solid lines) and full-wave HFSS results (crosses, circles, and plus signs) of the reflection coefficient for the two-layer mushroom HIS absorber excited by a TM-polarized plane wave at oblique angles of incidence $\theta$.

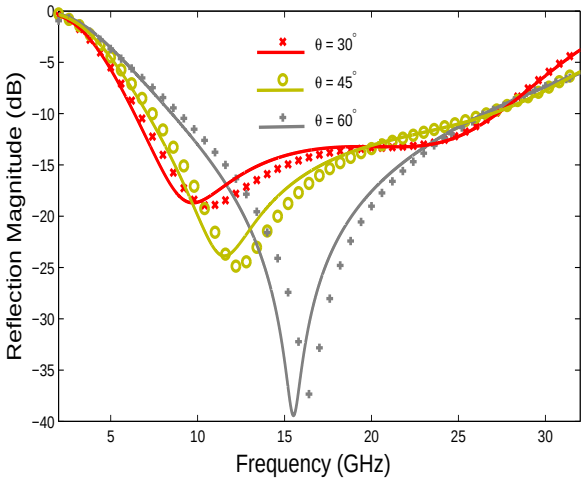


**Figure 3.19.** Comparison of analytical (solid lines) and full-wave HFSS results (crosses, circles, and plus signs) of the reflection coefficient for the two-layer HIS absorber (without vias) excited by a TM-polarized plane wave at oblique angles of incidence $\theta$.

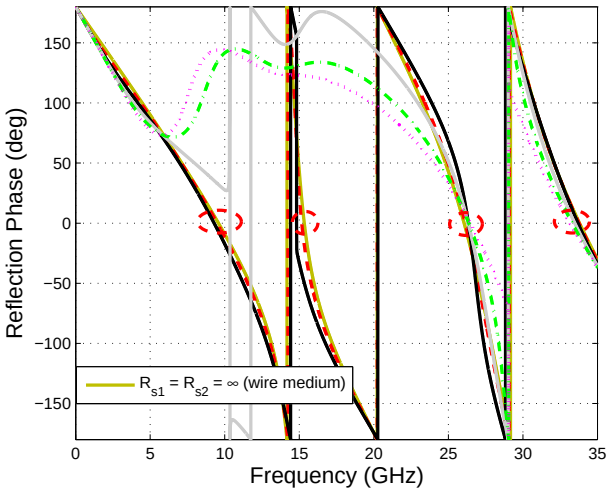


(a)

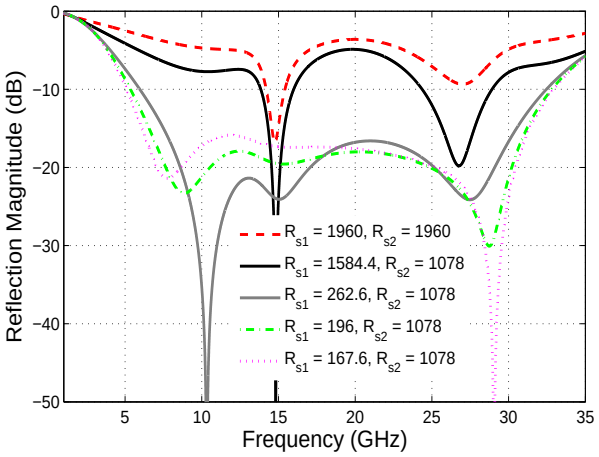


(b)

**Figure 3.20.** (a) Phase and (b) magnitude of the reflection coefficient of the two-layer mushroom structure for different values of sheet resistivity $R_s$ (in $\Omega$), $\theta = 45°$.

is observed in the entire frequency band for all angles of incidence. In particular, it verifies the possibility of the accurate modeling of the doubled-sided wire media with thin resistive patches at the junctions, using the proposed ABCs. This would not be possible using the local model [71] (which is based on the fact that the charge build up diminishes at the wire-to-patch junctions, such that the wire-medium slab can be homogenized as a uniaxial continuous ENG material), and hence, ABCs are essential to obtain the correct results (see [74, Fig. 5]). In general, the analytical model considered in this work is valid provided the radius of the vias is much smaller than the period $a$ and the spacing between the wires $a$ is much smaller than the wavelength in the host medium, $k_r a \ll 2\pi$ or $a \ll \lambda_r$, where $k_r = k_0\sqrt{\varepsilon_r}$ is the wave vector, $\lambda_r = \lambda_0/\sqrt{\varepsilon_r}$ is the wavelength, and $\varepsilon_r = \varepsilon_{r,1}$, with $\varepsilon_{r,1}$ being the largest permittivity of the dielectric materials used in the two-layer mushroom structure. However, it is noticed from Fig. 3.18 that at the highest operational frequency 32 GHz, $a \approx 0.79\lambda_r$, and surprisingly the model still captures the physics even beyond the homogenization limit. Hence, the condition $a \ll \lambda_r$ is not necessarily required to be strictly enforced, however, it is required that $a$ is sufficiently smaller than $\lambda_r$, provided the gap $g$ between the patches is small, $g \ll a$. Fig. 3.19 shows the results of the two-layer structure without vias. Clear differences can be seen when the results of Figs. 3.18 and 3.19 are compared. In Fig. 3.18 we see a significant enlargement of the absorption band for oblique angles of incidence, as compared to the case of no vias (Fig. 3.19). Also, Fig. 3.18 shows that the two-layer mushroom structure, while maintaining wide bandwidths, allows for the enhancement of the absorption for increasing angles of incidence. However, for the structure with no vias, the bandwidth decreases when the absorption increases. For example, for $\theta = 60^o$, it can be noticed that the 20 dB absorption bandwidth of the structure with vias covering the frequency band from 9.03 GHz to 25.29 GHz has a 55.5% bandwidth increase in comparison

to the structure without vias with the frequency band from 12.67 GHz to 18.86 GHz. Furthermore, it can be observed that the relative bandwidth of absorption of the two-layer structure studied in Figs. 3.18 and 3.19 increases with respect to the single-layer structure analyzed in Figs. 3.12 and 3.13. It should be noted that, although the proposed two-layer absorber shows improvement both in bandwidth and absorption for the obliquely incident TM-polarized plane waves, there can be a number of different optimized solutions with similar wideband results as those shown in Fig. 3.18. Designing an absorber with optimum performance is always a challenging task because of having a large number of degrees of freedom. Hence, by proper selection of dimensions and resistivities of the patch arrays, and thicknesses and permittivities of the dielectric slabs, one can obtain a better solution (i.e., wider bandwidth and increased absorption) than the one shown in Fig. 3.18. The design procedure described in Section 3.3.3 for the single-layer absorber can be used to obtain the values of $R_s$ in the design of the two-layer structure. Although this idea may seem trivial and simple to implement, the selection of the proper values of $R_s$ in the design of a wideband absorber is a tedious process (because of increased degrees of freedom) and, hence, the explanation of the design procedure is omitted here for the sake of brevity. One can use the numerical techniques [26, 27], to obtain better optimized values of $R_s$, however, this is not the subject of the present work.

In many applications it is desirable to have wideband absorption properties for both TM and TE polarizations. For TE illumination, although wideband absorption behavior is noticed, the stability of the absorption level decreases for increasing angles of incidences. This is due to the fact that, for TE illumination the electric field is orthogonal to the thin vertical metallic vias, and therefore the interaction will be negligible. Since the work carried out here deals with the interaction of incident field with the vertical vias, i.e., for obliquely incident TM-polarized plane wave, the results

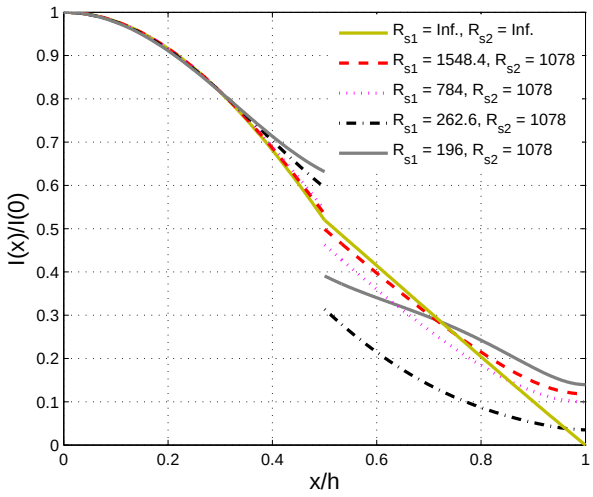


**Figure 3.21.** Normalized wire current in the two-layer mushroom structure for different values of sheet resistivity $R_s$ (in $\Omega$) at $f = 15$ GHz, $\theta = 45°$. Here $h$ is the total thickness of the two-layer structure given by $h_1 + h_2$.

for TE polarization are henceforth omitted.

For the single-layer structure, it was observed that the additional resonance of the mushroom structure is used to obtain wide bandwidths with enhanced absorption, and that the resonances resulting in wideband behavior are the perturbed HIS resonances of the mushroom structure with PEC patches. However, for the two-layer structure, the behavior of resonances and wide bandwidths are not due to the perturbation of the structure with PEC patches ($R_s = 0$), but due to the perturbation of the resonances of the wire-medium slab ($R_s = \infty$). To explain this we study in Fig. 3.20 the reflection properties (phase and magnitude) of the structure for different resistivities of the patch arrays for a TM-polarized plane wave incident at 45°. Starting with the wire-medium slab case (i.e., $R_s = \infty$), the reflection phase behavior shows four resonances (shown in red circles in Fig. 3.20(a) corresponding to the zero phase). The variation of resistivities of the patch arrays can be done in many ways, for example by decreasing $R_s$ in both layers at the same time or decreasing $R_s$ in one layer with the other layer fixed. We employ the latter strategy, because the aim is to explain the wideband behavior of the absorber with $R_{s1} = 196\,\Omega$ and $R_{s2} = 1078\,\Omega$. By gradually

decreasing the resistivity of the patch array in the bottom layer (with the resistivity of the top patch array being fixed), it is noticed that the phase behavior starts to deviate from the wire-medium slab case (shown in Fig. 3.20(a)). It is also observed from the magnitude behavior shown in Fig. 3.20(b) that the absorption levels of the reflection minima shift with decreasing values of $R_s$, and for some cases there are perfect reflection nulls (similar to the behavior observed in a single-layer mushroom structure) corresponding to the zero phases of the perturbed HIS resonances of the wire-medium slab. This proves the fact that the reflection minima shown in Fig. 3.18, for the case of $R_{s1} = 196\,\Omega$ and $R_{s2} = 1078\,\Omega$ are associated with the perturbed HIS resonances of the actual wire-medium slab. Bandwidth enhancement with respect to the single-layer mushroom structure is also observed for small angles of incidence (results not shown here). In this case, the influence of the vias is almost negligible since the electric field is almost orthogonal to the vias. The bandwidth enhancement is then explained in terms of the mutual interactions between patches printed in the adjacent layers. For higher angles of incidence, the role of vias is dominant and they are responsible for the widening of the useful frequency band. Hence, by using the resonances of the mushroom structure, along with the proper choice of dimensions and resistivities of the patch arrays, and with good selection of the permittivities of the dielectric slabs (perforated with metallic vias) the absorption bandwidth can be enlarged, as compared to the case with no vias.

The behavior of the current along the vias has also been studied for various resistivities of the patch arrays. Figure 3.21 shows the normalized wire current in the two-layer mushroom structure at $f = 15\,\text{GHz}$. The aim is to verify that the resonances resulting in the wideband behavior shown in Fig. 3.20 are actually due to the perturbation of the HIS resonances of the wire-medium slab. For the values of $R_s$ used in Fig. 3.20(b), it can be observed from Fig. 3.21 that the current along the

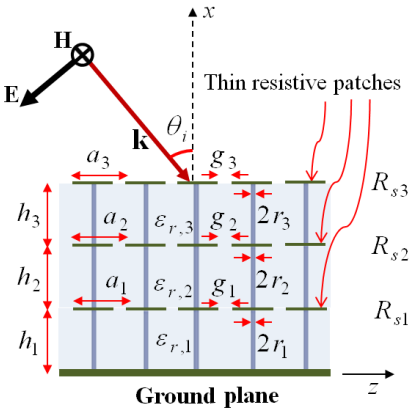


**Figure 3.22.** Three-layer mushroom-type HIS absorber with thin resistive patches. Structural parameter used in this work: $h_1 = 2.7\,\text{mm}$, $h_2 = h_3 = 3.2\,\text{mm}$, $\varepsilon_{r,1} = 3.2$, $\varepsilon_{r,2} = 1.8$, $\varepsilon_{r,3} = 1.33$, $r_1 = r_2 = r_3 = 0.05\,\text{mm}$, $a_1 = a_2 = a_3 = 5\,\text{mm}$, $g_1 = g_2 = g_3 = 0.1\,\text{mm}$, $R_{s1} = 196\,\Omega$, $R_{s2} = 588\,\Omega$, $R_{s3} = 1176\,\Omega$.

metallic vias varies significantly, indicating that the spatial dispersion effects are not suppressed. The reason is that when the $R_s$ is large (conductivity is small), the thin resistive patch resembles a dielectric rather than a metal, and charges accumulate at the tip of the double-sided wire-to-patch junction, which necessitates the ABCs derived in Section 3.2. This behavior is consistent with the study reported in [74] for small values of $\sigma_{2D}$, however, it should be noted that the structure in that paper has a single-sided wire-to-patch junction. Hence, from the behavior of the current (nonuniformity) and the phase behavior (perturbed), the resonances of the absorber are indeed the perturbed HIS resonances of the wire-medium slab.

### 3.3.5 Three-layer Mushroom Structure with Thin Resistive Patches

The purpose of this section is to show that the analytical model derived in Section 3.2 can be applied to model a large number of mushroom structure layers (with double-sided wire-to-thin-resistive-patch junctions). The structure consists of three resistive patch arrays separated by dielectric slabs perforated with metallic vias, with a ground plane at the bottom (with the geometry shown in Fig. 3.22). The parameters of the

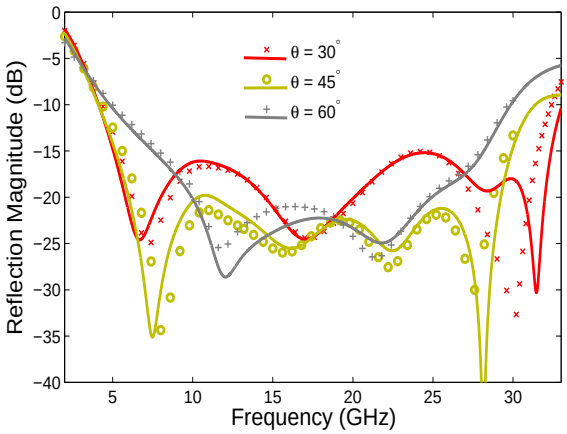


**Figure 3.23.** Comparison of analytical (solid lines) and full-wave HFSS results (crosses, circles, and plus signs) of the reflection coefficient for the three-layer mushroom HIS absorber excited by a TM-polarized plane wave at oblique angles of incidence $\theta$.

dielectric slabs together with the dimensions and sheet resistivities of the square patches are given in the caption of Fig. 3.22. In Fig. 3.23 the magnitude of the reflection coefficient is plotted for different incidence angles. The results obtained using the analytical model described in Section 3.2 agree very well with the HFSS results. It is also observed that, as the incidence angle increases, the interaction with the vias grows and absorption is increased, as expected. Finally, Fig. 3.24 shows the magnitude of the reflection coefficient of the absorber without vias, with the parameters in the caption of Fig. 3.22. By comparing Figs. 3.23 and 3.24 one can clearly see significant improvements in the absorption bandwidth for increasing angles of incidence. For example, for $\theta = 60^{\circ}$, the 20 dB absorption bandwidth of the structure with vias covering the frequency band from 9.93 GHz to 24.93 GHz shows a 38 % increase in the bandwidth when comparing to the structure with no vias, having the bandwidth from 9.01 GHz to 14.6 GHz. Also, it should be noted that the HFSS results shown in Fig. 3.23 for $\theta = 45^{\circ}$ and $60^{\circ}$ have been obtained up to 30 GHz only (due to lack of convergence at higher frequencies). Further, it should be noted that, due to high resistivity of the top patch arrays in the two-layer and three-layer mushroom structures (i.e., with $R_{s2} = 1078\Omega$ in the two-layer, and $R_{s3} = 1176\Omega$ in

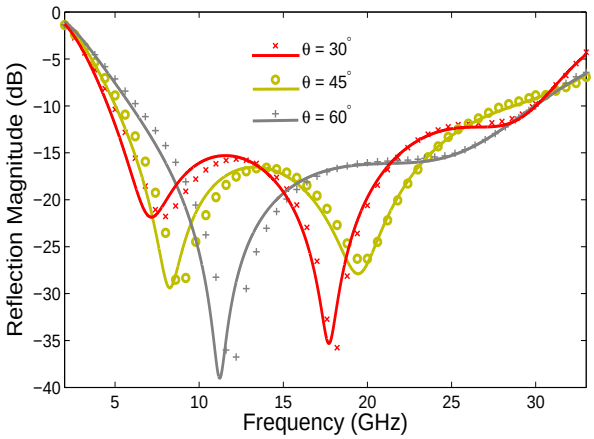


**Figure 3.24.** Comparison of analytical (solid lines) and full-wave HFSS results (crosses, circles, and plus signs) of the reflection coefficient for the three-layer HIS absorber (without vias) excited by a TM-polarized plane wave at oblique angles of incidence $\theta$.

the three-layer), one can replace them with solid resistive sheets with same resistive values, without causing much deviations in the absorption behavior. This is because the resistivity in these cases dominates the capacitive impedance of the patch array, and hence the gaps in these patches can be neglected.

## 3.4 Conclusions

A simple analytical model has been presented to analyze the reflection properties of multilayered mushroom HIS structures with thin resistive patches. Additional boundary conditions for the double-sided junctions of wire media with thin resistive patches at the interface have been obtained. The limitations and applicability of the new boundary conditions have been studied, particularly for the two-layer mushroom structure, and the analytical model results have been verified using full-wave simulations. It is observed that the model gives accurate results when $g \ll a$ for small and moderate values of the patch resistivity, however, for large values of $g$, the value of $R_s$ should be large. Further, a design procedure for selecting resistivities of the patch arrays has been presented. By using the resonances of the mushroom and wire-medium HIS structures, we have shown that the absorption band can be

enlarged with enhanced absorption for obliquely incident TM-polarized plane waves, when compared to the structure without vias. Also, it is observed that for the single-layer mushroom absorber (with small resistivities of the patch arrays) the resonances resulting in the wideband behavior are indeed the perturbed HIS resonances of the mushroom structure with PEC patches. However, for the two-layer structure it is observed that the resonances resulting in the wideband behavior are the perturbed resonances of the wire-medium slab.

# CHAPTER 4

# ANALYSIS AND DESIGN OF CONFORMAL MANTLE CLOAKS FOR CYLINDRICAL OBJECTS USING PRINTED AND SLOTTED ARRAYS: ANALYTICAL APPROACH

Following the idea of "cloaking by a surface" [Alù, Phys. Rev. B 80, 245115 (2009); Chen, Alù, Phys. Rev. B 84, 205110 (2011)], we present a rigorous analytical model applicable to mantle cloaking of cylindrical objects using 1-D and 2-D sub-wavelength conformal frequency selective surface (FSS) elements. The model is based on Lorenz-Mie scattering theory which utilizes the two-sided impedance boundary conditions at the interface of the sub-wavelength elements. The FSS arrays considered in this work are composed of 1-D horizontal and vertical metallic strips and 2-D printed (patches, Jerusalem crosses, and cross dipoles) and slotted structures (meshes, slot-Jerusalem crosses, and slot-cross dipoles). It is shown that the analytical grid-impedance expressions derived for the planar arrays of sub-wavelength elements may be successfully used to model and tailor the surface reactance of cylindrical conformal

mantle cloaks. By properly tailoring the surface reactance of the cloak, the total scattering from the cylinder can be significantly reduced, thus rendering the object invisible over the range of frequencies of interest (i.e., at microwaves and far-infrared). The results obtained using our analytical model for mantle cloaks are validated against full-wave numerical simulations.

## 4.1 Introduction

Achieving invisibility with electromagnetic metamaterials has been discussed in a variety of possible scenarios. One of the most successful approach is the coordinate transformation (CT) cloaking method, put forward by Pendry *et al* [77] and Leonhardt [78]. This technique is based on the principle of bending the electromagnetic waves around an object by utilizing a surrounding medium (cloak) with specific inhomogeneity and anisotropic properties. This ensures that the waves travel around the object with no reflection, thus making the region inside the cloak effectively undetectable. With recent improvements in metamaterial fabrication technology, experimental demonstrations have verified the CT method at microwaves [79] and visible frequencies [80, 81]. Since then there has been an increased interest in the study of electromagnetic cloaking realized with metamaterials, due to its vast significance and potential applications in camouflaging, non-invasive probing, and low observability, among others. Alternative approaches to metamaterial cloaking, which have recently received much attention include the plasmonic cloaking [82] and cylindrical transmission-line cloaking [83].

A common feature of all of the above mentioned cloaking techniques is that they utilize bulk volumetric metamaterials, which are not only difficult to realize but also have a finite thickness often comparable with the size of the region to be cloaked. To overcome this issue, recently a different cloaking technique [23–25] based on the

concept of mantle cloaking has been proposed to reduce the visibility of objects of various shapes. This technique is based on the scattering cancellation properties of the mantle cloak (realized using an ultra thin conformal metasurface) characterized by an average surface reactance of choice. By adjusting the parameters of the metasurface inclusions, one can achieve the desired surface reactance, which can effectively cancel the scattering from a given object, thus reducing its overall visibility. In these studies on mantle cloak, once the required average surface reactance has been analytically determined, the specific design of the metasurface has been carried out by optimizing numerically the shape and parameters of the metasurface elements, without necessarily providing a clear analytical recipe on the individual elements forming the metasurface.

In this work, we extend the reach of the mantle cloaking technique by presenting and utilizing closed-form analytical expressions of the surface reactance for several representative metasurface cloaks for cylindrical objects. We consider a variety of 1-D and 2-D sub-wavelength periodic FSS elements, such as strips, [35] mesh grids and patches, [34,35,37–39] Jerusalem crosses, [40,41] and cross dipoles. [42] We use a rigorous analytical model to describe the surface reactance of the mantle cloaks, extending the available models previously derived for planar configurations [34,35,37–42] to cylindrical shapes. The analysis is based on the Lorenz-Mie scattering theory, [43,84] which employs the two-sided impedance boundary conditions applied on the surface of the FSS elements. This tremendously facilitates the design of cylindrical mantle cloaks in realizing the required surface reactances, which can be used to reduce the overall scattering from a given object at the desired frequency of interest, and our results are accurately validated with full-wave simulations. In the following, we also discuss the underlying physical phenomena involved with mantle cloaking with conformal metasurfaces, the conditions of applicability of the analytical expressions

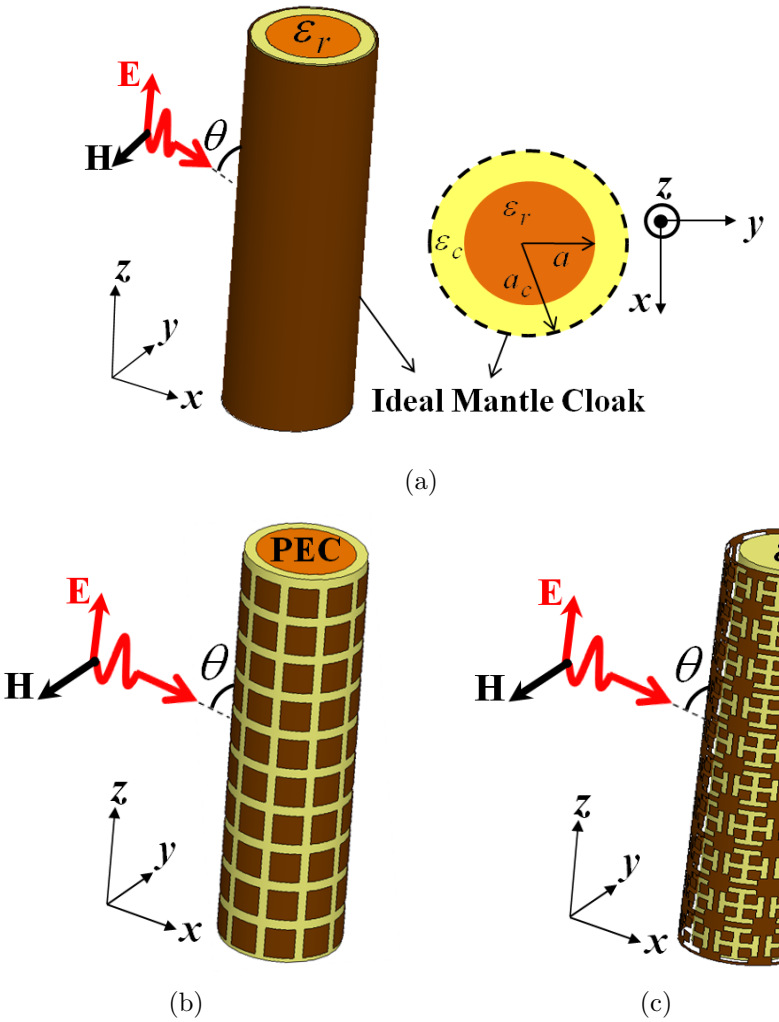


**Figure 4.1.** Schematics of the cylindrical objects coated by mantle cloaks: (a) infinite dielectric cylinder with an ideal mantle cloak, (b) infinite conducting cylinder with a conformal patch array, and (c) infinite dielectric cylinder with a conformal array of slotted Jerusalem crosses.

for cylindrical cloaks, and the robustness of the cloaking method by considering the frequency dispersion of the FSS elements. Moreover, the proposed model provides accurate design rules that provide very fast results when compared to the extensive numerical simulations with HFSS. [36]

The chapter is organized as follows. In Section 4.2, the formalism of our analytical model for the analysis of 2-D cylindrical objects covered by sub-wavelength conformal FSS elements is presented. In Sections 4.3 and 4.4, we focus on the applicability of the grid expressions for the cylindrical conformal printed and slotted cloaks (which have been originally derived for planar sub-wavelength elements), and then discuss under which conditions it is possible to significantly reduce the total scattering from a given object using various 1-D and 2-D sub-wavelength conformal FSS cloaks. Conclusions regarding the applicability of the analytical model are drawn in Section 4.5. The time dependence of the form $e^{j\omega t}$ is assumed and suppressed.

## 4.2 Theoretical Analysis

Consider a transverse magnetic (TM) polarized plane wave normally incident ($\theta = 90°$) on an infinitely long dielectric cylinder with relative permittivity $\varepsilon_r$, radius $a$, covered by a mantle cloak with radius $a_c$, with the space between the cloak and the cylinder filled by a dielectric of thickness $a_c - a$, and relative permittivity $\varepsilon_c$, as shown in Fig. 4.1(a). The mantle cloak in this work is realized using various commonly used patterned metasurfaces or FSS elements [some of the considered geometries are shown in Figs. 4.1(b) and 4.1(c)]. With the assumption that the unit-cell size of the FSS elements is much smaller than the wavelength of operation, the metasurface can then be characterized by an homogeneous surface impedance $Z_s$, which relates the macroscopic (averaged over the unit-cell) tangential electric field on the surface to the induced averaged electric surface current density: $\mathbf{E}_{\tan} = Z_s\mathbf{J}$. In terms of

effective circuit parameters, [34,35] $Z_s$ can be written as $R_s + jX_s$, where $R_s$ represents surface losses and $X_s$ takes into account the stored energy, and it can be either inductive ($X_s > 0$) or capacitive ($X_s < 0$) reactance of the FSS structure. In the lossless case, we have $Z_s = jX_s$, i.e., $R_s = 0$. In the limiting cases of $X_s \to \pm\infty$, we have a dielectric cylinder with no cloak, as the metasurface does not interact with the impinging field (no induced surface currents). The scattering problem is solved by applying the Lorenz-Mie scattering theory, [43,84] along with the following boundary conditions: (i) continuity of tangential components of electric and magnetic fields at the boundary of the core ($\rho = a$) and (ii) two-sided impedance boundary conditions at the interface of the mantle cloak ($\rho = a_c$). The two-sided impedance boundary conditions establish that the tangential electric $E_t$ and magnetic $H_t$ fields can be related via the sheet impedance, i.e.,

$$E_t|_{\rho=a_c^+} = E_t|_{\rho=a_c^-} = Z_s \left( H_t|_{\rho=a_c^+} - H_t|_{\rho=a_c^-} \right), \tag{4.2.1}$$

where $Z_s$ is the surface impedance of the mantle cloak covering the cylinder. Figures 4.1(b) and 4.1(c) show some of the mantle cloak geometries that we have considered in our design, which can provide the necessary surface reactances. These canonical FSS designs have been well characterized in planar configurations, and accurate analytical expressions for their averaged surface impedances are available for a plane-wave incidence. Details of these analytical expressions for various planar periodic sub-wavelength elements (strips, meshes, patches, Jerusalem crosses, cross dipoles, slotted Jerusalem crosses, and slotted cross dipoles), which are used in the design of mantle cloaks in the following, are provided in the Appendix. Analytical expressions for cylindrical FSS periodic arrays are not available in the literature, but since the inclusions are deeply sub-wavelength in our designs and the radius of curvature is infinite in the direction of polarization of the impinging electric field, one may expect that these formulas may still hold with a good degree of accuracy.

We verify this hypothesis in the next sections with full-wave simulations. Once the surface impedance is known, the scattering problem may be solved and the total bi-scattering width (SW) ($\phi = 0$), which is a quantitative measure of the detectability of the cylinder, is given by

$$\sigma = \frac{4}{k_0} \sum_{n=-\infty}^{\infty} |c_n^{\mathrm{TM}}|^2, \tag{4.2.2}$$

where $c_n^{\mathrm{TM}} = -P_l^{\mathrm{TM}}/(P_l^{\mathrm{TM}} + jQ_l^{\mathrm{TM}})$ is the $n^{\mathrm{th}}$ cylindrical scattering harmonic, which may be suppressed if $P_l^{\mathrm{TM}}$ is zero. The values of $P_l^{\mathrm{TM}}$ and $Q_l^{\mathrm{TM}}$ are given by:

$$P_l^{\mathrm{TM}} = \begin{vmatrix} J_n(ka) & J_n(k_c a) & Y_n(k_c a) & 0 \\ \frac{1}{\eta} J_n'(ka) & \frac{1}{\eta_c} J_n'(k_c a) & \frac{1}{\eta_c} Y_n'(k_c a) & 0 \\ 0 & J_n(k_c a_c) & Y_n(k_c a_c) & J_n(k_0 a_c) \\ 0 & \frac{1}{\eta_c} Z_s J_n'(k_c a_c) + j J_n(k_c a_c) & \frac{1}{\eta_c} Z_s Y_n'(k_c a_c) + j Y_n(k_c a_c) & \frac{1}{\eta_0} Z_s J_n'(k_0 a_c) \end{vmatrix},$$

$$Q_l^{\mathrm{TM}} = \begin{vmatrix} J_n(ka) & J_n(k_c a) & Y_n(k_c a) & 0 \\ \frac{1}{\eta} J_n'(ka) & \frac{1}{\eta_c} J_n'(k_c a) & \frac{1}{\eta_c} Y_n'(k_c a) & 0 \\ 0 & J_n(k_c a_c) & Y_n(k_c a_c) & -Y_n(k_0 a_c) \\ 0 & \frac{1}{\eta_c} Z_s J_n'(k_c a_c) + j J_n(k_c a_c) & \frac{1}{\eta_c} Z_s Y_n'(k_c a_c) + j Y_n(k_c a_c) & -\frac{1}{\eta_0} Z_s Y_n'(k_0 a_c) \end{vmatrix}, \tag{4.2.3}$$

where $\eta = \eta_0/\sqrt{\varepsilon_r}$ and $\eta_c = \eta_0/\sqrt{\varepsilon_c}$. By proper selection of $\varepsilon_c$, $a_c$, and $X_s$, the value of $P_l^{\mathrm{TM}}$ can be made zero, which would reduce the overall scattering of the object. Provided that the $l^{\mathrm{th}}$ scattering order dominates the scattering of the object, this may lead to a drastic suppression of the overall visibility. For transverse electric (TE) polarization, the expressions for scattering coefficient and SW can be easily obtained by electromagnetic duality. It should be noted here that the above formulation holds as along as the polarization coupling is negligible, i.e., when pure TM or TE incident cylindrical waves excite only TM or TE scattered waves, respectively. This ideally holds only for a normal incidence or for objects with a small transverse cross-section.

In the more general case of oblique incidence, where polarization coupling is present, Eq. 4.2.2 can be modified to include TM-TE coupling, as discussed in Ref. [85].

## 4.3 1-D cylindrical cloaks

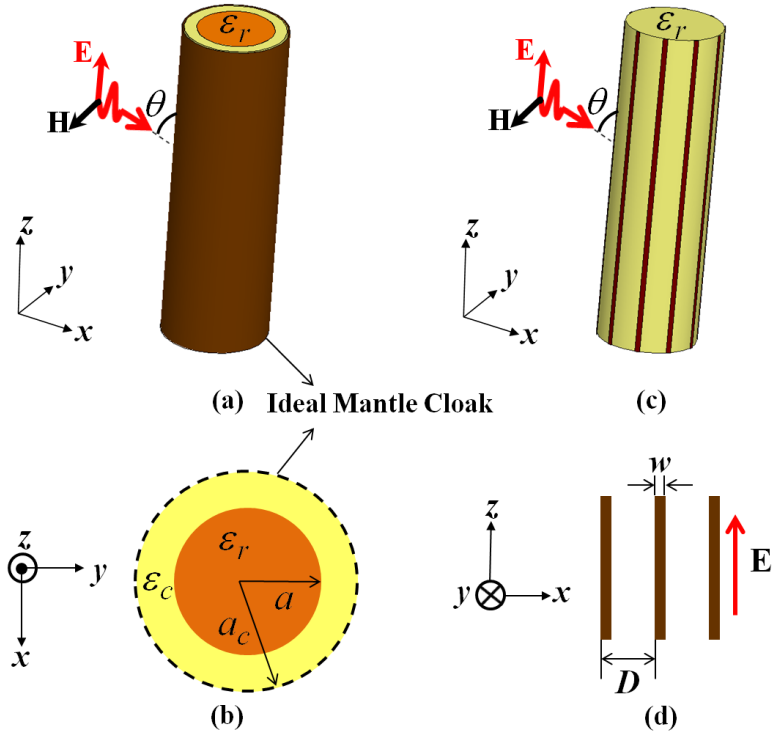


**Figure 4.2.** Geometries of the cylindrical structures covered by mantle cloaks: (a) 3-D view of the infinite dielectric cylinder with an ideal mantle cloak, (b) top-view of (a), (c) 3-D view of the dielectric cylinder with a conformal array of vertical strips, and (d) periodic grid of the planar vertical strips.

In this section, the scattering properties of 2-D cylindrical objects (such as dielectric and PEC cylinders) covered by 1-D conformal sub-wavelength metallic FSS elements (such as strips, shown in Fig. 4.2(d)) are studied using the analytical model formalism presented in Section 4.2. At first we study the scattering of the cylinders covered by an ideal lossless and dispersionless reactive mantle cloak at the frequency of interest and determine under which conditions (inductive or capacitive reactance) it is possible to reduce (cancel) the scattering from the cylinder making it invisible.

The required surface reactance of the ideal mantle cloak is then realized using the 1-D FSS elements (shown in Fig. 4.2(d)), whose analytical grid-impedance expressions in the planar case are given in appendix (Eq. A.1.2). Although, the expressions are derived for the planar case, here, we use them to model and tailor the properties of the cylindrical FSS cloaks, and show that under the sub-wavelength conditions (of the size of the elements) this approximation is valid. Further, we validate the results obtained using our analytical model with the numerical simulations.

### 4.3.1 Dielectric cylinder

To demonstrate the concept of mantle cloaking using FSS elements, we begin with the analysis of the scattering properties (or SW) of the dielectric cylinder with $\varepsilon_r = 10$ and radius $a = \lambda_0/10$ ($\lambda_0$ is the free-space wavelength at the design frequency $f_0$), covered by an ideal mantle cloak with radius $a_c$, as shown in Fig. 4.2(a). The mantle cloak is characterized by a homogeneous lossless and dispersionless surface reactance $X_s$. Fig. 4.3(a) shows the variation of the normalized SW of the dielectric cylinder as a function of $X_s$ of the mantle cloak for a TM-polarized plane-wave at normal incidence ($\theta = 90°$) for various values of $a_c$. It can be seen from Fig. 4.3(a) that for large reactance values ($X_s \rightarrow \pm\infty$), the mantle cloak has no effect on scattering (shown using the dashed grey line), i.e., there is no cloak on the cylinder, but for some specific inductive values, there is a significant reduction in the scattering. In particular, for the conformal cloak, $a_c = a$, maximum scattering cancellation occurs at $X_s = 52\ \Omega$, i.e., the mantle cloak surface reactance should be inductive to render the cylinder invisible at the design frequency. Also, one can notice that with an increase in the radius of the mantle cloak, the level in dB of the SW decreases, however, the scattering reduction is still significantly higher (for example for $a_c = 1.1a$, with $X_s = 29\ \Omega$, the level in dB is around $-20$ dB) which ensures that the object

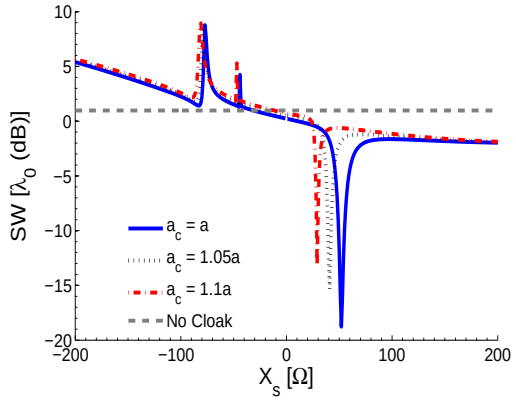


(a)

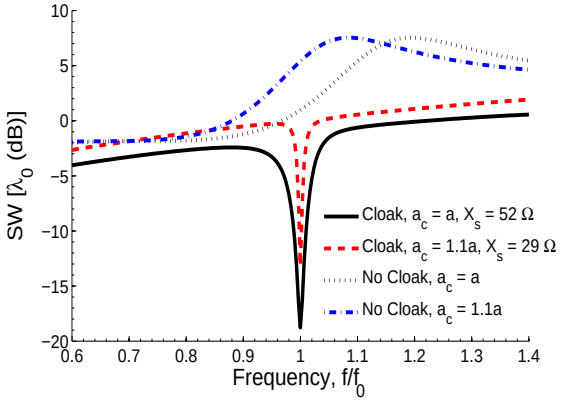


(b)

**Figure 4.3.** Variation of the normalized SW: (a) of the infinite dielectric cylinder versus surface reactance of a conformal mantle cloak and (b) of the infinite dielectric cylinder with and without the mantle cloak versus frequency. The results shown here are calculated using the analytical model presented in Section 4.2.

can still be cloaked for larger radius of the mantle cloak. The physical mechanism behind this scattering reduction can be understood as the destructive interference at all angles between the fields radiated by the induced currents on the mantle cloak and the fields scattered by the dielectric cylinder. In order to realize the required surface reactance ($X_s = 49.8\ \Omega$, $a_c = a$), in the present work we use first a 1-D periodic array of metallic vertical strips (shown in Fig. 4.2(d)). This is an obvious

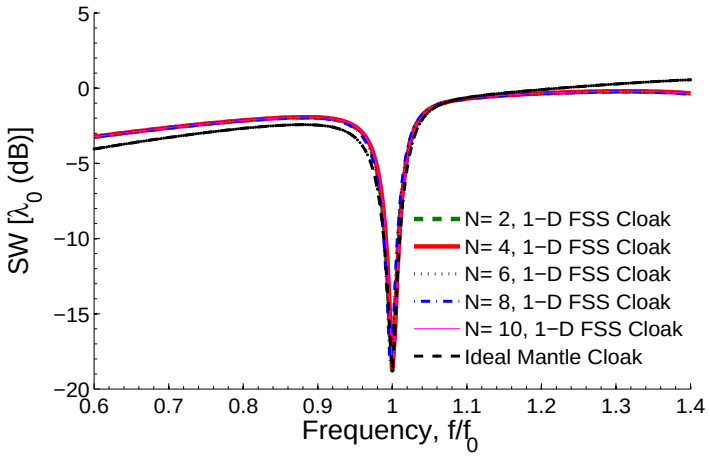


(a)

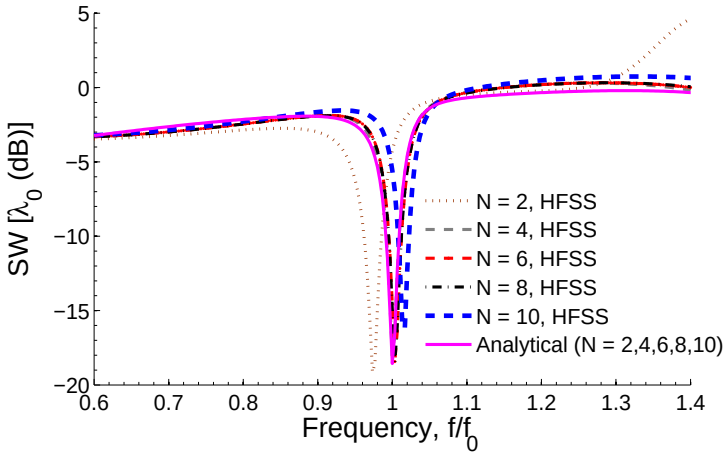


(b)

**Figure 4.4.** Variation of the SW versus frequency: (a) comparisons of the SW of an ideal mantle cloak with various periodicities of the 1-D FSS cloak calculated using the analytical model and (b) comparisons of analytical and full-wave results of the SW for various periodicities of the 1-D FSS cloak.

choice, because the vertical strips are very well known [34, 35, 39] to provide an inductive surface reactance in the planar configuration for electric field parallel to the strips (Fig. 4.2(d)). In this case, the averaged surface impedance has the analytical expression given in the Appendix (Eq. A.1.2). Obviously, the orientation of the strips plays a very important role in the design of the mantle cloak. Since cylinders with moderate cross-sections are dominated by TM scattering with electric field parallel to the cylinder axis, the mantle cloak strips should be oriented as in Fig. 4.2(c). We can expect that the analytical model in Eq. A.1.2, formally derived for a planar configuration, may still hold with a good accuracy in this cylindrical configuration, as long as the spacing between neighbouring strips is small, since the strips are not curved along their axis. The grid-impedance expression in Eq. A.1.2 is frequency dispersive and it also depends on the grid parameters, i.e., the period $D$ and width $w$. Since the vertical strips are positioned around the cylinder in the $\phi$-direction, the total number of strips $N$ depends on the periodicity $D$ of the FSS elements, i.e., $N = 2\pi a/D$. Table 4.1 shows the required design parameters for different values of $D$ and $w$, as the function of the number of strips around the cylinder, to produce the required surface inductance using Eq. A.1.2. In Fig. 4.4(a) we show the predicted frequency variation of the SW for different designs in Table 4.1, obtained after substituting the analytical expression for $Z_s$ given in Eq. A.1.2 in the expressions of $P_l^{\mathrm{TM}}$ and $Q_l^{\mathrm{TM}}$ (given in Ref. [25]), along with the SW of the ideal mantle cloak. It is clear that the inductive strips with different periodicities generate precisely the same SWs; however, they cannot reproduce the exact behavior of the ideal mantle cloak. This small discrepancy between the SWs is related to the fact that the inductive strip FSS is frequency dispersive. In Fig. 4.4(b), we compare these analytical results with full-wave simulations of mantle-cloaks with a different number of strips, using the same design parameters from Table 4.1. In the figure, only a single analytical curve is shown,

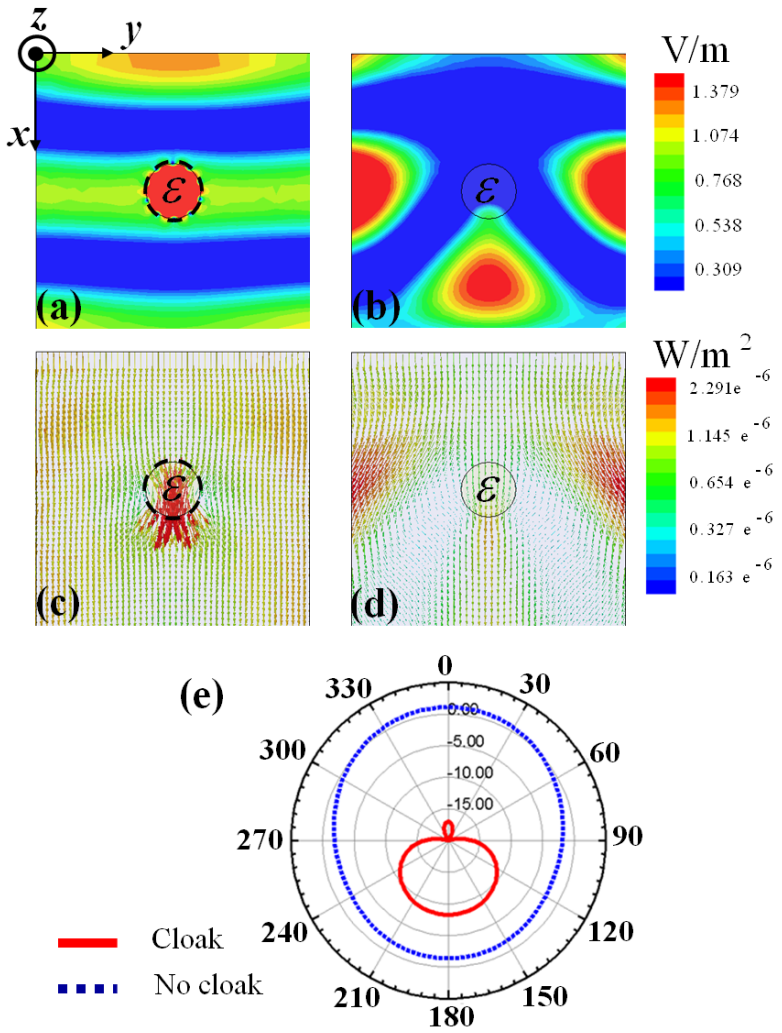


**Figure 4.5.** Full-wave numerical results of magnitude of **E**-field distributions on the $\phi$-plane: (a) with the vertical strips cloak and (b) without the cloak. Vector power-flow distributions on the $\phi$-plane: (c) with the vertical strips cloak and (d) without the cloak. Far-field radiation patterns for: (e) the infinite dielectric cylinder with and without the cloak.

**Table 4.1.** Parameters of the inductive strips for different number of strips ($N$) around the cylinder.

| N | $D$ | $w$ | $\varepsilon_r$ | $a_c = a$ |
|---|---|---|---|---|
| 2 | $\lambda_0/3$ | $\lambda_0/7$ | 10 | $\lambda_0/10$ |
| 4 | $\lambda_0/6$ | $\lambda_0/23$ | 10 | $\lambda_0/10$ |
| 6 | $\lambda_0/10$ | $\lambda_0/55$ | 10 | $\lambda_0/10$ |
| 8 | $\lambda_0/13$ | $\lambda_0/125$ | 10 | $\lambda_0/10$ |
| 10 | $\lambda_0/16$ | $\lambda_0/200$ | 10 | $\lambda_0/10$ |

because the analytical results for different $N$ overlap with good approximation. It is seen that, as $N$ increases, the numerical results move closer to the analytical results (shown by the pink solid curve). In particular, when $N > 2$, since the neighbouring strips do not feel the effect of the curvature and the planar model holds with very good accuracy.

To further show the effect of cloaking, in Fig. 4.5 we show the corresponding full-wave simulations of the near-field amplitude (Figs. 4.5(a) and 4.5(b)) and vector power-flow distributions (Figs. 4.5(c) and 4.5(d)), and far-field radiation patterns (Fig. 4.5(e)) of the cylinder with and without the 1-D periodic inductive strip cloak ($N = 10$, see Table 4.1 for design parameters), respectively. A plane wave travelling along the $+x$-direction with electric field parallel to the $z$-axis, illuminates the structures in all the cases. In the presence of the cloak, as shown in Fig. 4.5(a), the scattering from the cylinder is drastically suppressed in all directions and one can see uniform planar wavefronts of the **E**-field even in the very near-field of the cylinder, with the field penetrating through the object. As expected, the cylinder without the cloak scatters the impinging wave in all directions, as shown in Fig. 4.5(b). Figure 4.5(c) shows the vector power-flow distribution of the cloaked cylinder, emphasizing how most of the energy is drifted around and through the cloak without causing much perturbation. However, for the case of no cloak, shown in Fig. 4.5(d), it is clear that the power distribution is highly perturbed by the object, and one can

notice the shadow region in the forward direction. Figure 4.5(e) shows the far-field radiation patterns of the two scenarios, showing drastically reduced scattering for all observation angles when comparing cloak and no-cloak cases.

### 4.3.2 Conducting cylinder

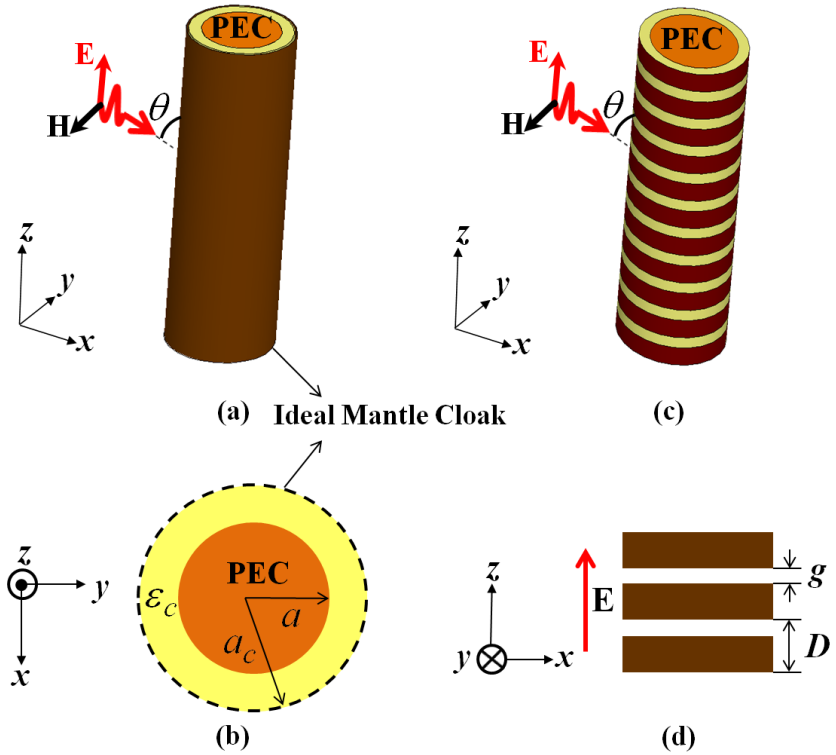


**Figure 4.6.** Geometries of the cylindrical structures coated by mantle cloaks: (a) 3-D view of the infinite conducting cylinder with an ideal mantle cloak, (b) top-view of (a), (c) 3-D view of the infinite conducting cylinder with horizontal strips, and (d) periodic grid of the planar horizontal strips.

We consider now a conducting cylinder with radius $a = \lambda_0/10$ covered by an ideal mantle cloak with radius $a_c$, characterized by a homogeneous, lossless, and dipersionless surface reactance $X_s$ (analogous to the dielectric cylinder discussed in Section 4.3.1), as shown in Fig. 4.6(a). In this case the field cannot penetrate the object and, unlike the dielectric scenario where the cloak can be conformed to the object, here, due to the zero impedance of the conducting cylinder, there must be a gap between the cloak and the object to avoid an electric short. Fig. 4.7(a) shows the

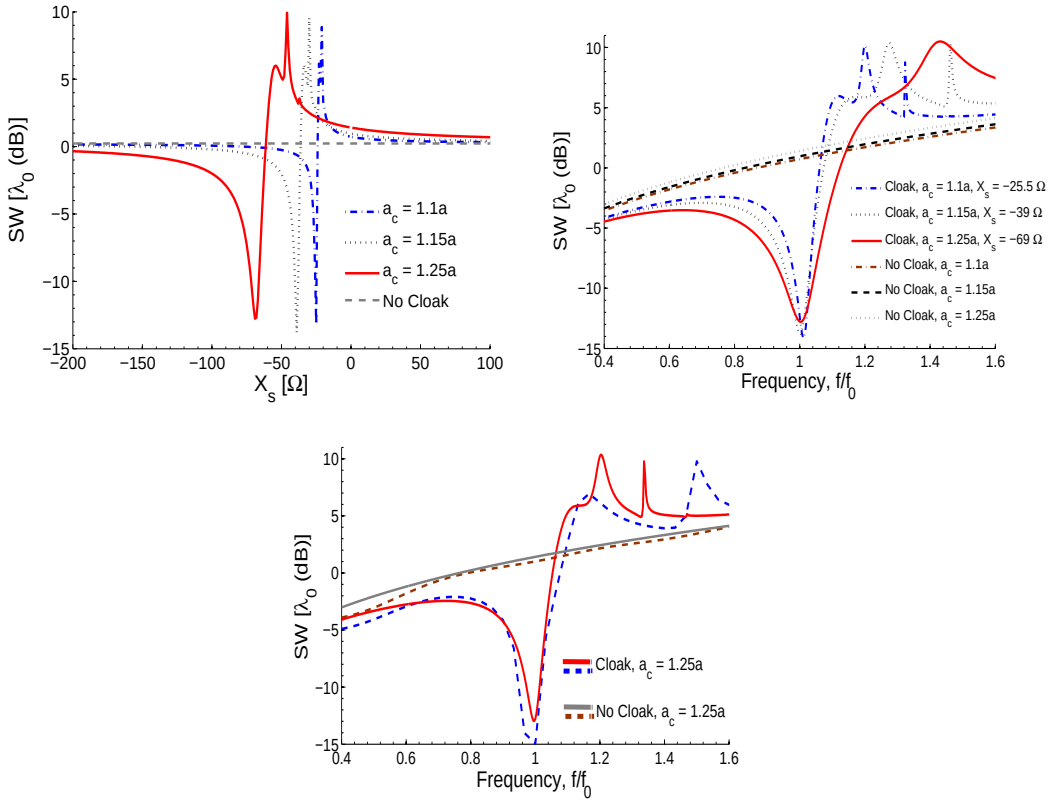


**Figure 4.7.** Variation of the normalized SW: (a) of the infinite metallic cylinder versus surface reactance of a conformal mantle cloak, (b) of the infinite metallic cylinder with and without mantle cloak versus frequency of operation, and (c) of the infinite metallic cylinder with and without capacitive ring array cloak versus frequency of operation. In (c) the analytical results are represented by solid lines and full-wave HFSS results by dot-dashed lines.

results of variation of SW versus $X_s$ for different radii of the mantle cloak. Here, it is seen that a mantle cloak with capacitive response may significantly reduce the overall scattering.For the cases $a_c = 1.1a$, $a_c = 1.15a$, and $a_c = 1.25a$ the corresponding values of surface reactances that give minimum SW at the design frequency are $X_s = -25\ \Omega$, $-39\ \Omega$, and $-69\ \Omega$, respectively. With these values of $X_s$, in Fig. 4.7(b), we show the variation of the SW versus frequency for two different radii of the ideal mantle cloak, along with the SW of the uncloaked cylinders of comparable crossections. It is clearly evident that at the design frequency one can notice the scattering cancellation (or null in the SW) for the cloaked cylinders for different radii of the

mantle cloaks, when compared to the SW of the uncloaked cylinders. Based on the required values of $X_s$, here we need to consider capacitive strips [34] to realize the required surface impedance, using the geometry shown in Fig. 4.6(d). Similar to the inductive strips case presented above, also here, the orientation of the capacitive strips is important in the cloak design. In this case, the **E**-field should be perpendicular to the direction of the strips to generate the capacitive response from the grid, as indicated in Fig. 4.6(d). This implies that horizontal capacitive rings, as sketched in Fig. 4.6(c), wrapped around the cylinder would constitute the best geometry to cloak conducting cylinders. Also in this case we use the analytical grid-impedance expression [34, 35] given in the Appendix (Eq. A.1.4), valid for the planar case, and we validate them against full-wave simulations to make sure that the curvature of the ring does not dramatically affect the local impedance value. We expect the model to be accurate, as long as the aspect ratio of the rings is large. We validate this model in Fig. 4.7(c) for $a_c = 1.25a$, and the required surface reactance is realized by choosing $D = \lambda_0/8$, $g = \lambda_0/69$, and a dielectric spacer (between the cloak and the metallic cylinder) with $\varepsilon_c = 10$. A significant reduction in scattering from the metallic cylinder is achieved also in this case, when compared to the case without cloak of comparable cross-section. In addition, the SW frequency dispersion calculated with full-wave numerical simulations agrees well with the analytical model based on Eq. A.1.4.

Figures 4.8(a) and 4.8(b) show the corresponding **E**-field distribution on the $(x - y)$ plane or azimuthal plane ($\phi$-plane) for the conducting cylinder with and without cloak, respectively, for a plane wave propagating in the $+x$-direction. It is clear that the capacitive ring mantle cloak can drastically suppress the scattering from the cylinder restoring quasi-planar field amplitudes in the near- and far-field regions. Similarly, Figs. 4.8(c) and 4.8(d) show the power-flow distribution on the $\phi$-plane for the conducting cylinder with and without the mantle cloak, respectively, verifying

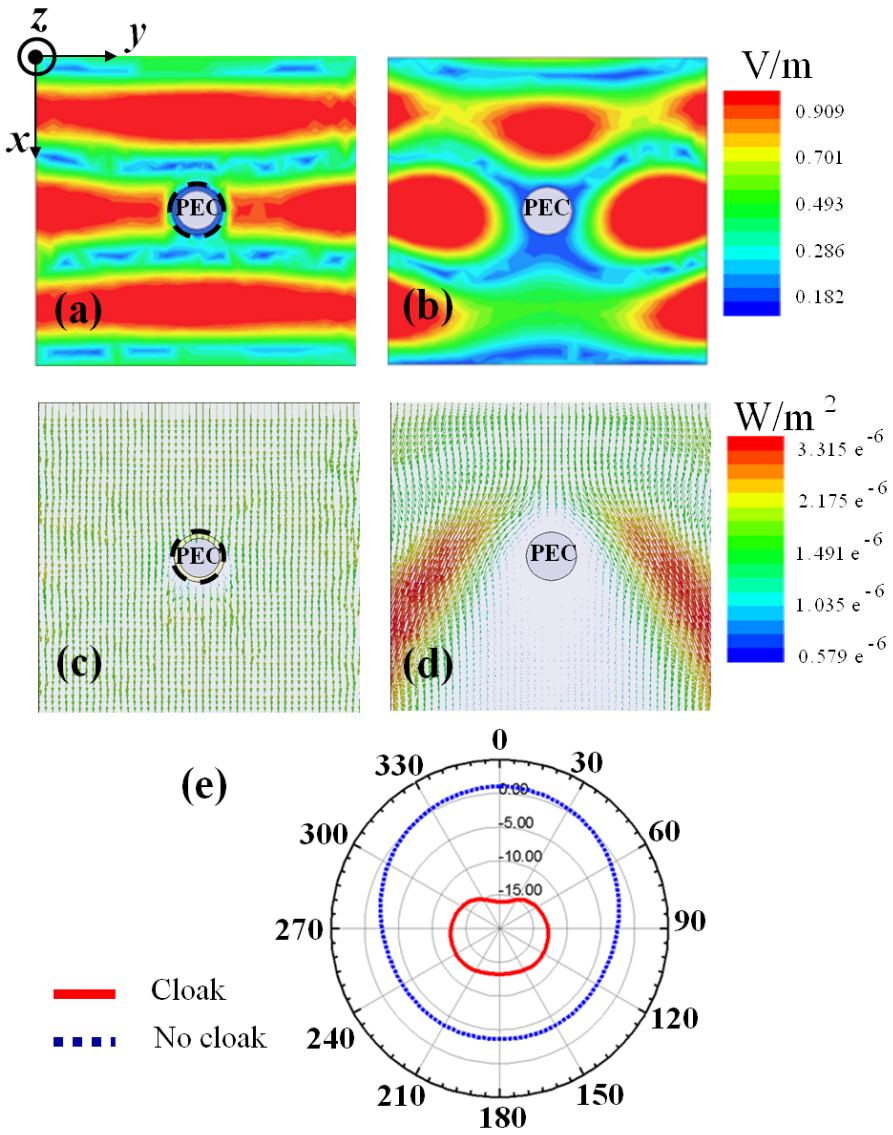


**Figure 4.8.** Full-wave numerical results of magnitude of **E**-field distributions on the $\phi$-plane: (a) with the horizontal strips cloak and (b) without the cloak. Vector power-flow distributions on the $\phi$-plane: (c) with the horizontal strips cloak and (d) without the cloak. Far-field radiation patterns for: (e) the infinite conducting cylinder with and without the cloak.

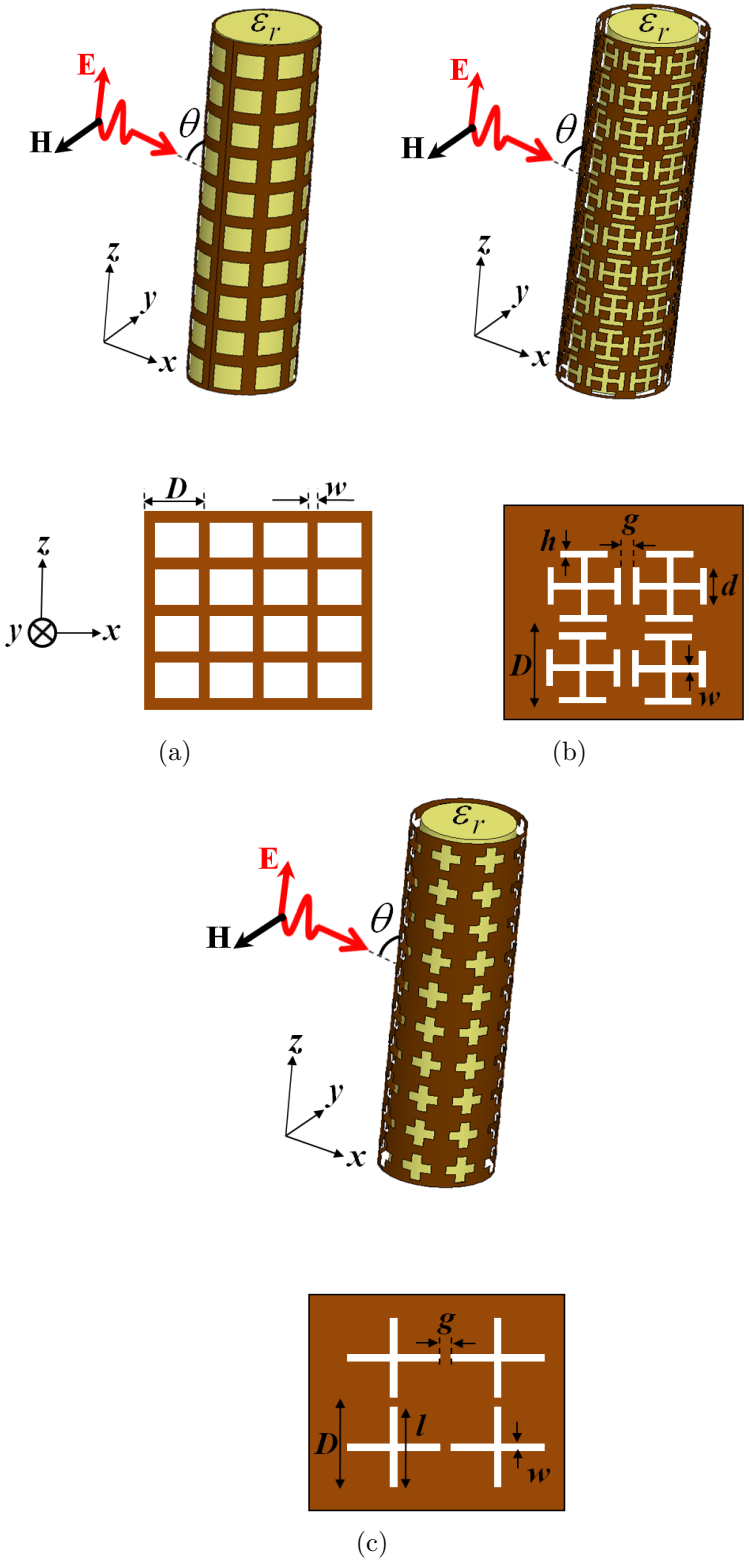


**Figure 4.9.** Schematics of the cylindrical structures covered by FSS mantle cloaks: (a) mesh grid cylindrical cloak, (b) slotted Jerusalem cross cylindrical cloak, and (c) slotted cross dipole cylindrical cloak.

that in the presence of cloak most of the energy is drifted around the cylinder without causing much perturbation. Finally, in Fig. 4.8(e), we show the corresponding far-field radiation patterns, confirming that the scattered field is suppressed quite significantly by the capacitive ring cloak for all observation angles.

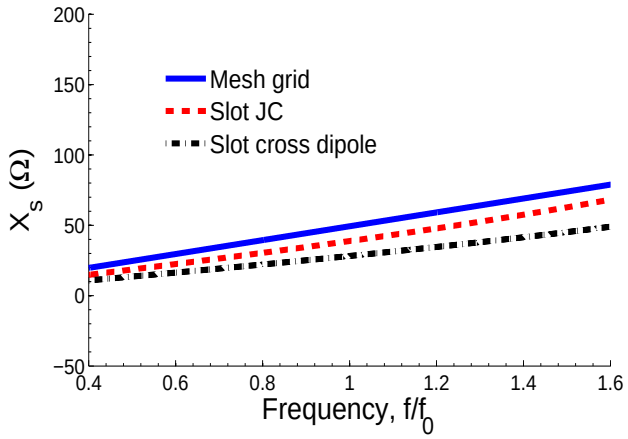


**Figure 4.10.** Variation of grid impedances of the three FSS structures versus frequency obtained using the grid-impedance expressions with parameters given in Table 4.2. The results shown here are calculated using the analytical grid-impedance expressions given in the Appendix.

It is obvious that, due to the 1-D geometry of the mantle cloak considered in this section, the scattering reduction is strongly dependent on the polarization of incidence. This is not an issue for dielectric cylinders with electrically small transverse cross-section, which are typically dominated by TM scattering. However, for conducting cylinders and thicker objects it may be desirable to realize more isotropic performance. To address this issue, in the next section we propose various 2-D periodic sub-wavelength patterned mantle cloaks which provide cloaking for both polarizations independent of the incidence plane.

## 4.4 2-D cylindrical cloaks

### 4.4.1 Dielectric cylinder

Extending the analysis carried out in the previous section, we focus here on mantle cloaks patterned with various 2-D sub-wavelength periodic elements. In general, it is not necessarily relevant to suppress the scattering for both TM and TE polarizations simultaneously at the same frequency. This is because, in the case of dielectric cylinders of moderate sizes, such as those considered in this work, the scattering is commonly dominated by one of the two responses. Thus, we concentrate on cancelling the TM-polarized scattering, which usually dominates the response for dielectric cylinders, and design an optimized cloak with maximum scattering suppression for this polarization. We then analyze its behavior for TE-polarized incident waves. Following the results in the previous section we need a 2-D conformal mantle cloak with inductive response. Here we propose three different suitable 2-D geometries, as depicted in Fig. 4.9: a mesh grid, slotted Jerusalem crosses, and slotted cross dipole arrays. In all cases, we consider the same periodicity along $z$- and $\phi$-direction.

**Table 4.2.** Parameters of the 2-D sub-wavelength inductive surface mantle cloaks with different conformal radii, $\epsilon_r = 10$, $a = \lambda_0/10$, and $\varepsilon_c = 1$.

| FSS type | $N$ | $D$ | $w$ | $g$ | $l$ | $d_1$ | $a_c$ |
|---|---|---|---|---|---|---|---|
| Mesh grid | 10 | $\lambda_0/16$ | $\lambda_0/200$ | - | - | - | $a$ |
| Slot-JC | 10 | $\lambda_0/15$ | $\lambda_0/200$ | $\lambda_0/650$ | - | $\lambda_0/22$ | $1.05a$ |
| Slot-cross dipoles | 4 | $\lambda_0/8$ | $\lambda_0/25$ | - | $\lambda_0/6$ | - | $1.1a$ |

The required surface reactance is tailored also in these cases by using the analytical grid-impedance expressions given in the Appendix (Eqs. A.2.6, A.2.22, and A.2.24), originally derived for planar surfaces. As explained in Section 4.3.1, these expressions should hold for cylindrical structures, as long as the dimensions of the elements and

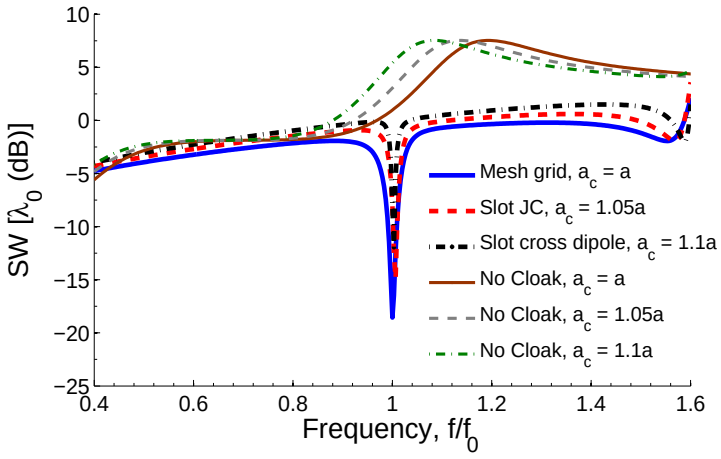


(a)

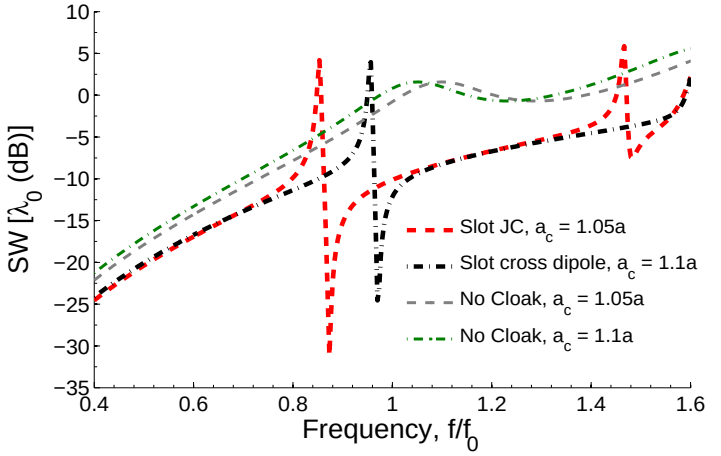


(b)

**Figure 4.11.** Variation of the SW of a dielectric cylinder with and without the FSS mantle cloaks versus frequency: (a) TM polarization and (b) TE polarization. The results shown here are calculated using the analytical model presented in Section 4.2. The results of the mesh grid structure for TE polarization are not included here.

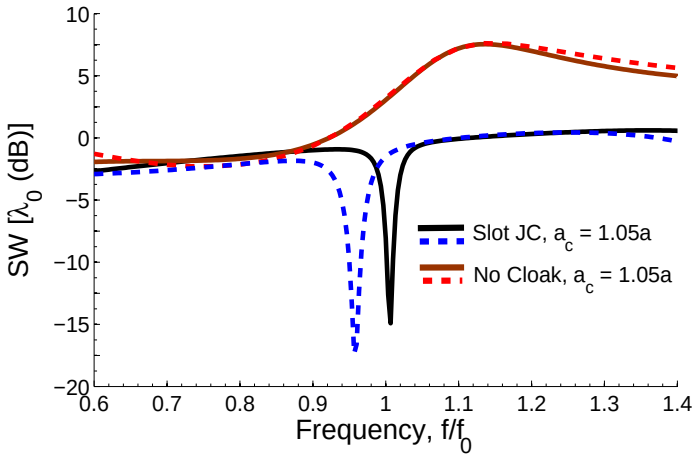


(a)

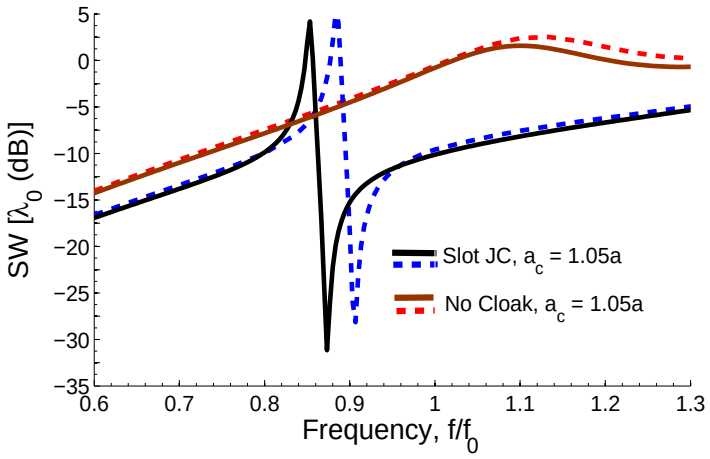


(b)

**Figure 4.12.** Variation of the SW of a dielectric cylinder with and without the slotted Jerusalem cross cloak versus frequency: (a) TM polarization and (b) TE polarization. The analytical results are represented by solid lines and full-wave simulation results by dashed lines.

periods among them are sub-wavelength and smaller than the local curvature. Using the available grid-impedance expressions and substituting them into the analytical formulas in Section 4.2, we optimize the cloak designs to obtain scattering cancellation at the design frequency using all the three structures. The optimal design parameters of the three FSS cloaks are given in Table 4.2 for different values of $a_c$.

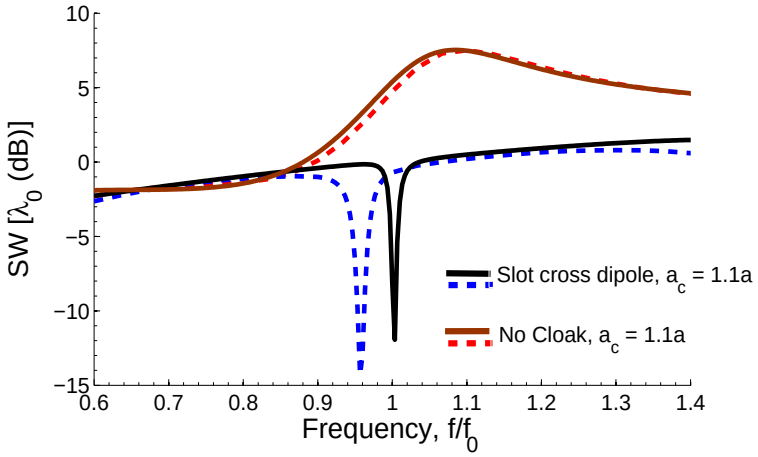


(a)

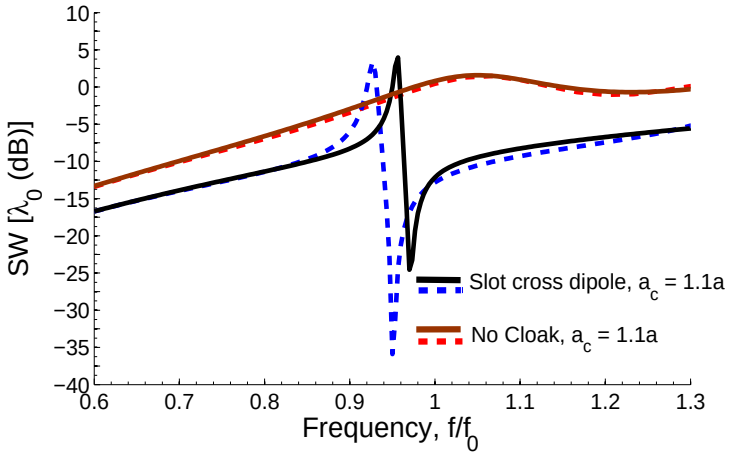


(b)

**Figure 4.13.** Variation of the SW of a dielectric cylinder with and without the slotted cross dipole mantle cloak versus frequency: (a) TM polarization and (b) TE polarization. The analytical results are represented by solid lines and full-wave simulation results by dashed lines.

In Fig. 4.10, we plot the grid impedances of the three structures using these optimized parameters. It can be seen that the grid impedance curves of the three FSS structures are almost identical with only small deviations at higher frequencies. Based on this fact, we next study the SW behavior of the three structures. Figure 4.11(a) shows the variation of the SW of the three FSS structures versus frequency for a TM-polarized illumination. Clearly, at the design frequency one can notice the scattering cancellation in all the three cases when compared to the uncloaked cylinders of comparable cross-sections. It should be noted that the medium between the dielectric cylinder object and the slotted Jerusalem cross and the slotted cross dipole cloaks is free space. We next analyze the behavior of the TM-optimized cloaks to TE-polarization incidence. Figure 4.11(b) shows the variation of the SW versus frequency for the dielectric cylinder covered by the TM-optimized slotted Jerusalem cross and slotted cross dipole mantle cloaks for a TE-polarized incident plane wave. Clearly, one can notice that scattering cancellation is achieved with the two structures even for TE incidence. However, the scattering minimum is achieved at slightly lower frequencies for the Jerusalem cross case. The SWs of the slotted Jerusalem cross and the slotted cross dipole structures for both TM and TE polarizations obtained by the analytical model (Figs. 4.11(a) and 4.11(b)) are shown in Figs. 4.12 and 4.13, and compared with the full-wave results. The comparisons illustrate the effectiveness of our model and verifies the accuracy of the grid-impedance analytical expressions in describing the surface reactance of conformal cylindrical cloaks. Here, the results of the mesh grid structure have not been included because the grid-impedance expression is not accurate for TE excitation. It can be noticed from Figs. 4.12 and 4.13 that the scattering behavior of the uncloaked cylinders for TE illumination is largely different from the TM case, due to the anisotropy in the shape of the object. Therefore, it may not be possible to design a mantle cloak with an isotropic $X_s$ that ensures a

scattering null at the same frequency (or design frequency) for both polarizations. Hence, the $X_s$ of the cloaks proposed here have been optimized to give a null at the design frequency for TM polarization (whose scattering is usually dominant) and a null close to the design frequency for TE polarization. An extension to anisotropic mantle cloaks that can suppress both polarizations may be envisioned, but it goes beyond the scope of the present work.

### 4.4.2 Conducting cylinder

Similar to the study carried out in Section 4.3.2, i.e., cloaking of conducting cylinders using 1-D sub-wavelength periodic elements, in this section we focus on extending the analysis to both TM and TE polarizations using 2-D sub-wavelength periodic elements. As stated before, the analysis here will be carried out for both polarizations based on a TM-optimized cloak design.

In this case, a capacitive surface reactance is required to suppress the scattering from the cylinder. To realize this reactance, here we use the complementary cases of the 2-D sub-wavelength elements studied in Section 4.4.1, i.e., 2-D arrays of printed patches, Jerusalem crosses, and cross dipoles (whose geometries are shown in Fig. 4.14). Since, the dimensions of the periodic elements considered in this work and their relative distances are sub-wavelength, the grid-impedance expressions given in Appendix (Eqs. A.2.20, A.2.8, and A.2.16) should again provide accurate results. By substituting these expressions in the analytical formalism presented in Section 4.2, one can tailor the required $X_s$ to suppress the scattering from the cylinder. After a careful study of these expressions, we chose $a_c = 1.15a$, with $X_s = -39\ \Omega$ for our design. The final optimized parameters are given in Table 4.3. In Fig. 4.15, we plot the grid impedances of the three structures, with the design parameters given in Table 4.3. Although the impedance of the three curves is rather different, they

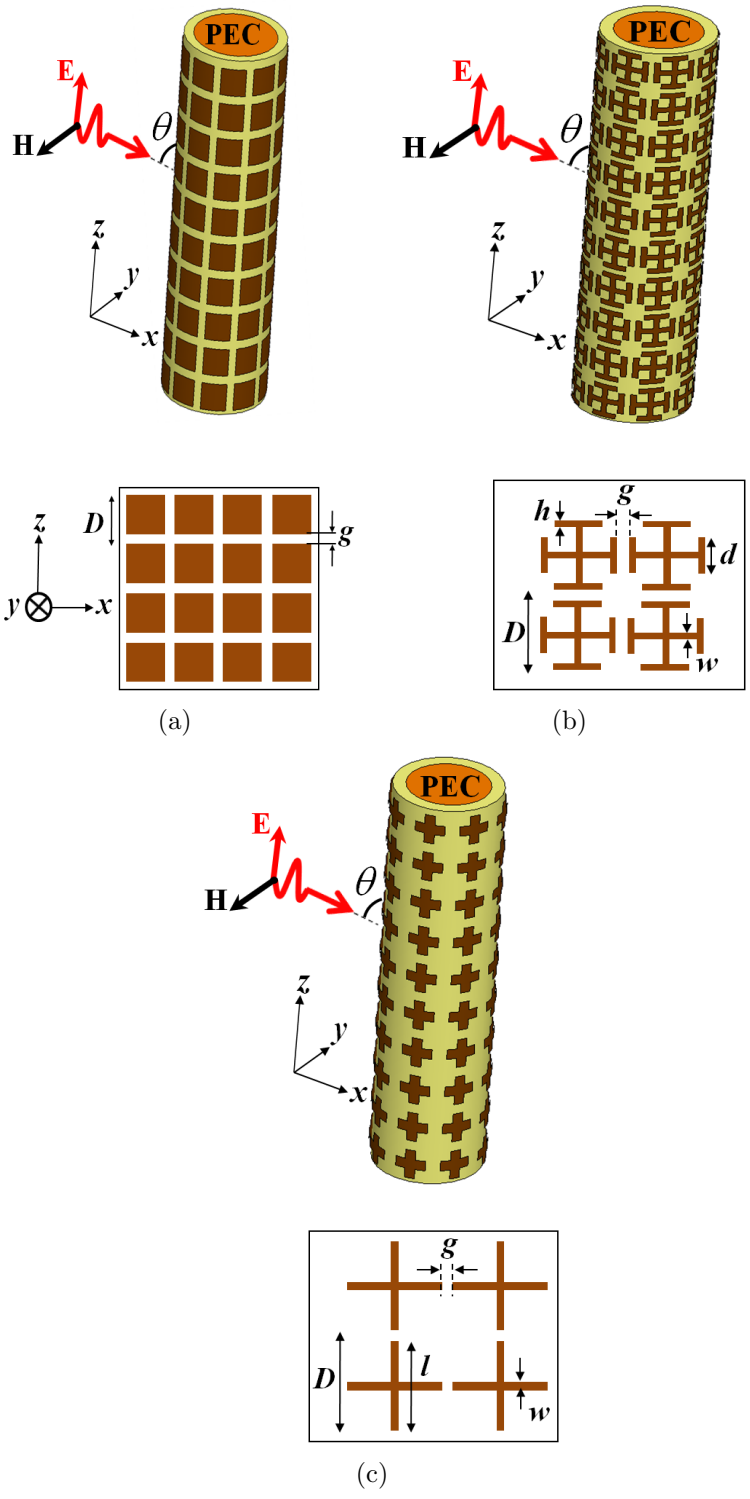


**Figure 4.14.** Schematics of the conducting cylinders covered by FSS mantle cloaks: (a) patch array cylindrical cloak, (b) Jerusalem crosses cylindrical cloak, and (c) cross dipoles cylindrical cloak.

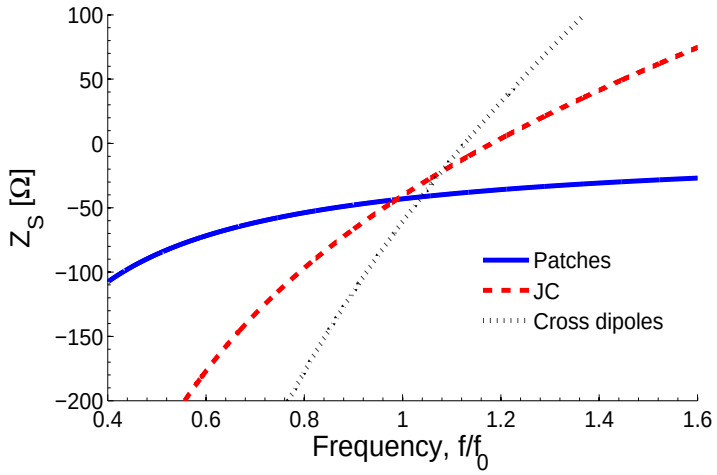


**Figure 4.15.** Variation of grid impedances of the three FSS structures versus frequency obtained using the grid-impedance expressions with parameters given in Table 4.3. The results shown here are calculated using the analytical grid-impedance expressions given in the Appendix.

**Table 4.3.** Parameters of the 2-D sub-wavelength capacitive surface mantle cloaks conformal to a PEC cylinder, with $a = \lambda_0/10$.

| FSS type | $N$ | $D$ | $w$ | $g$ | $d_1$ | $\varepsilon_c$ | $a_c$ |
|---|---|---|---|---|---|---|---|
| Patches | 10 | $\lambda_0/14$ | - | $\lambda_0/222$ | - | 25 | $1.15a$ |
| JC | 6 | $\lambda_0/8$ | $\lambda_0/125$ | $\lambda_0/111$ | $\lambda_0/28$ | 13 | $1.15a$ |
| Cross dipoles | 4 | $\lambda_0/5$ | $\lambda_0/500$ | $\lambda_0/30$ | - | 15 | $1.2a$ |

intersect around the design frequency for $X_s = -39\ \Omega$, as expected. Inspecting Table 4.3, it is seen that the printed cross dipole FSS requires a cloak with larger radius ($a_c = 1.2a$), when compared to the ones used in the other two designs ($a_c = 1.15a$). The reason for chosing a higher value of $a_c$ is to achieve the required $X_s$ at the design frequency. Considering these optimized designs, in Fig. 4.16(a) the variation of SW versus frequency for the three structures is compared with the SW of the uncloaked cylinder with comparable cross-section. Strong scattering cancellations are obtained at the design frequency for all the cloaked cylinders. This clearly emphasizes that the mantle cloak patterned with commonly used 2-D sub-wavelength elements can indeed provide the response of an ideal mantle cloak. Next, we study the behavior of these cloaks for TE-polarized excitation. Fig. 4.16(b) shows the variation of the SW versus

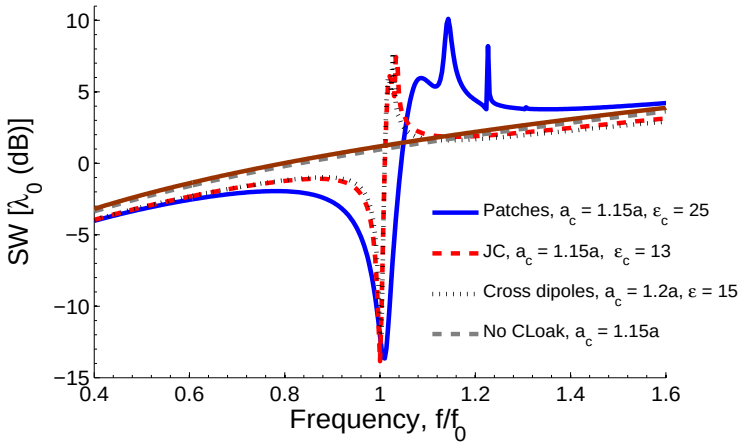


(a)

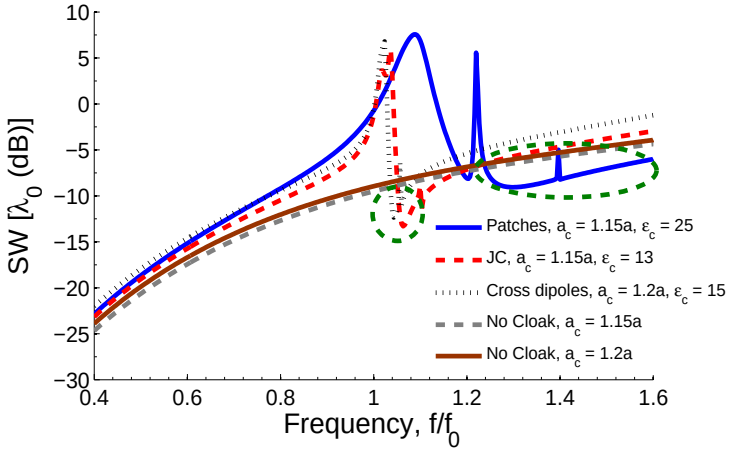


(b)

**Figure 4.16.** Variation of the SW of a conducting cylinder with and without the three FSS mantle cloaks versus frequency: (a) TM polarization and (b) TE polarization. The results shown here are calculated using the analytical model presented in Section.

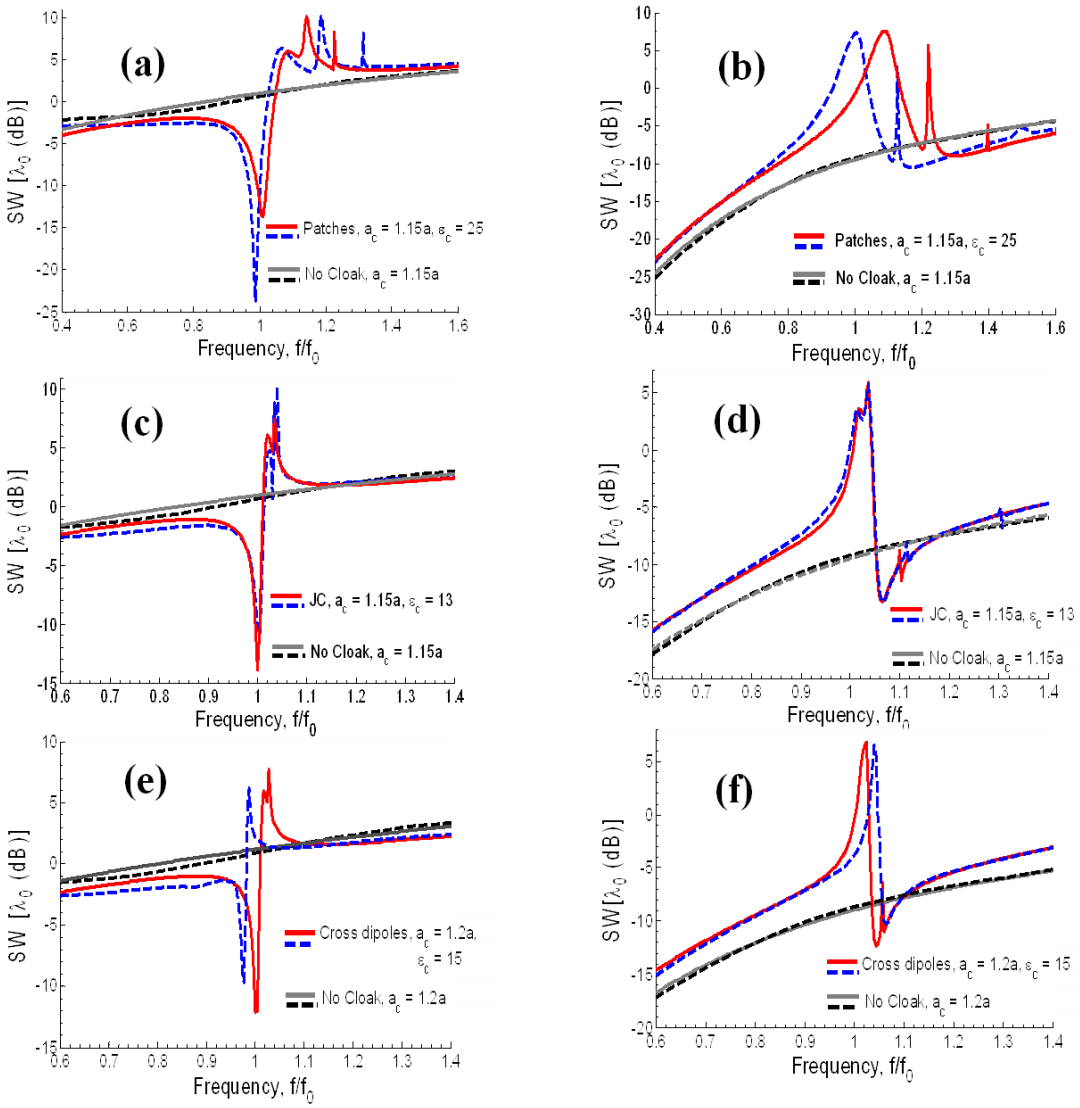


**Figure 4.17.** Comparisons of analytical and full-wave results for the variation of SW of the infinite conducting cylinder with and without the patch array cloak: (a) TM polarization and (b) TE polarization; with and without the Jerusalem crosses cloak: (c) TM polarization and (d) TE polarization; with and without the cross dipoles cloak: (e) TM polarization and (f) TE polarization. In (a)-(f) the analytical results are represented by solid lines and full-wave results by dashed lines.

frequency of the conducting cylinder using the three mantle cloaks considered above, for TE-polarized illumination. As in the previous examples, the scattering reductions arise at frequencies slightly different from the design frequency (shown in green circles in Fig. 4.16(b)). It can be seen that the scattering of the uncloaked conducting cylinder for TE polarization is itself very small (around -10 dB) and by utilizing the cloaks, the scattering is further reduced (i.e., reduced by 3 dB for patch arrays, 5 dB for Jerusalem crosses, and 4 dB for cross dipoles, when compared to the uncloaked cases). To validate our analytical model, we show in Fig. 4.17, the comparison with numerical simulations, which agree very well for both TM and TE polarizations in all the three geometries. This shows that the analytical grid-impedance expressions derived for the planar 2-D sub-wavelength elements can be effectively used to tailor the $X_s$ of the cylindrical mantle cloaks.

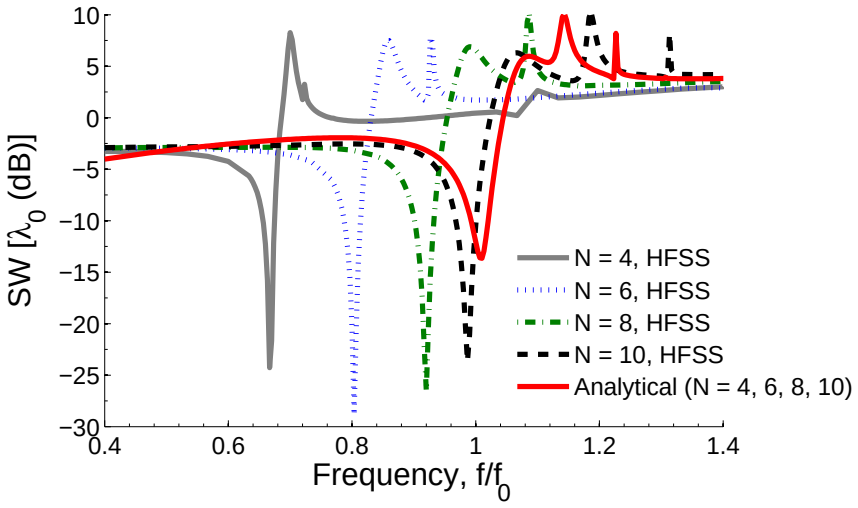


**Figure 4.18.** Comparisons of analytical and full-wave results for the variation of SW versus frequency for different $N$.

As a further verification, we show in Fig. 4.18, the variation of SW versus frequency for various $N$, comparing analytical model and numerical simulations. The parameters of the patch array for different $N$ are given in Table 4.4. Only one curve is shown for the analytical results, shown in red color. As expected, by increasing $N$,

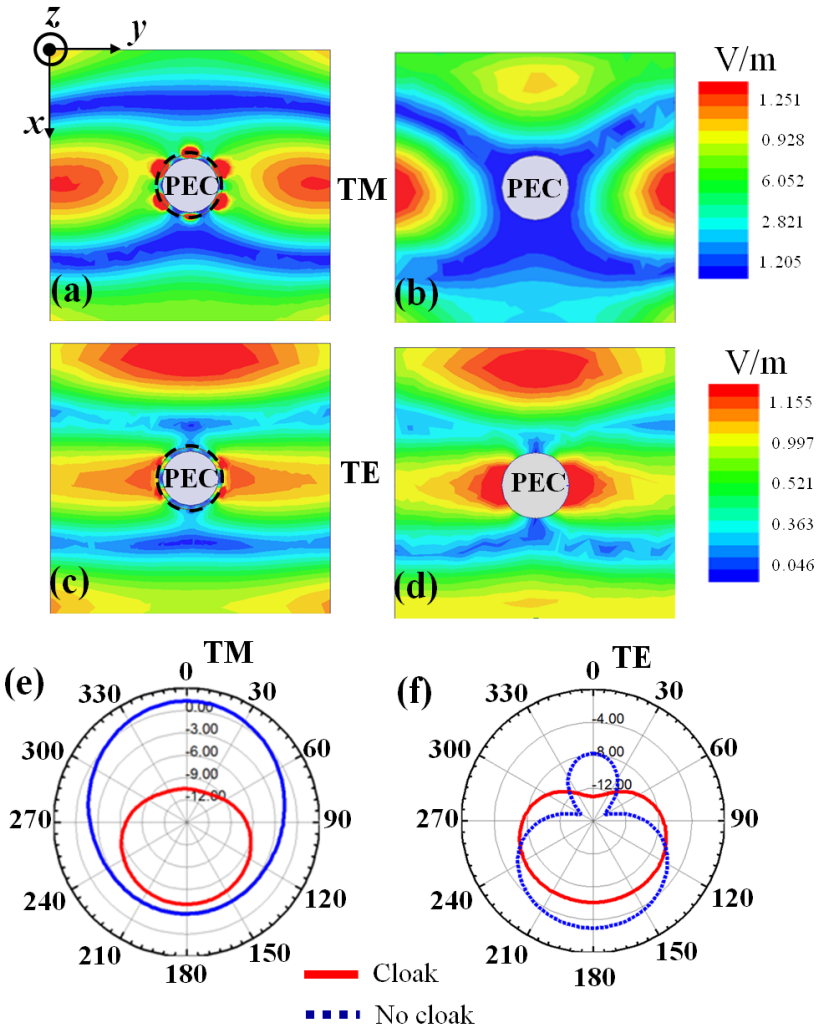


**Figure 4.19.** Full-wave numerical results for the magnitude of **E**-field distribution on the $\phi$-plane for an infinite conducting cylinder for TM polarization: (a) with and (b) without the Jerusalem crosses cloak; TE polarization: (c) with and (d) without the Jerusalem crosses cloak. Far-field radiation patterns for the infinite conducting cylinder with and without the Jerusalem crosses cloak for: (e) TM polarization and (f) TE polarization.

the numerical results converge to the analytical ones.

**Table 4.4.** Parameters of the patch arrays for different number of unit-cells ($N$) around the circumference of the cylinder, with $a = \lambda_0/10$.

| N | $D$ | $w$ | $\varepsilon_c$ | $a_c$ |
|---|---|---|---|---|
| 4 | $\lambda_0/5$ | $\lambda_0/22$ | 25 | $1.15a$ |
| 6 | $\lambda_0/8$ | $\lambda_0/55$ | 25 | $1.15a$ |
| 8 | $\lambda_0/11$ | $\lambda_0/125$ | 25 | $1.15a$ |
| 10 | $\lambda_0/14$ | $\lambda_0/232$ | 25 | $1.15a$ |

Finally, we show in Figs. 4.19 (a)-(d) the full-wave numerical simulations of the amplitude of the **E**-field distributions around the conducting cylinder with and without the Jerusalem crosses cloak (whose dimensions are given in Table 4.3) for both TM and TE polarizations. In all these cases, the plane wave is travelling along the $+x$-direction. For the TM case, it can be noticed that, in the presence of the cloak (Fig. 4.19(a)), the scattering from the cylinder is drastically suppressed, whereas in its absence the field distribution is largely perturbed and scattered fields are observed in all directions (shown in Fig. 4.19(b)). Fig. 4.19(e) shows the far-field radiation patterns of the conducting cylinder with and without the cloak for TM polarizations. It is evident that the scattered power is drastically reduced in all directions, when compared to uncloaked scenario. For TE polarization, in the presence of the cloak, uniform field distributions can be noticed in the near-field regions (shown in Fig. 4.19(c)). For the uncloaked case, the scattered field shown in Fig. 4.19(d) shows only small perturbations around the object. This is expected because, the scattering response for TE polarization is not as dominant as it was for TM polarization (shown in Fig. 4.19(b)). The corresponding far-field radiation patterns shown in Fig. 4.19(f) confirm the previous results. Similar cloaking effects are found using the other FSS geometries studied in this section.

## 4.5 Conclusions

We have presented here an analytical model to design practical mantle cloaks tailored to suppress the scattering from dielectric and conducting cylindrical objects for both polarizations using various sub-wavelength periodic surfaces. It has been shown that the suitable design of a conformal mantle cloak may significantly reduce the scattering from cylindrical rods and analytical formulas to derive the required surface reactance of the conformal surface may be borrowed from established models for planar FSS. Our analytical results, based on the grid-impedance expressions available for planar geometries, have been validated using full-wave numerical simulations.

Although the accuracy of the planar grid-impedance expressions for modeling the cylindrical cloaks varies as a function of the grid parameters, number of inclusions around the cylinder, and frequency of operation, these expressions have been found very accurate even when $N$ is small, up to $N = 4$, for the vertical strips or mesh grid structure, slotted cross dipoles, and cross dipole arrays. Our results may greatly facilitate the implementation and design of mantle cloaks in a variety of applications, including camouflaging and invisibility, cloaked sensing, non-invasive probing, [86] and low-interference communications. The present analysis may be extended to cloaking larger objects, 3-D objects (such as spheres), to oblique illumination, multifrequency operation, and to line-source excitation problems. We are currently working on these problems.

# CHAPTER 5

# MANTLE CLOAKING OF CYLINDRICAL OBJECTS WITH CONFORMAL METASURFACES DUE TO LINE SOURCE

In this chapter, we study a mantle cloaking of cylindrical objects coated with conformal metasurfaces due to an electric line source. The metasurface cloaks are formed by 2-D arrays of slotted (meshes and slot-Jerusalem crosses) and printed (patches and Jerusalem crosses) sub-wavelength frequency selective surface (FSS) elements. The electromagnetic scattering analysis is carried out using the analytical eigenfunction-expansion method which utilizes the two-sided impedance boundary conditions at the interface of the sub-wavelength elements. It is shown that the analytical expressions derived for the planar arrays of sub-wavelength elements may be successfully used to model and tailor the surface reactance of cylindrical conformal mantle cloaks even in a close proximity of the line source to a cloaked object. By proper tailoring of the surface reactance of the cloak, we demonstrate that the field radiated by the line source is almost unperturbed, rendering the object invisible over the range of frequencies of interest (i.e., at microwaves and far-infrared). The

analytical model results presented throughout this chapter are validated using full-wave numerical simulations.

## 5.1 Introduction

In recent years, there has been an increased interest in the analysis and design of various electromagnetic invisibility cloaks due to their broad range of applications in camouflaging, non-invasive probing [82, 86, 87], low-interference communication [86], imaging [77], and cloaked sensing, among others. In particular, the coordinate transformation method or most commonly referred to as the CT method, which was first proposed by Pendry et al [77] and Leonhardt [78], has been used successfully to realize various electromagnetic cloaks with applications ranging from microwave [79, 88–90] to visible light [80, 81]. Later on, various other cloaking methods, such as the plasmonic cloaking [82, 86, 87], [88], [90] anomalous localized resonance [91], and cylindrical transmission-line cloaking [83] have been put forward to design invisibility cloaks. However, the electromagnetic cloaks designed using the above mentioned techniques (such as CT and plasmonic) are bulky and sometimes challenging to realize even with todays fabrication technology. To overcome this issue, recently some of the authors have introduced a different cloaking technique [23–25] based on the concept of mantle cloaking to reduce the visibility of objects of various shapes. This technique is based on the scattering cancellation properties of the mantle cloak (realized using an ultra thin conformal metasurface) characterized by an average surface reactance of choice. By adjusting the parameters of the metasurface inclusions, one can achieve the desired surface reactance, which can effectively cancel the scattering from a given object, thus reducing its overall visibility. However, choosing a specific shape of the metasurface inclusions in order to generate a required surface reactance is a cumbersome process, since it involves a numerical optimization procedure. To overcome this

problem, in chapter IV, we have proposed a simple and accurate analytical model to design various conformal metasurface cloaks, providing a clear analytical recipe for the individual elements forming the metasurfaces. Although, the above mentioned mantle cloaking technique is very robust, the analysis has been limited to the problem of plane-wave scattering, i.e., the object and the cloak lie in the far-field of the source.

In this work, we extend the concept of a mantle cloaking technique to the case of an electric line source placed in a close proximity to the metasurface cloak surrounding a cylindrical object. Using the cloaking conditions obtained in chapter IV, for the plane-wave incidence, i.e., using the same radius of the cloak and the shape and dimensions of the metasurface inclusions, here, we demonstrate that the mantle cloaking technique still holds for an electric line source positioned in a close proximity to the cloaked object. The cloaking effect is shown for both the dielectric and conducting cylinders coated with slotted and printed metasurface mantle cloaks. We consider a variety of 2-D arrays with sub-wavelength FSS elements, such as mesh grids and patches [34, 35, 37–39], and Jerusalem crosses [40, 41]. Based on the analysis carried out in chapter IV, with the assumption that the metasurface inclusions are deeply sub-wavelength, in this chapter we show that the analytical expressions derived for the planar arrays of sub-wavelength elements may be successfully used to model and tailor the surface reactance of cylindrical conformal mantle cloaks even in a close proximity of the line source to a cloaked object. The scattering problem is then solved using the analytical eigenfunction-expansion method which employs the sheet impedance boundary conditions on the surface of the metasurface cloaks. By proper tailoring of the surface reactance of the cloak, we demonstrate that the field radiated by the line source is almost unperturbed, rendering the object invisible at the design frequency, and the analytical results are accurately validated with the full-wave simulations (HFSS [36]). This analytical approach of characterizing the

scattering properties (the cloaking behavior) of cylindrical objects with conformal patterned metasurface cloaks in a close proximity of a line source has not been presented before and is the new contribution of this work. In addition, we demonstrate the cloaking effect due to a line source for electrically large objects. Also, at higher frequencies, it is shown that the metasurface coated metallic cylinder can be used to enhance the radiation of the line source and to increase the directivity in the forward direction when compared to the no cover case (bare metallic cylinder), with potential applications for low-profile conformal antennas.

The chapter is organized as follows. In 5.2, the formalism of the analytical model for the analysis of 2-D dielectric and metallic cylindrical objects coated by metasurfaces (metameshes and metafilms) due to an electric line source is presented. In 5.3, we demonstrate the mantle cloaking effect for various cloaked cylindrical objects. In 5.4, we present a parametric study of the cloaking effect for various positions of the line source away from the object, and discuss the applicability of the analytical grid expressions for the cylindrical conformal printed and slotted (metameshes and metafilms). In 5.5, we demonstrate the use of a particular patterned metasurface cloak (composed of printed patches) coating metallic cylinder for low-profile conformal antenna applications with improved directivity. Further, in 5.6, we show the effectiveness of the mantle cloaking technique for electrically large dielectric objects in the presence of a line source. Finally, the conclusions are drawn in 5.7. The time dependence of the form $e^{j\omega t}$ is assumed and suppressed.

## 5.2 Theoretical Analysis

Consider the geometry illustrated in Fig. 5.1(a), where an infinite electric line source of constant current $I_e$ is positioned in the vicinity of an infinitely long dielectric

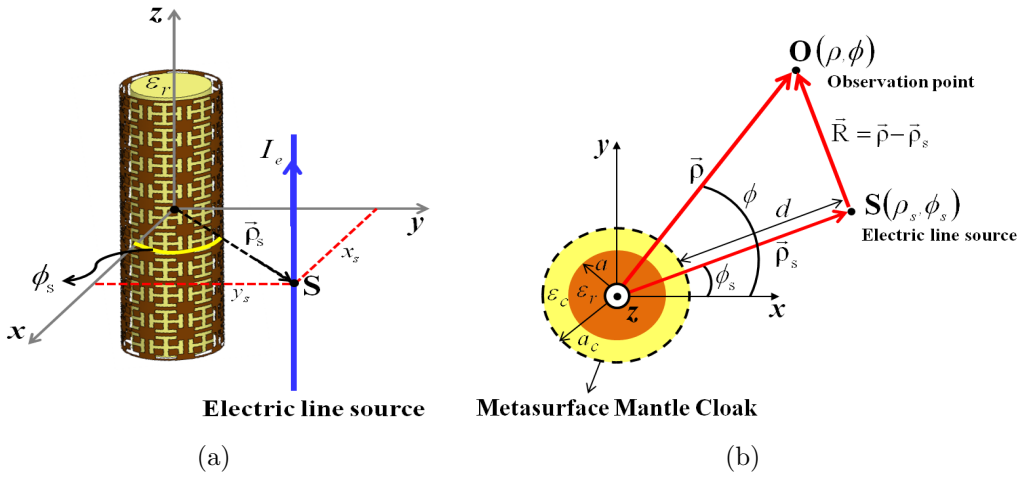


**Figure 5.1.** Schematic of a dielectric cylinder coated by a conformal array of slotted Jerusalem crosses, illuminated by an electric line source carrying a current $I_e$: (a) 3-D view, and (b) top view. In Fig. 1(b) **S** is the source position and **O** is the observation point.

cylinder with relative permittivity $\varepsilon_r$, radius $a$, covered by a mantle cloak with radius $a_c$, with the space between the cloak and the cylinder filled by a dielectric of thickness $a_c - a$, and relative permittivity $\varepsilon_c$. The source and observation locations, along with the positions of the object and that of the cloak are shown in Fig. 5.1(b) in cylindrical $(\rho, \phi, z)$ and Cartesian $(x, y, z)$ coordinate systems, where the axis of the cylinder and that of the line source coincides with the $z$-axis. The coordinates of the line source are $(\rho_s, \phi_s)$, while the coordinates of the observation point are $(\rho, \phi)$. The distance between the electric line source and the surface of the cylinder is denoted by $d$. The relationship between the variables in cartesian coordinate system and those of the cylindrical system is given as $\rho_s = \sqrt{(x_s)^2 + (y_s)^2}$, $\rho = \sqrt{x^2 + y^2}$, and $R = |\overrightarrow{\rho} - \overrightarrow{\rho_s}| = \sqrt{\rho^2 + (\rho_s)^2 - 2\rho\rho_s \cos(\phi - \phi_s)}$.

For a line source positioned away from the origin

$$\overrightarrow{J} = \hat{z}\frac{I_e}{\rho}\delta(\overrightarrow{\rho} - \overrightarrow{\rho_s}) = \hat{z}\frac{I_e}{\rho}\delta(\rho - \rho_s)\delta(\phi - \phi_s), \tag{5.2.1}$$

the incident field is given by

$$E_z^i(\rho,\phi) = -\frac{{k_0}^2}{4\omega\varepsilon_0} H_0^{(2)}(k_0|\overrightarrow{\rho} - \overrightarrow{\rho_s}|), \tag{5.2.2}$$

where $H_0^{(2)}(k_0|\overrightarrow{\rho} - \overrightarrow{\rho_s}|)$ is the Hankel function of the second kind. Employing the addition theorem for Hankel functions Eq. 5.2.2 can be written as [92],

$$E_z^i(\rho,\phi) = -\frac{k_0^2 I_e}{4\omega\varepsilon_0} \begin{cases} \sum_{n=-\infty}^{\infty} J_n(k_0\rho) H_n^{(2)}(k_0\rho_s) e^{jn\phi-\phi_s} & \rho \leq \rho_s \\ \sum_{n=-\infty}^{\infty} J_n(k_0\rho_s) H_n^{(2)}(k_0\rho) e^{jn\phi-\phi_s} & \rho > \rho_s \end{cases} \tag{5.2.3}$$

and the scattered fields in each of the regions can be expressed as

$$E_z^s(\rho,\phi) = -\frac{k_0^2 I_e}{4\omega\varepsilon_0} \begin{cases} \sum_{n=-\infty}^{\infty} c_n H_n^{(2)}(k_0\rho) e^{jn\phi} & \rho \geq a_c \\ \sum_{n=-\infty}^{\infty} \left[a_n J_n(k_c\rho) + b_n Y_n(k_c\rho)\right] e^{jn\phi} & a \leqslant \rho \leqslant a_c \\ \sum_{n=-\infty}^{\infty} d_n J_n(k\rho) e^{jn\phi} & \rho \leqslant a \end{cases} \tag{5.2.4}$$

where $k_0 = \omega\sqrt{\mu_0\varepsilon_0}$, $k_c = k_0\sqrt{\varepsilon}_c$, and $k = k_0\sqrt{\varepsilon}_r$ are the wave numbers in free-space, concentric dielectric region, and core regions, respectively. $J_n(\cdot)$ and $Y_n(\cdot)$, are the Bessel functions of the first and second kind. The unknown coefficients ${a_n}^{TM}$, ${b_n}^{TM}$, ${c_n}^{TM}$, and ${d_n}^{TM}$ are obtained by enforcing the following boundary conditions: (i) continuity of tangential components of electric and magnetic fields at the boundary of the core ($\rho = a$) and (ii) two-sided impedance boundary condition at the interface of the mantle cloak ($\rho = a_c$). The two-sided impedance boundary condition establishes that the tangential electric and magnetic fields can be related via the sheet impedance, i.e.,

$$E_z^i + E_z^s|_{\rho=a_c^+} = E_z^s|_{\rho=a_c^-} = Z_s\left[\left(H_\phi^i + H_\phi^s\right)|_{\rho=a_c^+} - H_\phi^s|_{\rho=a_c^-}\right], \tag{5.2.5}$$

where $Z_s$ is the surface impedance of the mantle cloak covering the cylinder. $H_\phi^i$ and $H_\phi^i$ are the corresponding magnetic field components which can be obtained using Maxwell's Faraday equation. The mantle cloak in this work is realized using

various commonly used patterned metasurfaces or FSS elements [with a typical geometry shown in Fig. 5.1(a)]. With the assumption that the inclusions are deeply sub-wavelength, the metasurface cloak can be characterized by a surface with average surface impedance, such that $Z_s$ can be written in terms of effective circuit parameters [34,35] as $R_s + jX_s$, where $R_s$ represents surface losses and $X_s$ takes into account the stored energy, and it can be either inductive ($X_s > 0$) or capacitive ($X_s < 0$) reactance of the FSS structure. In the lossless case, we have $Z_s = jX_s$, i.e., $R_s = 0$. In the limiting cases of $X_s \to \infty$, we have a dielectric cylinder with no cloak, as the metasurface does not interact with the impinging field of the electric line source (no induced surface currents). Since, closed-form analytical expressions representing the surface impedance of the cylindrical FSS arrays are not available in the literature, one can use the expressions available for the planar sub-wavelength FSS elements, provided the conditions on the size of the inclusions of the metasurface cloak are satisfied. This hypothesis has been clearly proved in chapter IV, where plane-wave scattering from various cylindrical cloaks was considered. Details of the analytical expressions for various planar periodic sub-wavelength elements (meshes, patches, Jerusalem crosses, and slotted Jerusalem crosses), which are used in the design of mantle cloaks in the following, are provided in Appendix. However, in the present work, the patterned metasurface cloak is in the intense near field of the line source, and one might wonder about the applicability of these expressions. Under certain conditions in regard to the location of the line source such that the evanescent fields scattered by the grids are negligible at the observation planes, we show in the following that these formulas which are originally derived for the planar sub-wavelength FSS arrays for plane-wave incidence can still accurately capture the physics of the field scattered by a cylindrical FSS excited by an electric line source. Once the surface impedance is known, the unknown scattering coefficients can be solved by enforcing

the boundary conditions discussed above, and subsequently the total fields can be determined in each of the regions. With proper tailoring of the surface reactance of the cylindrical cloak, the currents induced on the surface of the cloak generates anti-phase fields which cancels the scattering from the object, and the field radiated by a line source located a fraction of wavelength away from the cloak remains unperturbed, rendering the object invisible at the design frequency.

## 5.3 Numerical Results

Based on the analysis carried out in chapter IV, for the 2-D cylindrical objects (such as dielectric and perfect electric conductor (PEC) cylinders) covered by various sub-wavelength FSS mantle cloaks for plane-wave incidence, here we demonstrate the mantle cloaking effect for an electric line source positioned in the vicinity, using the analytical model described in Section 5.2. The required surface reactances of the conformal FSS elements are achieved using the analytical grid-impedance expressions given in Appendix for the planar cases. Although, these expressions have been derived for the planar case and have been successfully applied for cylindrical FSS cloaks (chapter IV) with source situated at infinity, here we use them in the case when the line source is in close proximity to the patterned metasurface cloak. Further, our analytical model results are validated using the full-wave numerical simulations.

### 5.3.1 Dielectric cylinder

For all the configurations studied in this chapter, the position of the line source is such that it is varied only along the x-axis (no azimuthal variations, $\phi_s = 0$), i.e., with $y_s = 0$ we have $\rho_s = x_s$. Further, this location of the line source in the rest of the work is indicated by the distance $d$ (which is the distance between the surface

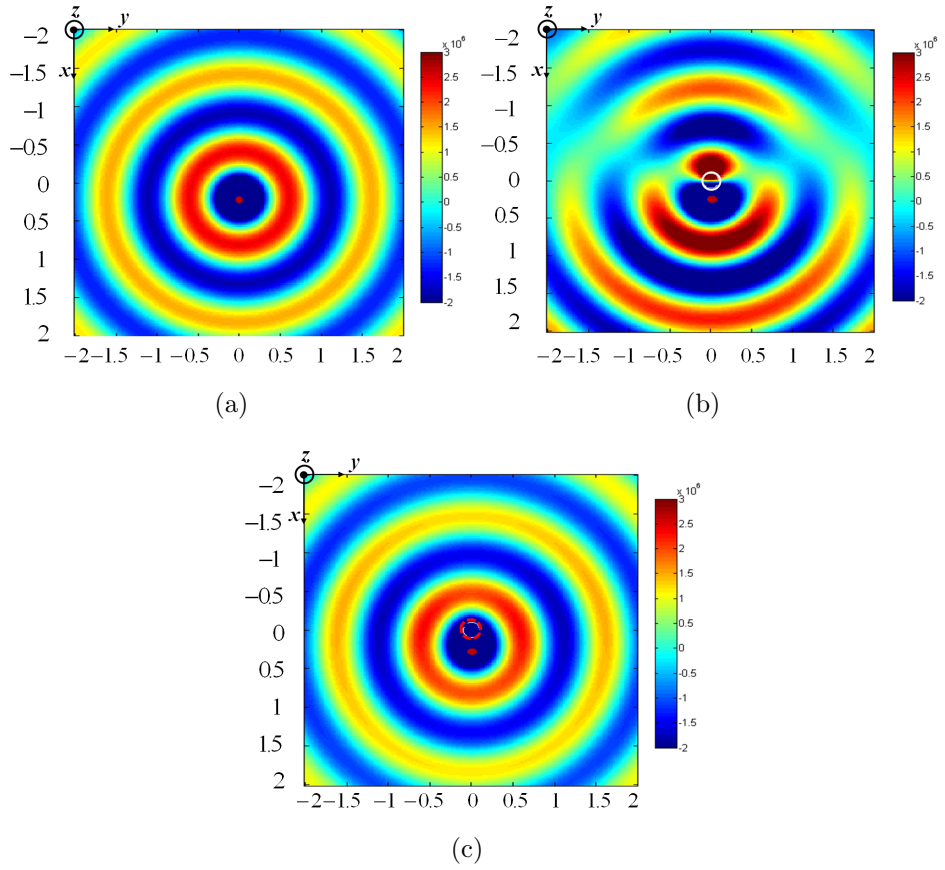


**Figure 5.2.** Analytical results of magnitude of E-field distributions on the $\phi$-plane: (a) in vacuum, (b) without the cloak, and (c) with the mesh grid cloak.

of the cloak and the line source, shown in Fig. 5.2). We first consider an infinite length electric line source located at the point $S(\rho_s, \phi_s) = (0.2\lambda_0, 0)$ with $d = 0.1\lambda_0$ radiating in a vacuum with wavelength $\lambda_0$ and carrying a current $I_e = 1\ A$. The real part of electric field distribution $Re(E_z)$ calculated using the analytical model given

in Section 5.2, is shown in Fig. 5.2(a). Here, $E_z$ is defined as

$$E_z(\rho,\phi) = -\frac{k_0^2 I_e}{4\omega\varepsilon_0}\begin{cases} \sum_{n=-\infty}^{\infty} J_n\left(k_0\rho\right) H_n^{(2)}\left(k_0\rho_s\right) e^{jn\phi-\phi_s} + \sum_{n=-\infty}^{\infty} c_n H_n^{(2)}\left(k_0\rho\right) e^{jn\phi} & \rho \leq \rho_s \\ \sum_{n=-\infty}^{\infty} J_n\left(k_0\rho_s\right) H_n^{(2)}\left(k_0\rho\right) e^{jn\phi-\phi_s} + \sum_{n=-\infty}^{\infty} c_n H_n^{(2)}\left(k_0\rho e^{jn\phi}\right) & \rho > \rho_s \\ \sum_{n=-\infty}^{\infty} \left[a_n J_n\left(k_c\rho\right) + b_n Y_n\left(k_c\rho\right)\right] e^{jn\phi} & a \leqslant \rho \leqslant a_c \\ \sum_{n=-\infty}^{\infty} d_n J_n\left(k\rho\right) e^{jn\phi} & \rho \leqslant a \end{cases} \tag{5.3.6}$$

For simplicity, the computational domain can be as that shown in Fig. 5.3. Next, we

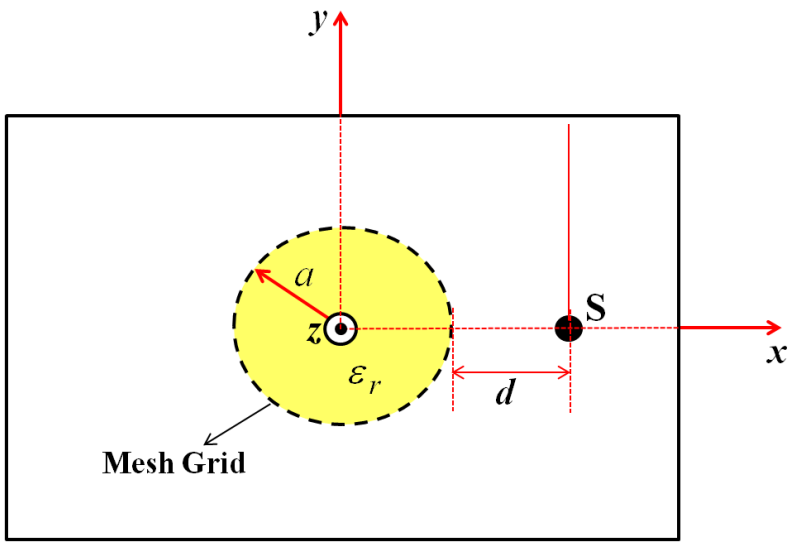


**Figure 5.3.** A sketch of the computational domain used in the analytical model for calculation of electric fields.

consider a 2-D infinitely long dielectric cylinder with $\varepsilon_r = 10$ and radius $a = \lambda_0/10$ placed at the origin in the vicinity of the line source. Obviously, the dielectric cylinder scatters the incident field in different directions and perturbs the field distribution of the line source, as shown in Fig. 5.2(b). To design a mantle cloak for this cylinder, we follow the analysis carried out in Section 4.3.1 for a similar case, with a plane-wave at normal incidence, where it was shown that a 2-D inductive mesh grid metasurface

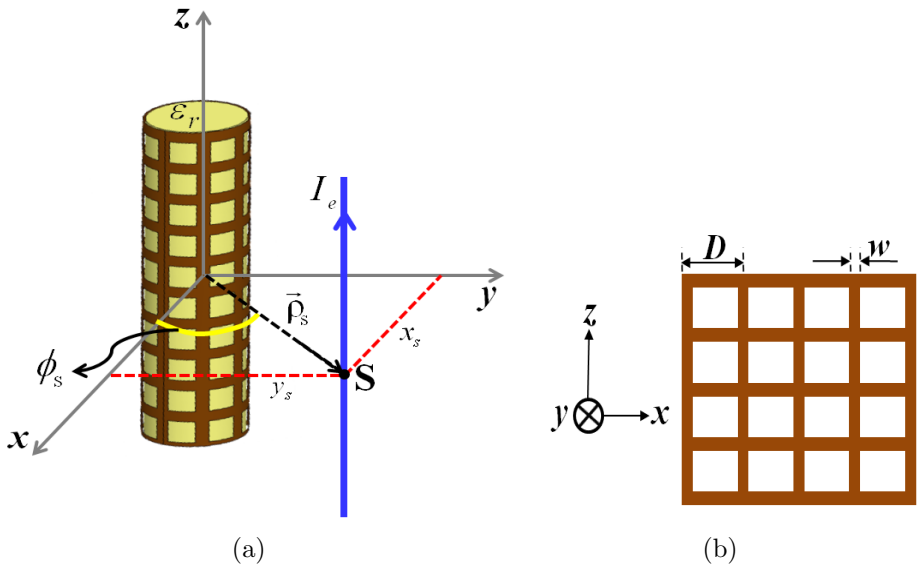


**Figure 5.4.** Geometry of the dielectric cylinder covered by the mesh grid mantle cloak: (a) 3-D view, and (b) periodic grid of the planar structure.

cloak drastically suppresses the scattering from the dielectric cylinder. The geometry of the dielectric cylinder covered by a conformal mesh grid is shown in Fig. 5.4. Using a mesh grid cloak similar to the one used in Section 4.3.1 (where the parameters of the cloak are optimized using the grid-impedance expression given in Appendix), here we investigate the scattering properties of the mesh grid covered dielectric cylinder in the presence of a line source. The parameters used in the design are: $D = \lambda_0/16$, $w = \lambda_0/200$, $\varepsilon_r = 10$, and $a_c = a$. The electric field distribution $Re(E_z)$ calculated using the analytical model, is shown in Fig. 5.2(c). Clearly, one can notice that in the presence of the cloak, the scattering from the cylinder is drastically suppressed, and the perturbed field of the line source in the presence of the bare dielectric cylinder (no cloak case, shown in Fig. 5.2(b)) is clearly restored. With the field penetrating through the cloak and the object, it can be noticed that the field behavior resembles to the case shown in Fig. 5.2(a) as if the electric line source is radiating in vacuum, thus rendering the object invisible. To validate these results, in Fig. 5.5 we show

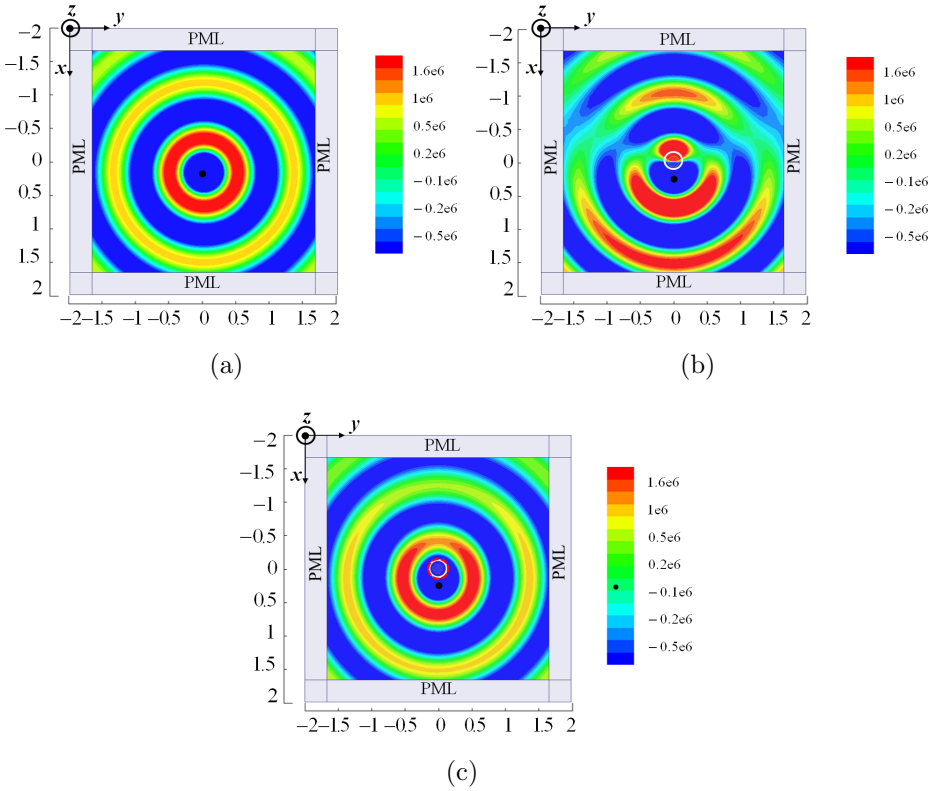


**Figure 5.5.** Full-wave numerical results of magnitude of E-field distributions on the $\phi$-plane: (a) in vacuum, (b) without the cloak, and (c) with the mesh grid cloak.

the corresponding field distributions of the three cases considered in Fig. 5.2, but calculated using the full-wave numerical simulations. For the full-wave simulations, a computational domain similar to the analytical model was set up, but the boundaries are terminated by the perfectly matched layers (PMLs), and one can clearly notice the mantle cloaking effect, which corroborates the above analytical results. This proves the concept of mantle cloaking for objects which lie in the very close neighborhood of the line source. To further comprehend the effect of cloaking, in Fig. 5.6 we plot the real part of the transverse component of the electric field at origin varying along the $y$-axis. The field values are obtained using the analytical model and three cases similar to those in Figs. 5.2 and 5.5 are considered here: vacuum, dielectric cylinder with no cloak, and dielectric cylinder with cloak. By using the line integral, the fields are

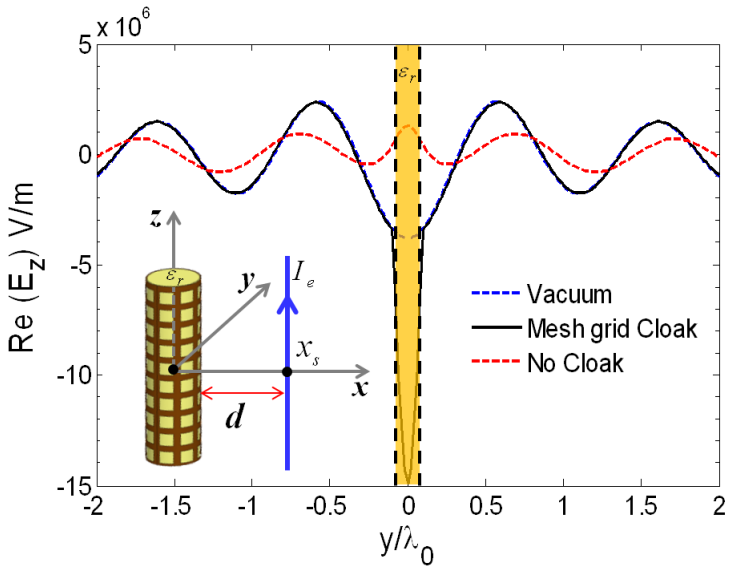


**Figure 5.6.** Real part of $E_z$ along the $y$-axis calculated using the analytical model. The vertical dashed bold lines represent the position of the mesh grid cloak, and the shaded region represents the dielectric cylinder.

calculated along a line going through the center of the dielectric cylinder ($x = 0, y$), where $y$ varies from $-2$ to 2. It should be noted that the dimensions of the domain here and in the rest of the chapter are normalized to free-space wavelength $\lambda_0$. To have a clear picture see Fig. 5.7, where the computational domain along with the location of source and the line where fields are calculated, are shown. It can be observed that the field values (shown in Fig. 5.6) in vacuum and for the cylinder with cloak have the same amplitude outside the region of the cloak, indicating that the cloak suppresses the scattered fields and renders the object almost undetectable. Obviously, the cylinder with no cloak scatters the field in different directions and hence the reason for low amplitude of the field value, as shown in Fig. 5.6 using dashed red curve. The accuracy of the analytical model is further demonstrated using the full-wave results, as shown in Fig. 5.8, where the comparisons are plotted separately for each of the three cases (vacuum, dielectric with no cloak, and dielectric with cloak). Cleary, it can be noticed that the analytical model captures the physics of the problem, and verifies the accuracy of the analytical grid-impedance expression used in describing

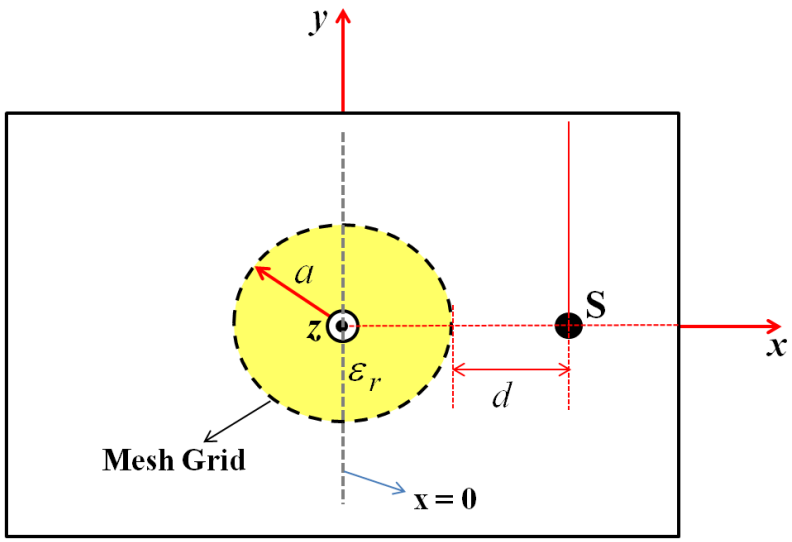


**Figure 5.7.** Sketch of the computational domain used in the analytical model for calculation of electric field along the $y$-axis.

the surface reactance reactance of the conformal FSS, even for an electric line source present in close proximity to the cloak. Further, since the analytical model does not provide an exact solution, small discrepancies can be noticed around the region of the cloak and inside the object. This is because, close to the grids the evanescent fields scattered are significant, and since the numerical solver calculates the true field and the analytical model gives an average value, the differences noticed are reasonable.

In the next example, we consider a dielectric cylinder with same parameters similar to the one considered previously (i.e., in particular the parameters of the cylinder and the position of the line source), but covered by a different mantle cloak. Since, the cloak should have an inductive response to reduce the scattering, here we choose the slotted Jerusalem cross FSS array, whose geometry is shown in Fig. 5.9. Following the same approach as in Section 4.3.1, here we achieve the required surface impedance of the cloak by optimizing the parameters of the FSS unit-cell using the analytical grid-impedance expression given in the Appendix, for the planar surface. The parameters of the optimized slotted Jerusalem cross FSS array cloak are: $D = \lambda_0/15$, $w = \lambda_0/200$, $g = \lambda_0/650$, $d_1 = \lambda_0/22$,and $a_c = 1.05a$. It can be observed that, the radius

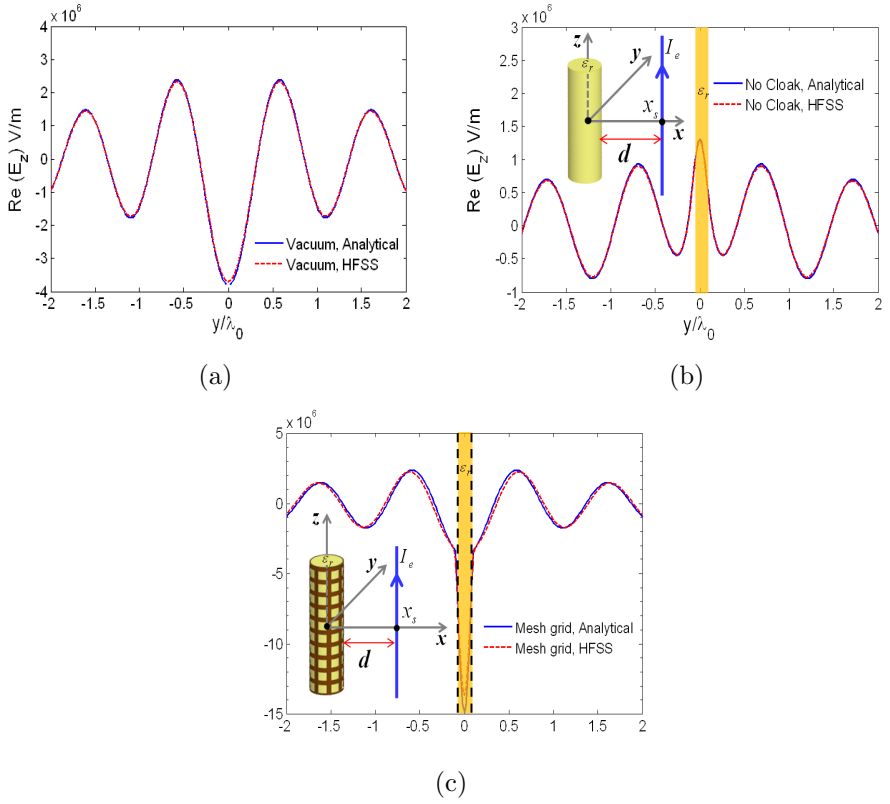


**Figure 5.8.** Verification of analytical results shown in Fig. 6.5, using full-wave numerical simulations: (a) in vacuum, (b) without the cloak, and (c) with the mesh grid cloak. The vertical dashed bold lines represent the position of the mesh grid cloak, and the shaded region represents the dielectric cylinder.

of the cloak in this case is slightly bigger than in the previous case for mesh grid. The reason for choosing a higher value of $a_c$ is to achieve the required $X_s$ at the design frequency. It is also worth mentioning that these parameters are originally optimized to yield a null in the scattering width for a plane-wave incidence. Using the same parameters of the cloak, in the following, we use them to achieve cloaking for a line source located in the close proximity to the object. Figure 5.10 shows the total electric field distributions for three cases (vacuum, dielectric with no cloak, and dielectric with cloak) similar to those shown in Fig. 5.6. Clearly, in the region outside the cloak, one can notice that the amplitudes of the fields in vacuum and in the presence of the cloak are high and almost identical when compared to the

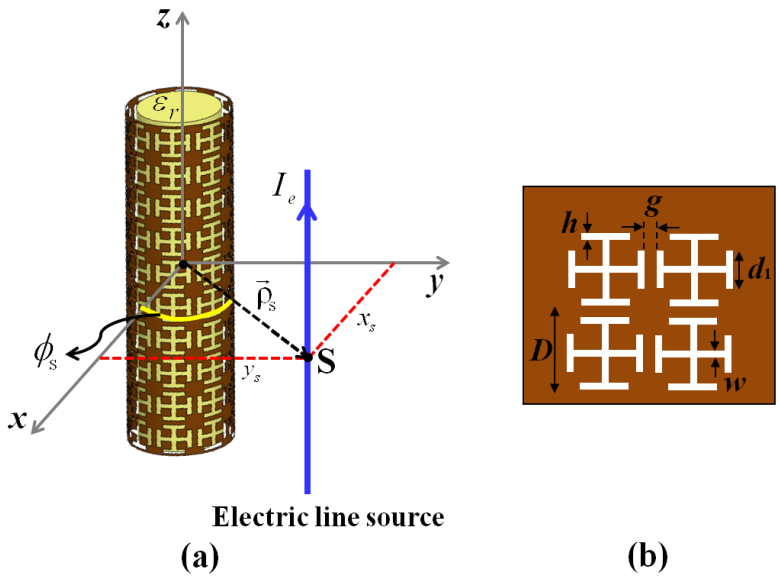


**Figure 5.9.** Geometry of the dielectric cylinder covered by slotted Jerusalem crosses mantle cloak: (a) 3-D view, and (b) periodic grid of the planar structure.

uncloaked cylinder of comparable cross-section. Also, it should be noted that the medium between the dielectric cylinder and the slotted Jerusalem cross cloak is free space. Further in Fig. 5.24, we illustrate the effectiveness of the analytical model, by comparing the electric field distributions calculated using the analytical model (results shown in Fig. 5.10) with the full-wave results. Again, our analytical model results are accurately verified, with the advantage of requiring negligible computation resources. Similar behavior as that shown in Figs. 5.2 and 5.5 can also be obtained using the slotted Jerusalem crosses cloak, however, the results are not included here for the sake of brevity.

### 5.3.2 Conducting Cylinder

Similar to the study carried out in Section 5.3.1, i.e., cloaking of dielectric cylinder using 2-D sub-wavelength periodic elements, in this section we focus on extending the analysis to a conducting cylinder. In this case, a capacitive surface reactance is required to suppress the scattering from the cylinder. To realize this reactance,

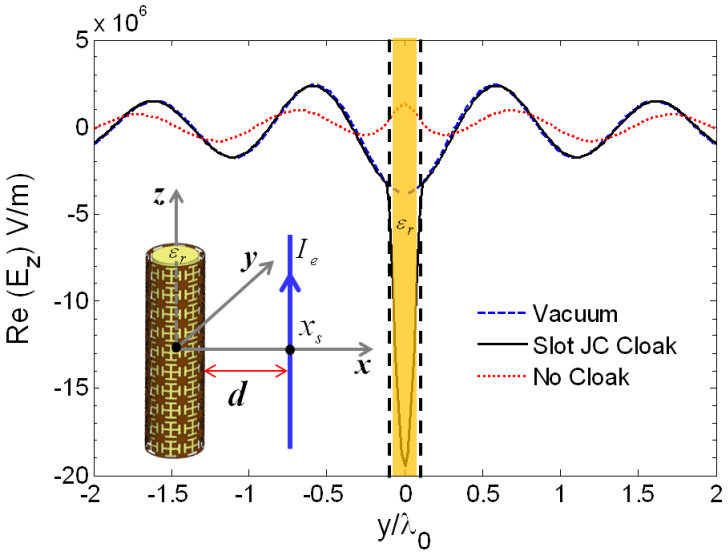


**Figure 5.10.** Real part of $E_z$ along the $y$-axis calculated using the analytical model. The vertical dashed bold lines represent the position of the slotted Jerusalem crosses cloak, and the shaded region represents the dielectric cylinder, with the medium between the cloak and the object being free-space.

here we use the complementary cases of the 2-D sub-wavelength elements studied in Section 5.3.1, i.e., 2-D arrays of printed patches and Jerusalem crosses (whose geometries are shown in Fig. 5.12). As stated before, the analysis here will be carried out for an electric line source located in close neighborhood of the object. In this case the field cannot penetrate the object and, unlike the dielectric scenario where the cloak can be conformed to the object, here, due to the zero impedance of the conducting cylinder, there must be a gap between the cloak and the object to avoid an electric short. Based on the analysis carried out in chapter IV, here, we demonstrate the effectiveness of the mantle cloaking technique for similar conducting cylinders covered by similar patch array and Jerusalem cross array cloaks due to an electric line source. Using the exact design parameters for the patch array cloak and the object, and employing the same closed-form analytical grid-impedance expression (given in the Appendix) for the surface reactance of the cloak in the analytical model given in Section 5.2, in Fig. 5.13, we plot the total electric field distributions ($Re(E_z)$) in the entire computational domain (see Fig. 5.3 for the domain region). The parameters of

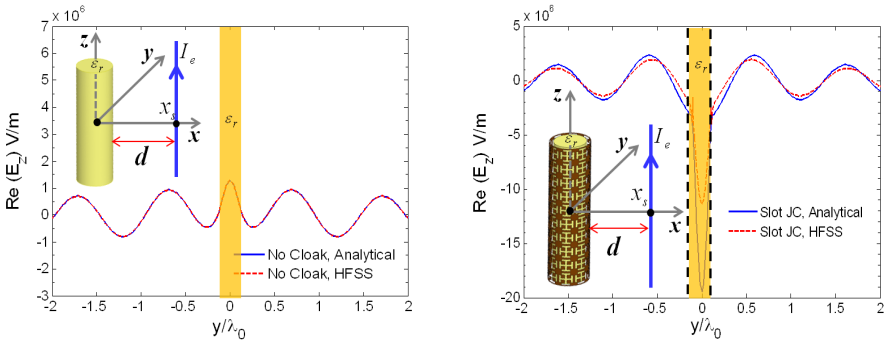


(a) (b)

**Figure 5.11.** Verification of analytical results shown in Fig. 6.8, using full-wave numerical simulations: (a) without the cloak and (b) with the slotted Jerusalem crosses cloak. The vertical dashed bold lines represent the position of the cloak, and the shaded region represents the dielectric cylinder.

the patch array cloak along with the Jerusalem crosses cloak are given in Table 5.1. To show the effect of cloaking, we show the field distribution in the absence of the cloak. In the presence of the patch array cloak (Fig. 5.13(a)), it can be observed that the scattering is greatly suppressed and near-perfect cylindrical wave-fronts of the line source are restored, rendering the object impossible to detect. To corroborate our analytical model results, in Fig. 5.14, we show the numerical results. Clearly, these results demonstrate the performance of the mantle cloaking and verify the analytical

**Table 5.1.** Parameters of the 2-D sub-wavelength FSS mantle cloaks conformal to a PEC cylinder, with $a = \lambda_0/10$.

| FSS type | N | $D$ | $w$ | $g$ | $d_1$ | $\varepsilon_c$ | $a_c = a$ | $d$ |
|---|---|---|---|---|---|---|---|---|
| Patches | 10 | $\lambda_0/14$ | - | $\lambda_0/222$ | - | 25 | $1.15a$ | $0.1\lambda_0$ |
| JC | 6 | $\lambda_0/8$ | $\lambda_0/125$ | $\lambda_0/111$ | $\lambda_0/28$ | 13 | $1.15a$ | $0.1\lambda_0$ |

results. Similar behavior as that shown in Figs. 5.13(a) and 5.14(a) can also be obtained using the Jerusalem crosses cloak, however, the results are not included here for the sake of brevity.

To further show the effect of cloaking using the patch array and Jerusalem cross array cloaks, in Figs. 5.15 and 5.16, we plot the total electric field distributions for

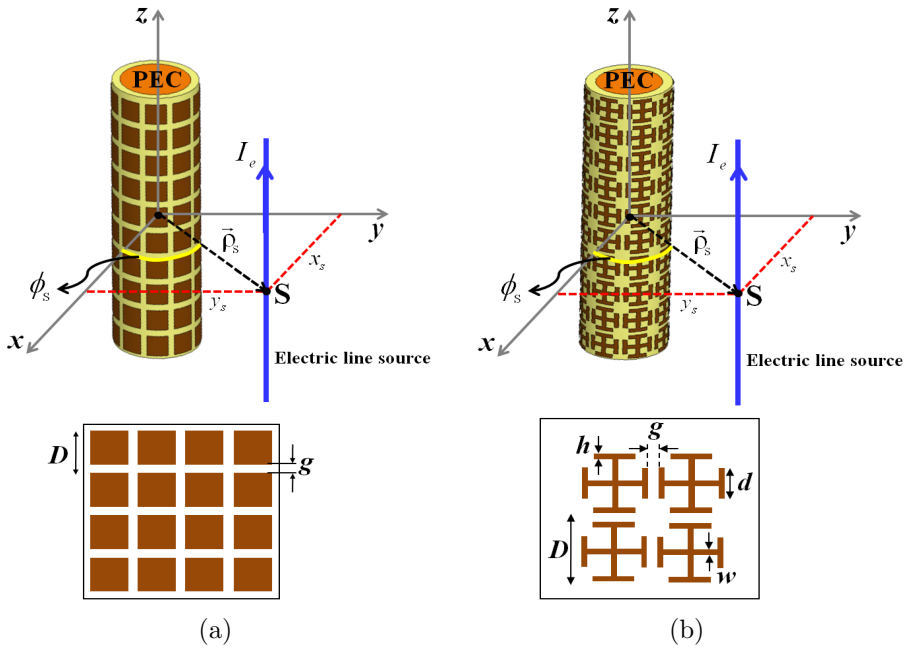


**Figure 5.12.** Schematics of the conducting cylinders covered by FSS mantle cloaks: (a) patch array cylindrical cloak, and (b) Jerusalem crosses cylindrical cloak.

three cases (vacuum, PEC cylinder with no cloak, and PEC cylinder with cloak), calculated using the analytical model, similar to that in Fig. 5.10. The field values in the two cases: cylinder with cloaks and vacuum, are almost identical, particularly, outside the region of cloaks. As expected, the field values in the absence of cloaks scatter irregularly and diminish (have low amplitudes), rendering the objects easily detectable in both the cases. Further, the numerical results shown in Fig. 5.14 give only a qualitative agreement with the analytical results (shown in Fig. 5.13), and they do not provide an exact quantitative accuracy of the analytical model. To show this, in Figs. 5.17 and 5.18 we show comparisons of our analytical model results with the numerical simulation results, similar to those shown in Figs. 5.8 and 5.24. The analytical results agree very well with the full-wave results. This shows that the analytical grid-impedance expressions derived for the planar 2-D sub-wavelength elements can be effectively used to tailor the $X_s$ of the cylindrical mantle cloaks even

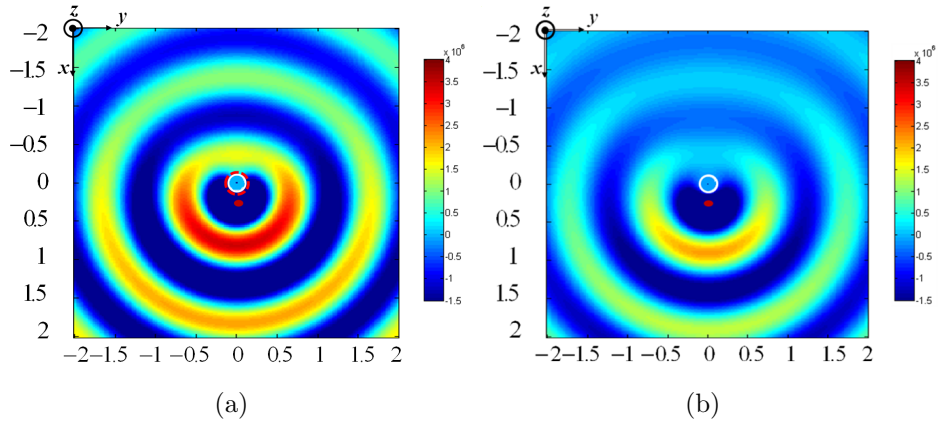


**Figure 5.13.** Analytical results of magnitude of E-field distributions on the $\phi$-plane: (a) with the patch array cloak, and (b) without the cloak.

when the cylindrical cloak lie in the intense near field of the line source.

## 5.4 Verification

In the previous section, the mantle cloaking effect has been verified for various cylindrical objects using a variety of 2-D sub-wavelength printed and slotted FSS arrays. However, it is necessary to verify the cloaking effect for various positions of the line source, particularly, when the line source is very close to the object. To complete the study in this section we demonstrate the effect of cloaking for various positions of the line source.

Here we consider a dielectric cylinder covered by a mesh grid cloak, which was studied in Section 5.3.1. With the same parameters of the cloak and the object (see parameters in Section 5.3.1), in Fig. 5.19 we show the total electric field distributions for various positions $d = 0.015\lambda_0$, $0.1\lambda_0$, and $0.4\lambda_0$ of the line source in the presence of the cloaked dielectric cylinder. The results here are calculated using the analytical model. To show the effect of cloaking, we also included the results for the the corresponding cases (different positions of the line source) when there is no cloak.

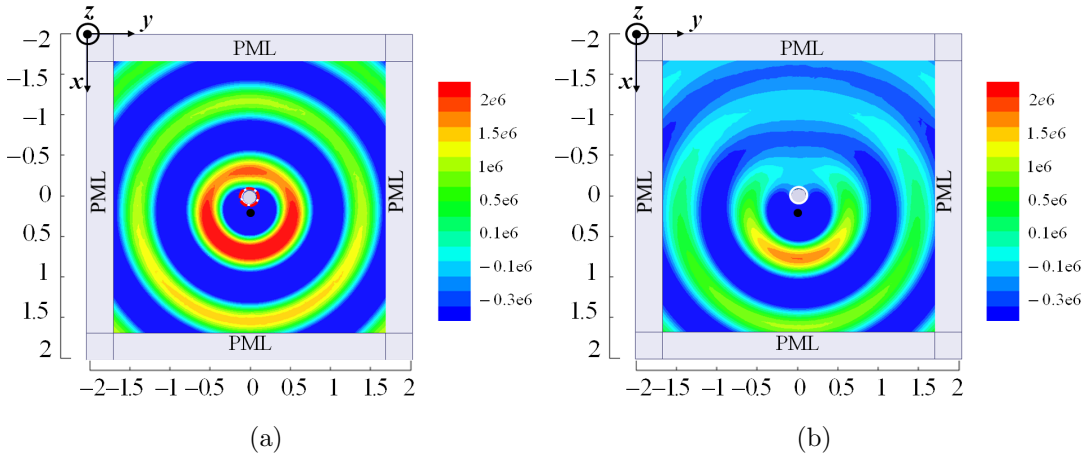


**Figure 5.14.** Full-wave numerical results of magnitude of E-field distributions on the $\phi$-plane: (a) with the patch array cloak, and (b) without the cloak.

Clearly, it can be observed that the dielectric cylinder covered by conformal mesh grid is cloaked for all the positions of the line source, where unperturbed cylindrical wavefronts of the line source are observed. Further, it is interesting to see that the mantle cloaking is effective even when the line source is in very close proximity ($d = 0.015\lambda_0$) to the object. To verify these results, in Fig. 5.20 we plot similar field distributions obtained using the full-wave numerical simulations. Again, the results not only corroborate the mantle cloaking effect, but also verify the analytical results shown in Fig. 5.19. Although, the qualitative agreement between the analytical and numerical results is good, it is necessary to verify the quantitative nature of the field behavior predicted by the analytical model, particularly for the line source in close proximity to the mesh grid/other periodic patterned surface cloaks. This is because, the analytical grid-impedance expressions used in this work, are originally derived and validated for planar surfaces for plane-wave incidence [34, 35], [37, 38, 40, 41]. In chapter IV, we have successfully shown and verified the accuracy of these expressions for tailoring the surface reactance properties of the cylindrical FSS arrays for plane-wave incidence. Recently in [93], the authors have studied the scattering problem of various

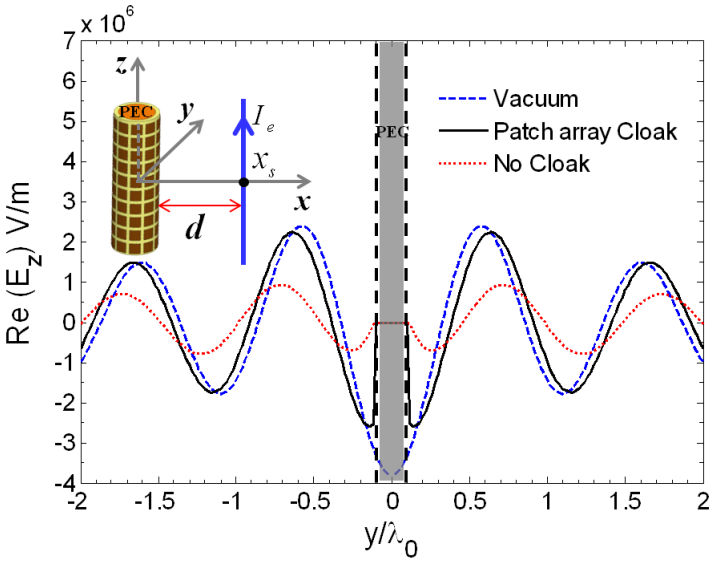


**Figure 5.15.** Real part of $E_z$ along the $y$-axis calculated using the analytical model. The vertical dashed bold lines represent the position of the patch array cloak, and the shaded region represents the conducting cylinder.

planar FSS arrays on grounded dielectric slabs excited by an aperiodic line source, wherein analytical grid-impedance expressions [35], [34], [40], and [41] have been used in characterizing the grid impedance of the planar FSS arrays. A detailed study in regard to the position of the line source, observation points, and the periodicity of the FSS arrays has been carried out and some important conclusions with respect to the accuracy of the analytical grid-impedance expressions were drawn. Hence, there is a certain necessity for validating these expressions especially when illuminated by a line source in close proximity to cylindrical patterned surfaces, and in the following we demonstrate their accuracy and comment on their behavior.

We first consider a dielectric cylinder covered by the conformal mesh grid with geometry shown in Fig. 5.4 (for parameters of the object and the cloak, see Section 5.3.1). Figures 5.21, 5.22, and 5.23 show the variation of $Re(E_z)$ versus observation angle $\phi$ for different positions of the line source $d$ at various observation points $\rho$ (with $d_2$ being the distance between the surface of the cloak and the observation point, whose geometry is shown in the inset of Figs. 5.21, 5.22, and 5.23). Results

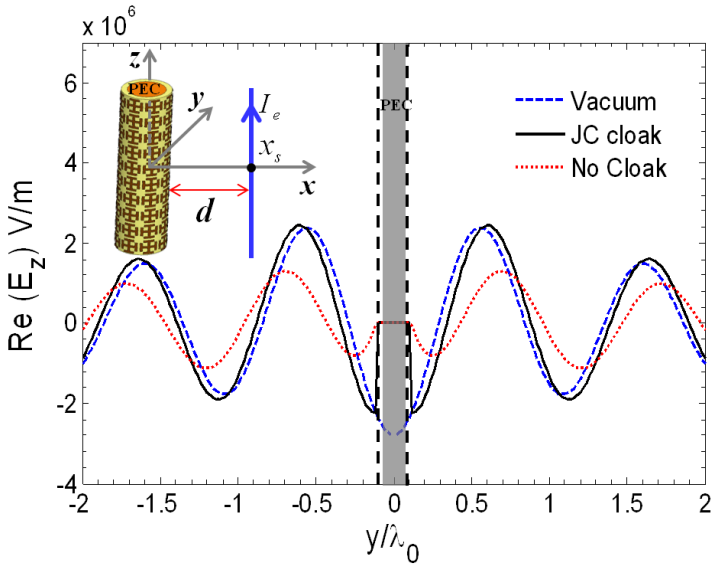


**Figure 5.16.** Real part of $E_z$ along the $y$-axis calculated using the analytical model. The vertical dashed bold lines represent the position of the slotted Jerusalem crosses cloak, and the shaded region represents the dielectric cylinder, with the medium between the cloak and the object being free-space.

obtained using full-wave numerical simulations are reported in order to validate the accuracy of the analytical model. The parameters of the conformal mesh grid and that of the dielectric cylinder are kept the same in all the cases. Figure 5.21 shows the variation of $Re(E_z)$ versus observation angle $\phi$ for an electric line source located at $d = 0.015\lambda_0$ in very close proximity to the object and the cloak, for different observation points: $d_2 = 0.002\lambda_0$, $d_2 = 0.1\lambda_0$, and $d_2 = 0.4\lambda_0$. It can be observed that, the results obtained by the analytical model show strong disagreements with the numerical results. This is because, the cylindrical FSS cloak lies very close to the line source, where the approximation of the analytical grid-impedances does not hold. The analytical expressions are valid provided: 1) the incident field produced by the line source varies little over the unit-cell of the FSS array and the evanescent fields have zero amplitude at the cloak interface, and 2) the evanescent fields scattered by the cloak have negligible amplitude at the observation points. For condition 1) to be satisfied the location of the line source should be such that $d > D$, where $D$ is the period of the FSS elements or in this analysis the mesh grid structure. Also,

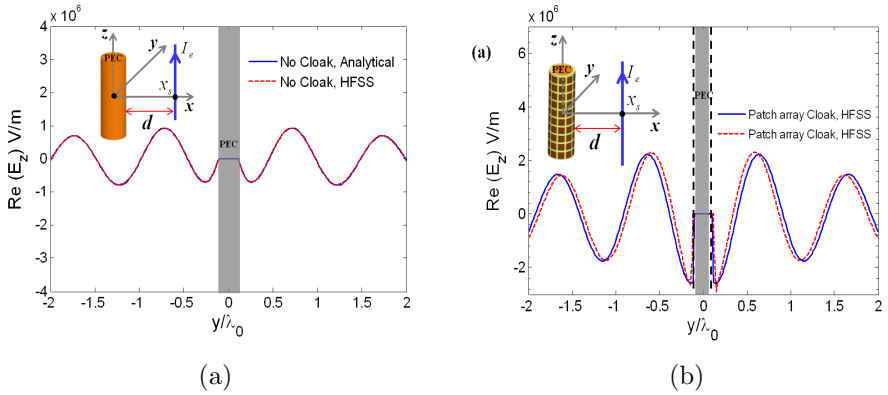


**Figure 5.17.** Verification of the analytical results shown in Figs. 6.14 and 6.15, using full-wave numerical simulations: (a) with and (b) without the patch array cloak; (c) with and (d) without the Jerusalem crosses cloak.

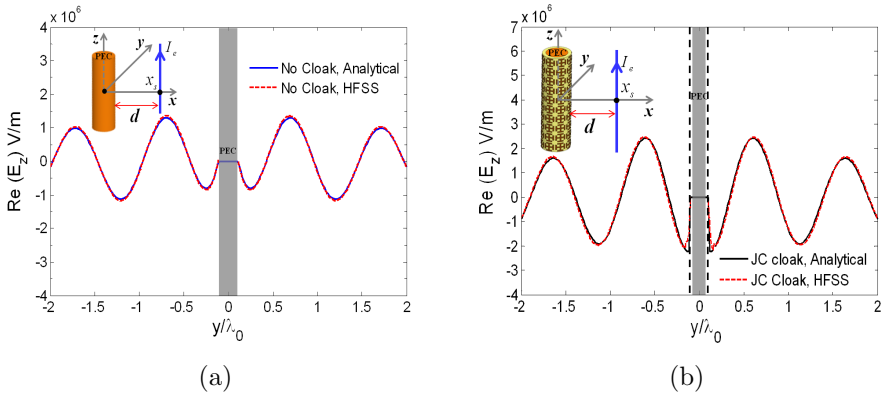


**Figure 5.18.** Verification of the analytical results shown in Figs. 14 and 15, using full-wave numerical simulations: (a) with and (b) without the Jerusalem crosses cloak.

for condition 2) to be satisfied, the observation point should be such that $d_2 \geq D$. Although, for the observation point located in close proximity $d_2 = 0.002\lambda_0$, the disagreement is reasonably expected, it is interesting to notice that even for the observation points far away $d_2 \geq D$ ( $d_2 = 0.1\lambda_0$ and $d_2 = 0.4\lambda_0$), the analytical results shown in Figs. 5.21(b) and 5.21(c) are still not accurate enough. This is due to the fact that the limitation on $d$ is not satisfied. In spite of the quantitative discrepancies in the prediction of the exact field behavior, an acceptable qualitative agreement of the cloaking effect (shown in Figs. 5.19(a) and 5.20(a)) is still observed.

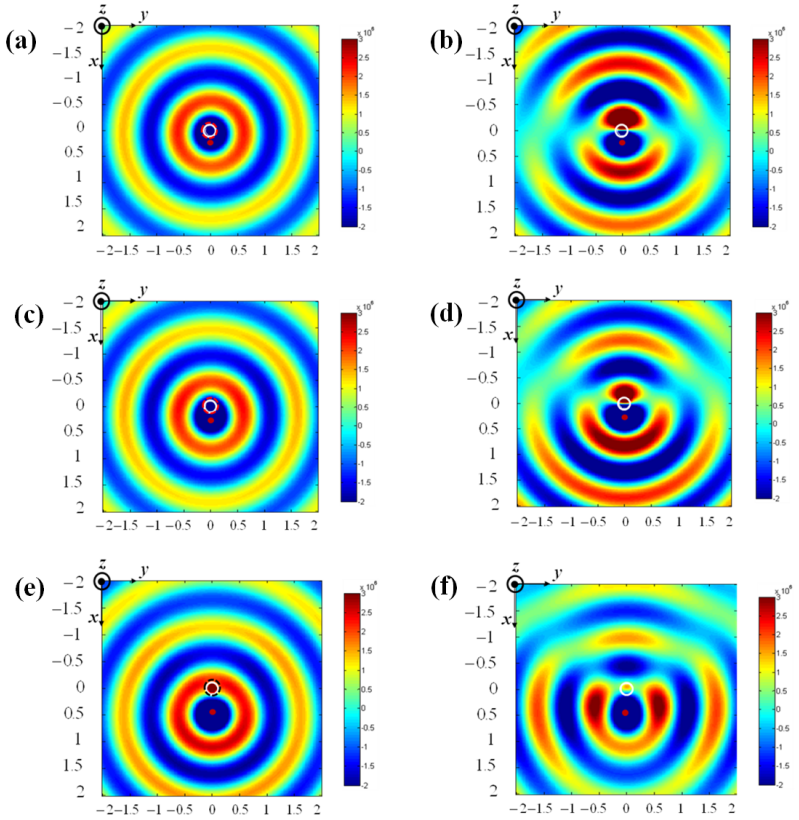


**Figure 5.19.** Electric field distributions obtained using the analytical model for $d = 0.015\lambda_0$: (a) with and (b) without the mesh grid cloak; for $d = 0.1\lambda_0$: (c) with and (d) without the mesh grid cloak; for $d = 0.4\lambda_0$: (e) with and (f) without the mesh grid cloak.

To further investigate the applicability of the analytical model, we consider now the cases when $d \geq D$: 1) $d = 0.1\lambda_0$ and 2) $d = 0.4\lambda_0$, for the observation points: $d_2 = 0.01\lambda_0$, $d_2 = 0.2\lambda_0$, $d_2 = 0.5\lambda_0$, and $d_2 = 0.7\lambda_0$, and study the variation of $Re(E_z)$ as a function of $\phi$. The analytical results are reported in Figs. 5.22 and 5.23 along with the full-wave numerical comparisons. It can be observed that in both the cases $d = 0.1\lambda_0$ and $d = 0.4\lambda_0$ excellent agreements between the analytical and full-wave simulations are obtained for $d_2 = 0.2\lambda_0$, $d_2 = 0.5\lambda_0$, and $d_2 = 0.7\lambda_0$. This is because the amplitude of evanescent fields produced by the line source at the cloak interfaces is negligible, and the amplitude of evanescent fields scattered by the grid are negligible at the observation points. For the observation point very close to the cloak $d_2 = 0.01\lambda_0$, strong disagreements can be seen for different $d$. This is expected taking into account

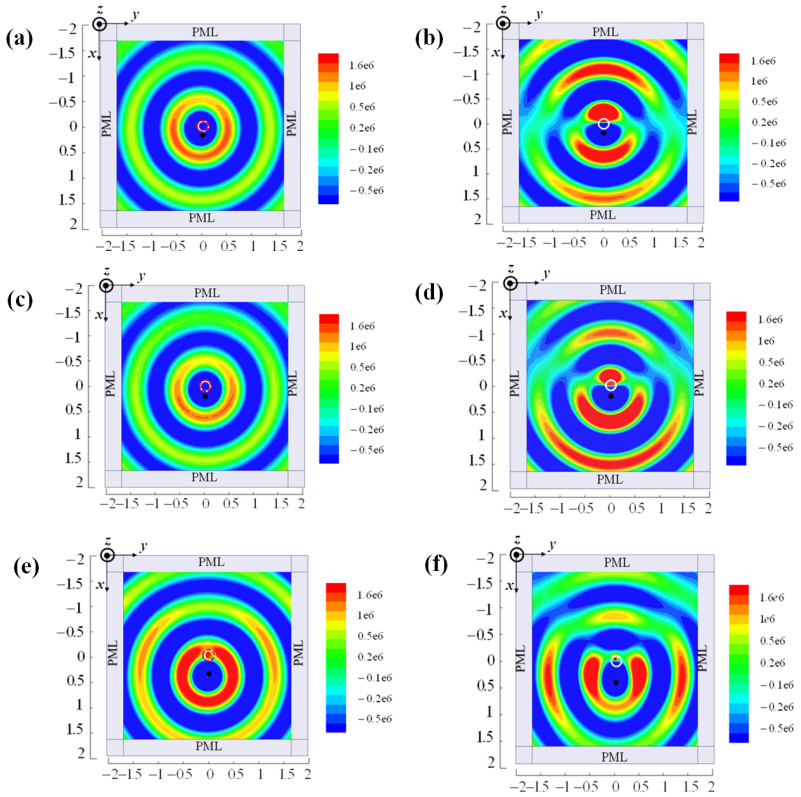


**Figure 5.20.** Electric field distributions obtained using the full-wave numerical simulations for $d = 0.015\lambda_0$: (a) with and (b) without the mesh grid cloak; for $d = 0.1\lambda_0$: (c) with and (d) without the mesh grid cloak; for $d = 0.4\lambda_0$: (e) with and (f) without the mesh grid cloak.

the evanescent field scattered by the grid is significant at the observation point. Hence, the true field (microscopic field) calculated by the numerical solver shows oscillations in the field behavior, while the averaged field (macroscopic field averaged over one unit-cell) is well represented by the analytical model (particularly, in Fig. 5.22). In Figs. 5.24, 5.25, and 5.26 a similar analysis has been carried out for the other patterned cloaks (slotted Jerusalem crosses, patch arrays, and Jerusalem crosses). For the sake of brevity, here the results are shown only for one specific location of the line source, i.e., $d = 0.1\lambda_0$ for slotted Jerusalem crosses and patch arrays and $d = 0.15\lambda_0$ for Jerusalem crosses, such that $d \geq D$, where $D$ is period of the corresponding sub-wavelength FSS arrays. The parameters of the cloaks and the objects are similar to those considered in Section 5.3 for the respective cases, and the field behaviors are

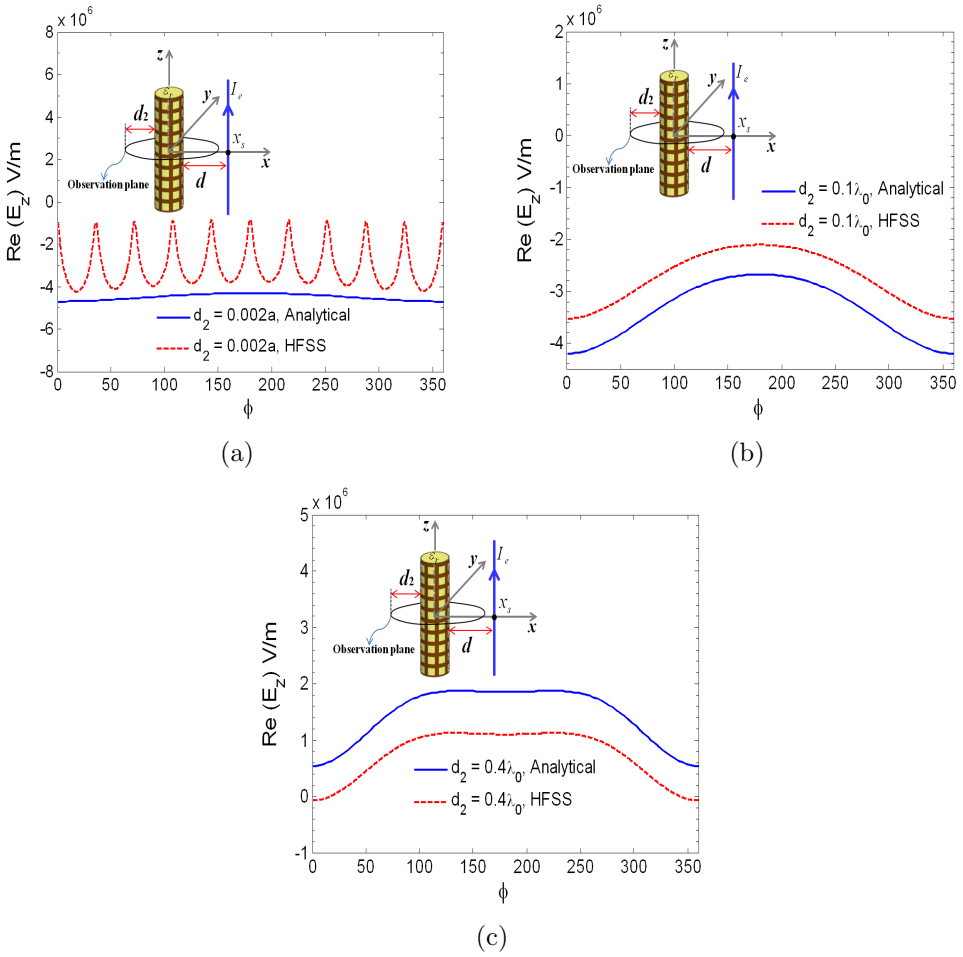


**Figure 5.21.** Electric field distributions around a mesh grid covered dielectric cylinder illuminated by a line source located at $d = 0.015\lambda_0$, as a function of azimuthal angle ($\phi$) at design frequency $f_0$ for different observation positions: (a) $d_2 = 0.002\lambda_0$, (b) $d_2 = 0.1\lambda_0$, and (c) $d_2 = 0.4\lambda_0$. The analytical results are represented by solid lines and full-wave simulation results by dashed, dot, and dot-dashed lines.

calculated at different observation points away from the cloaks and compared with the full-wave numerical simulations. It can be observed that for $d_2 < D$ the analytical results in all the cases show some disagreements with the numerical results, and the comparisons show improvement as $d_2$ increases. i.e., for $d_2 = 0.2\lambda_0$ and $d_2 = 0.5\lambda_0$. Also, it is worth mentioning that in all the cases studied in this work, the position of the line source is not varied azimuthally ($\phi_s$). In fact, we have studied the cloaking mechanism with respect to ($\phi_s$) and still observed the same effect, however, the results

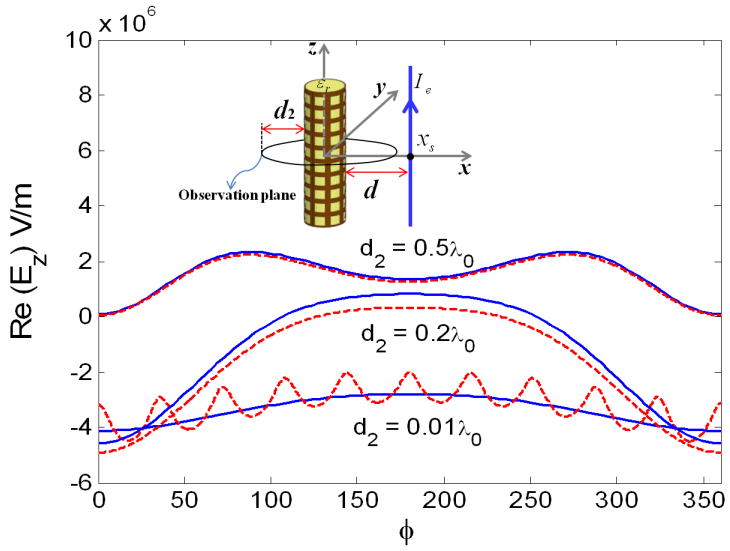


**Figure 5.22.** Same as in Fig. 6.21, except for $d = 0.1\lambda_0$, $d_2 = 0.01\lambda_0$, $d_2 = 0.2\lambda_0$, and $d_2 = 0.5\lambda_0$.

are not shown here for the sake of brevity.

## 5.5 Low-profile Conformal Antenna Applications

In this section, we study the electromagnetic radiation of an electric line source scattered by an infinite metallic cylinder coated with a conformal patterned FSS sheet. The idea behind this concept is based on the procedure carried out in chapter IV, where we studied the mantle cloaking of metallic cylinders covered by various patterned FSS cloaks. In fact it was observed that at higher frequencies, the FSS covered metallic cylinder showed an enhancement in the scattering width (SW) properties when compared to the uncoated cylinder. The reason behind this mechanism is due to the fact that the the currents induced on the surface of the cloak generate fields which are in-phase with the fields scattered by the cylinder, and hence an enhancement in the SW. Utilizing this property of the cloak, here we study the far-field radiation properties of the line source in the presence of an conformal FSS patterned sheet covered metallic cylinder. The cloak is realized using sub-wavelength patch

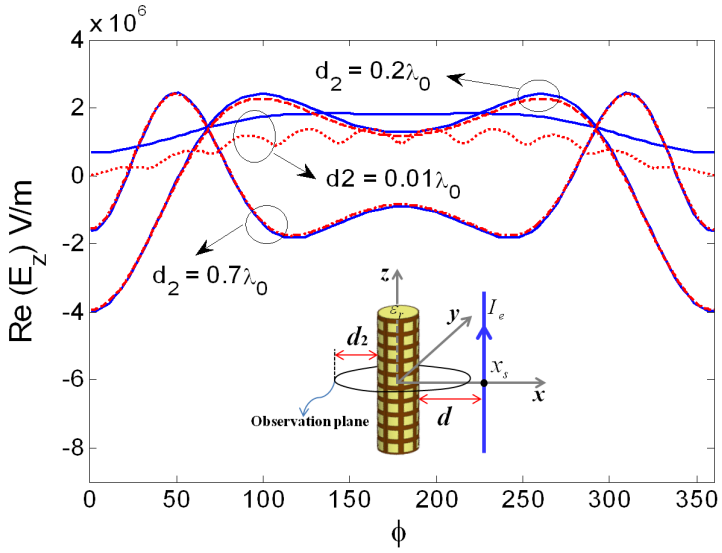


**Figure 5.23.** Same as in Fig. 6.21, except for $d = 0.4\lambda_0$, $d_2 = 0.01\lambda_0$, $d_2 = 0.2\lambda_0$, and $d_2 = 0.7\lambda_0$.

arrays, whose parameters can be found in Table 5.1 in Section 5.3.2, and the line source is located at $d = 0.1\lambda_0$. After several investigations, it is found that in fact at higher frequencies ($f/f_0 = 1.33$) where there was an enhancement in the SW (see Fig. 4.17a), the far-field radiation characteristics of the line source in the presence of the covered metallic cylinder showed an improvement in the directivity and enhancement of field in the forward direction ($\phi = 0°$). The details are given in Fig. 5.27, where it can be observed that using the patch array screen significant improvements of the figures of merit mentioned above are achieved. Although, improved directivity is achieved using the FSS patterned sheet, some significant amount of back radiation is still present. Better optimized screens can be designed to reduce these effects, however, these concepts go beyond the scope of this work and will be dealt in near future. It should be noted that using the same patch array cover with the same parameters, the cloaking effect can still be realized at the design frequency ($f_0$) as shown in Section 5.3.2.

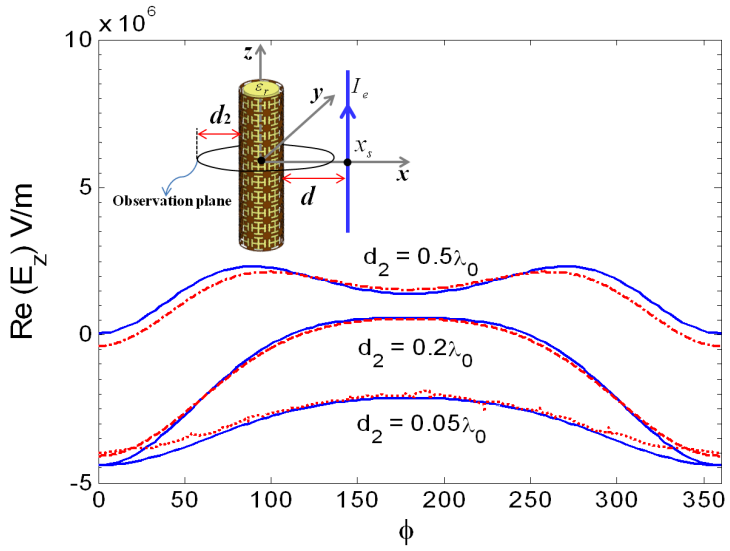


**Figure 5.24.** Electric field distributions around a slotted Jerusalem crosses cloak covered dielectric cylinder illuminated by a line source located at $d = 0.1\lambda_0$, as a function of azimuthal angle ($\phi$) at design frequency $f_0$ for different observation positions: (a) $d_2 = 0.05\lambda_0$, (b) $d_2 = 0.2\lambda_0$, and (c) $d_2 = 0.5\lambda_0$. The analytical results are represented by solid lines and full-wave simulation results by dashed, dot, and dot-dashed lines.

## 5.6 Large Objects

We further extend the previous concepts to large objects, i.e., mantle cloaking of large 2-D cylinders using sub-wavelength FSS arrays, illuminated by the line source. We consider two dielectric cylinders with radii $a = \lambda_0/6$ and $a = \lambda_0/4$. We first study the SW properties of the these two cylinders covered by a an ideal mantle cloak with radius $a_c$, characterized by a homogeneous, lossless, and dispersionless surface reactance $X_s$ (analogous to the study carried out in [23,24]) for plane-wave incidence. It was observed that the cloak with inductive response may significantly reduce the overall scattering (the results are omitted here for the sake of brevity). Based on the required values of $X_s$, the mantle cloak is then realized using an inductive mesh grid, whose geometry is shown in Fig. 5.4. The parameters of the mesh grid cloaks for the two dielectric cylinders are given in Table 5.2. It should be noted that the required $X_s$ of the ideal mantle cloak is achieved by optimizing the parameters of the

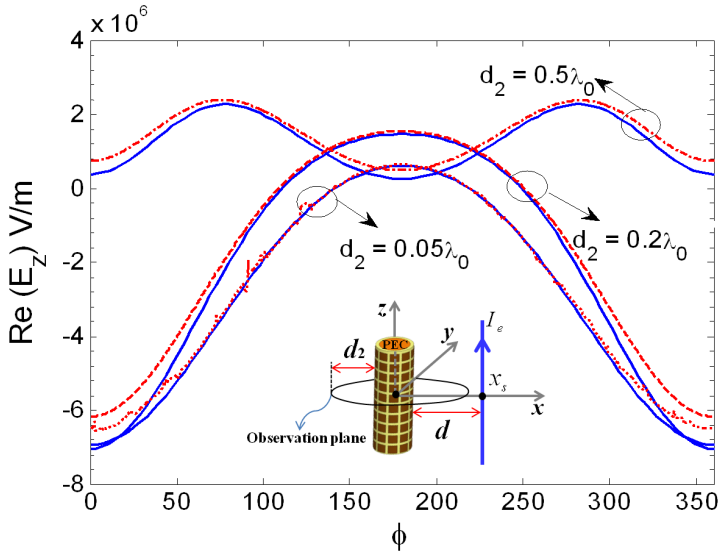


**Figure 5.25.** Electric field distributions around a slotted Jerusalem crosses cloak covered dielectric cylinder illuminated by a line source located at $d = 0.1\lambda_0$, as a function of azimuthal angle ($\phi$) at design frequency $f_0$ for different observation positions: (a) $d_2 = 0.05\lambda_0$, (b) $d_2 = 0.2\lambda_0$, and (c) $d_2 = 0.5\lambda_0$. The analytical results are represented by solid lines and full-wave simulation results by dashed, dot, and dot-dashed lines.

mesh grid using the analytical grid-impedance expression given in the Appendix. We then study the cloaking effect in the presence of a line source. A suitable location of the line source is chosen based on the conditions outlined in Section 5.4. In Figs. 5.28 and 5.29 we show the analytical results for two large dielectric cylinders covered with and without the mesh grid cloaks. Comparing the cloaked and uncloaked cases, the

**Table 5.2.** Parameters of the mesh grid cloak conformal to a dielectric cylinder.

| $a$ | N | $D$ | $w$ | $\varepsilon_r$ | $a_c$ | $d$ |
|---|---|---|---|---|---|---|
| $\lambda_0/6$ | 10 | $\lambda_0/10$ | $\lambda_0/83$ | 3.9 | $a$ | $0.1\lambda_0$ |
| $\lambda_0/4$ | 15 | $\lambda_0/10$ | $\lambda_0/154$ | 4.4 | $a$ | $0.1\lambda_0$ |

first obvious conclusion is that the mantle cloaking is still excellent, clearly restoring the cylindrical wave fronts of the line source, despite the large electrical size of the objects. Although the above results are in excellent agreement with the full-wave numerical results, their results are not included here for the sake of brevity.

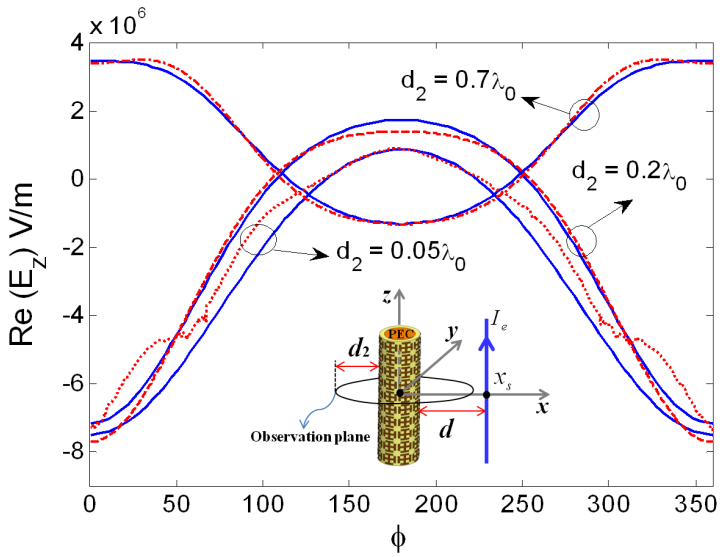


**Figure 5.26.** Electric field distributions around a slotted Jerusalem crosses cloak covered dielectric cylinder illuminated by a line source located at $d = 0.15\lambda_0$, as a function of azimuthal angle ($\phi$) at design frequency $f_0$ for different observation positions: (a) $d_2 = 0.05\lambda_0$, (b) $d_2 = 0.2\lambda_0$, and (c) $d_2 = 0.7\lambda_0$. The analytical results are represented by solid lines and full-wave simulation results by dashed, dot, and dot-dashed lines.

## 5.7 Conclusions

We have investigated here the concept of mantle cloaking technique applied to dielectric and conducting cylinders covered by various printed and slotted conformal sub-wavelength FSS arrays, illuminated by an electric line source. It has been shown that the conditions derived for the mantle cloak surface for plane-wave incidence are still valid for the line source present in the close proximity. An analytical model is proposed to carry out the electromagnetic scattering analysis. A detailed study in regard to the application of the analytical expressions (which are derived for the planar FSS elements) for tailoring the surface reactance of cylindrical conformal mantle cloaks which are present in the intense near field of a line source, has been carried out. Comparisons with numerical results have been shown to validate the analytical model results. In addition, mantle cloaking of large cylindrical dielectric objects illuminated by an electric line source is shown. Applications to low-profile conformal antennas

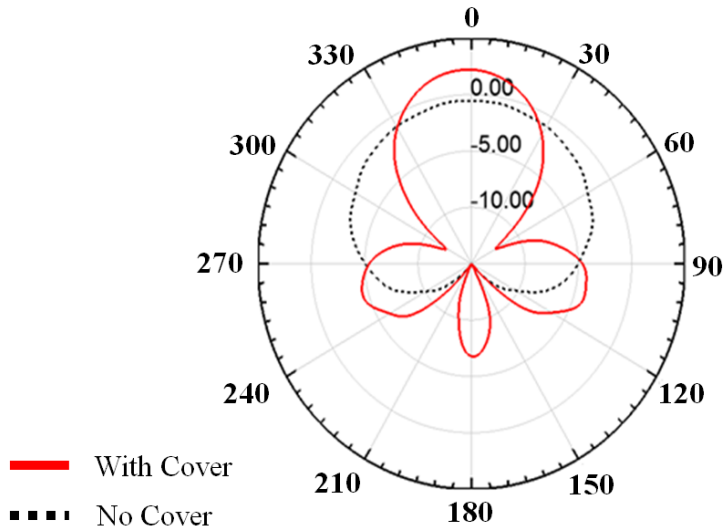


**Figure 5.27.** Directivity (dB) of the electric line source placed in front of a metallic cylinder with and without the conformal patch array screen.

have also been demonstrated and discussed. The analysis presented in this work can be extended to study cloaking in the presence of a magnetic line source.

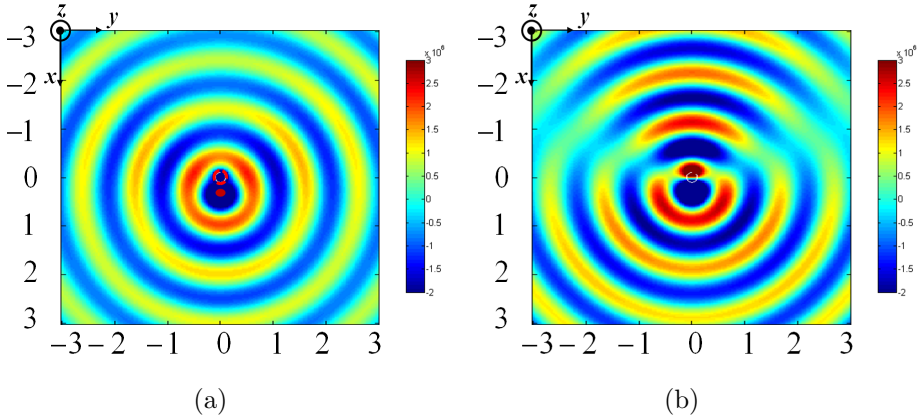


**Figure 5.28.** Analytical results of magnitude of E-field distributions on the $\phi$-plane for a dielectric cylinder with $\varepsilon_r = 4.4$ and radius $a = \lambda_0/6$: (a) with the mesh grid cloak and (b) without the cloak.

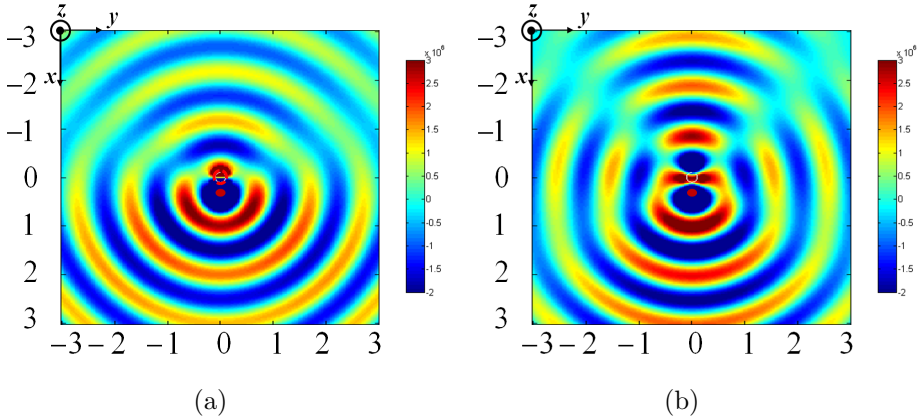


**Figure 5.29.** Analytical results of magnitude of E-field distributions on the $\phi$-plane for a dielectric cylinder with $\varepsilon_r = 3.9$ and radius $a = \lambda_0/4$: (a) with the mesh grid cloak and (b) without the cloak.

# CHAPTER 6

# CONCLUDING REMARKS AND FUTURE WORK

Metamaterials consisting of stacked metasurfaces and mushroom structures have been considered in this work. In the second chapter, a simple analytical model to characterize the absorption properties of a multilayered metasurface has been presented. Details of the additional boundary conditions and analytical model derived for the multilayered mushroom structure have been presented in the third chapter. Further, analytical models to characterize the cloaking structures are presented in Chapter IV and V.

The work carried out in the dissertation can be summarized as follows: First, a simple circuit model has been applied to the analysis of the absorption properties of multilayer structures with sub-wavelength dimensions in the microwave regime. The results obtained by this method are in complete agreement with the numerical simulations. The physical mechanisms of the observed absorption resonances are clearly explained in terms of the behavior of a finite number of strongly coupled FP resonators. The observed resonances have been characterized by studying the electromagnetic field behavior using the circuit model and numerical simulations. Next, additional boundary conditions for the double-sided junctions of wire media with thin resistive patches at the interface are derived. Further, a simple analytical model

has been presented to analyze the reflection properties of multilayered mushroom HIS structures with thin resistive patches. The limitations and applicability of the new boundary conditions have been studied, particularly for the two-layer mushroom structure, and the analytical model results have been verified using full-wave simulations. Also, a design procedure for selecting resistivities of the patch arrays has been presented.

Finally, we have presented an analytical model to design practical mantle cloaks tailored to suppress the scattering from dielectric and conducting cylindrical objects for both plane-wave incidence and line sources in close proximity using various sub-wavelength periodic surfaces. It has been shown that the suitable design of a conformal mantle cloak may significantly reduce the scattering from cylindrical rods and analytical formulas to derive the required surface reactance of the conformal surface may be borrowed from established models for planar FSS. Our analytical results, based on the grid-impedance expressions available for planar geometries, have been validated using full-wave numerical simulations.

The research conducted in this dissertation opens up new possibilities in future research, among which are the analysis of cloaking of large objects using multilayered conformal sub-wavelength patterned mantle cloaks for oblique plane wave incidences (TM and TE) and in the presence of electric and magnetic line sources, analysis of scattering characteristics of mushroom structures conformed to a conducting cylinder (shown in Fig. 6.1) for an oblique incident TM-polarized plane wave and for an electric line source present in the vicinity, and for the analysis of the scattering behavior from the metallic cylinder covered by a number of lossy sub-wavelength patterned metasurface layers for normal and obliquely incident uniform plane wave for TM and TE polarizations.

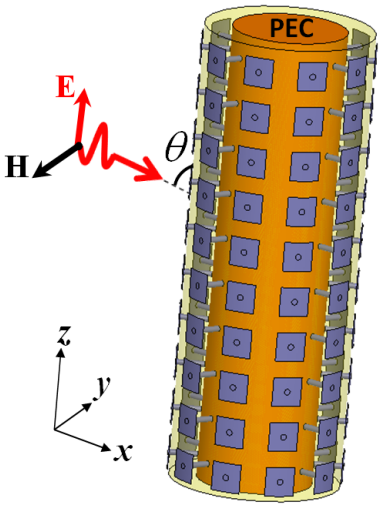


**Figure 6.1.** Geometry of the conducting cylinder covered by mushroom structure.

# BIBLIOGRAPHY

# Bibliography


[1] B. A. Munk, *Frequency Selective Surfaces: Theory and Design.* Wiley, 2000.

[2] W. W. Salisbury, "Absorbent body of electromagnetic waves," *IEEE Trans. Antennas Propagat. Mag.*, June 1952.

[3] L. J. D. Toit, "The design of jaumann absorbers," *IEEE Trans. Antennas Propagat. Mag.*, vol. 36, pp. 17–25, June 1994.

[4] N. I. Landy, S. Sajuyigbe, J. J. Mock, D. R. Smith, and W. J. Padilla, "Perfect metamaterial absorber," *Phys. Rev. Lett.*, vol. 100, p. 207402, May 2008.

[5] B. Wang, T. Koschny, and C. M. Soukoulis, "Wide-angle and polarization-independent chiral metamaterial absorber," *Phys. Rev. B*, vol. 80, p. 033108, Jul 2009.

[6] M. Diem, T. Koschny, and C. M. Soukoulis, "Wide-angle perfect absorber/thermal emitter in the terahertz regime," *Phys. Rev. B*, vol. 79, p. 033101, Jan 2009.

[7] H. Tao, C. M. Bingham, A. C. Strikwerda, D. Pilon, D. Shrekenhamer, N. I. Landy, K. Fan, X. Zhang, W. J. Padilla, and R. D. Averitt, "Highly flexible wide angle of incidence terahertz metamaterial absorber: Design, fabrication, and characterization," *Phys. Rev. B*, vol. 78, p. 241103, Dec 2008.

[8] N. I. Landy, C. M. Bingham, T. Tyler, N. Jokerst, D. R. Smith, and W. J. Padilla, "Design, theory, and measurement of a polarization-insensitive absorber for terahertz imaging," *Phys. Rev. B*, vol. 79, p. 125104, Mar 2009.

[9] X. Liu, T. Starr, A. F. Starr, and W. J. Padilla, "Infrared spatial and frequency selective metamaterial with near-unity absorbance," *Phys. Rev. Lett.*, vol. 104, p. 207403, May 2010.

[10] Y. Avitzour, Y. A. Urzhumov, and G. Shvets, "Wide-angle infrared absorber based on a negative-index plasmonic metamaterial," *Phys. Rev. B*, vol. 79, p. 045131, Jan 2009.

[11] J. Hao, J. Wang, X. Liu, W. J. Padilla, L. Zhou, and M. Qiu, "High performance optical absorber based on a plasmonic metamaterial," *Appl. Phys. Lett.*, vol. 96, p. 251104, June 2010.

[12] F. Bilott, A. Toscano, K. B. Alici, E. Ozbay, and L. Vegni, "Design of miniaturized narrowband absorbers based on resonant magnetic inclusions," *IEEE Trans. Electromag. Compat.*, vol. 53, pp. 63–72, 2011.

[13] N. Engheta, "Thin absorbing screens using metamaterial surfaces," *Proc. IEEE Int. Symp. Antennas Propag.*, vol. 2, pp. 392–395, 2002 (San Antonio, TX).

[14] S. Simms and V. Fusco, "Thin absorber using artificial magnetic ground plane," *Electron. Lett.*, vol. 41, pp. 1311–1313, 2005.

[15] H. Mosallaei and K. Sarabandi, "A one-layer ultrathin meta-surface absorber," *Proc. IEEE Int. Symp. Antennas Propag.*, Jul. 2005 (Washington, D.C.).

[16] Q. Gao, Y. Yin, D. B. Yan, and N. C. Yuan, "A novel radarabsorbingmaterial based on ebg structure," *Microw. Opt. Technol. Lett.*, vol. 47, pp. 228–230, 2005.

[17] B. A. Munk, P. Munk, and J. Pryor, "On designing jaumann and circuit analog absorbers (ca absorbers) for oblique angle of incidence," *IEEE Trans. Antennas Propag.*, vol. 55, pp. 186–193, Jan. 2007.

[18] A. Kazemzadeh and A. Karlsson, "Capacitive circuit method for fast and efficient design of wideband radar absorbers," *IEEE Trans. Antennas Propag.*, vol. 57, pp. 2307–2314, 2009.

[19] A. Kazemzadeh and A. Karlsson, "Nonmagnetic ultrawideband absorber with optimal thickness," *IEEE Trans. Antennas Propag.*, vol. 59, pp. 135–140, Jan. 2011.

[20] A. Kazemzadeh and A. Karlsson, "Multilayered wideband absorbers for oblique angle of incidence," *IEEE Trans. Antennas Propag.*, vol. 58, pp. 3637–3646, Nov. 2010.

[21] S. A. Tretyakov and S. I. Maslovski, "Thin absorbing structures for all incidence angles based on the use of a high-impedance surface," *Microw. Opt. Technol. Lett.*, vol. 38, pp. 153–157, 2003.

[22] O. Luukkonen, F. Costa, C. R. Simovsk, A. Monorchio, and S. A. Tretyakov, "A thin electromagnetic absorber for wide incidence angles and both poalrizations," *IEEE Trans. Antennas Propag.*, vol. 57, pp. 3119–3124, Oct. 2009.

[23] A. Alù, "Mantle cloak: Invisibility induced by a surface," *Phys. Rev. B*, vol. 80, p. 245115, Dec 2009.

[24] P.-Y. Chen and A. Alù, "Mantle cloaking using thin patterned metasurfaces," *Phys. Rev. B*, vol. 84, p. 205110, Nov 2011.

[25] P.-Y. Chen and A. Alù, "Atomically thin surface cloak using graphene monolayers," *ACS NANO*, vol. 5, pp. 5855–5863, Jun. 2011.

[26] L. J. D. Toit and J. H. Cloete, "Electric screen jauman absorber design algorithms," *IEEE Trans. Microw. Theory Tech.*, vol. 44, pp. 2238–2245, 1996.

[27] S. Chakravarty, R. Mittra, and N. R. Williams, "Application of the microgenetic algorithm (mga) to the design of broad-band microwave absorbers using multiple frequency selective surface screens buried in dielectrics," *IEEE Trans. Antennas Propag.*, vol. 50, pp. 284–296, 2002.

[28] S. Datta, C. T. Chan, K. M. Ho, and C. M. Soukoulis, "Effective dielectric constant of periodic composite structures," *Phys. Rev. B*, vol. 48, pp. 14936–14943, Nov 1993.

[29] M. G. Silveirinha and C. A. Fernandes, "Effective permittivity of metallic crystals: A periodic greens function formulation," *Electromagnetics*, vol. 8, pp. 647–663, 2003.

[30] M. G. Silveirinha and C. A. Fernandes, "Homogenization of metamaterial surfaces and slabs: the crossed wire mesh canonical problem," *IEEE Trans. Antennas Propag.*, vol. 53, pp. 59–69, Jan. 2005.

[31] M. G. Silveirinha, "Nonlocal homogenization model for a periodic array of "-negative rods," *Phys. Rev. E*, vol. 73, p. 046612, 2006.

[32] M. G. Silveirinha, "Additional boundary conditions for nonconnected wire media," *New J. Phys.*, vol. 11, p. 053011, 2009.

[33] J. D. Jackson, *Classical Electrodynamics*. Wiley, New York, 1998.

[34] O. Luukkonen, C. Simovski, G. Grant, G. Goussetis, D. Lioubtchenko, A. Raisanen, and S. Tretyakov, "Simple and accurate analytical model of planar grids and high-impedance surfaces comprising metal strips and patches," *IEEE Trans. Antennas Propag.*, vol. 56, pp. 1624–1632, Jun. 2008.

[35] S. Tretyakov, *Analytical Modeling in Applied Electromagnetics*. Artech House, Norwood MA, 2003.

[36] *HFSS: High Frequency Structure Stimulator based on Finite Element Method, http://www.ansoft.com*. 2009.

[37] Y. R. Padooru, A. B. Yakovlev, C. S. R. Kaipa, F. Medina, and F. Mesa, "Circuit modeling of multiband high-impedance surface absorbers in the microwave regime," *Phys. Rev. B*, vol. 84, p. 035108, Jul 2011.

[38] C. S. R. Kaipa, A. B. Yakovlev, F. Medina, F. Mesa, C. A. M. Butler, and P. Alastair, "Circuit modeling of the transmissivity of stacked two-dimensional metallic meshes," *Opt. Express*, vol. 18, p. 13309, 2010.

[39] L. B. Whitbourn and R. C. Compton, "Equivalent-circuit formulas for metal grid reflectors at a dielectric boundary," *Appl. Opt.*, vol. 24, pp. 217–220, 1985.

[40] C. R. Simovski, P. D. Maagt, and I. V. Melchakova, "High-impedance surfaces having stable resonance with respect to polarization and incidence angle," *IEEE Trans. Antennas Propag.*, vol. 53, pp. 908–914, Mar. 2005.

[41] A. B. Yakovlev, O. Luukkonen, C. R. Simovski, S. A. Tretyakov, S. Paulotto, P. Baccarelli, and G. W. Hanson *Metamaterials and plasmonics: Fundamentals, Modeling, Applications, ser. NATO Science for Peace and Security B, Physics and Biophysics, S. Zhoudi, A. Sihvola, and A. P. Vinogradov, Eds. Dordrecht, The Netherlands: Springer*, pp. 908–914, 2009.

[42] C. R. Simovski, S. Zouhdi, and V. V. Yatsenko, "Electromagnetic interaction in dipole grids and prospective high-impedance surfaces," *Radio Science.*, vol. 40, 2005.

[43] C. F. Bohren and D. R. Huffman, *Absorption and Scattering of Light by Small Particles*. Wiley: New York, 1998.

[44] B. Wang, T. Koschny, and C. M. Soukoulis, "Wide-angle and polarization-independent chiral metamaterial absorber," *Phys. Rev. B*, vol. 80, p. 033108, Jul 2009.

[45] D. J. Kern and D. H.Werner, "Magnetic loading of ebg amc ground planes and ultrathin absorbers for improved bandwidth performance and reduced size," *Microw. Opt. Technol. Lett.*, vol. 48, pp. 2468–2471, Dec. 2006.

[46] F. Costa, A. Monorchio, and G. Manara, "Analysis and design of ultra thin electromagnetic absorbers comprising resistively loaded high impedance surfaces," *IEEE Trans. Antennas Propag.*, vol. 58, pp. 1551–1558, May 2010.

[47] Q. li Zhou, C. lin Zhang, K. jun Mu, B. Jin, L. liang Zhang, W. wei Li, and R. shu Feng, "Optical property and spectroscopy studies on the explosive 2,4,6-trinitro-1,3,5-trihydroxybenzene in the terahertz range," *Applied Physics Letters*, vol. 92, no. 10, p. 101106, 2008.

[48] L. Cugunov, A. Mednis, and J. Kliava, "Multiband electron spin resonance spectroscopy of rare-earth s ions in glasses: the isospectral frequency ratio method," *Journal of Physics: Condensed Matter*, vol. 3, no. 41, p. 8017, 1991.

[49] H. Tao, C. M. Bingham, D. Pilon, K. Fan, A. C. Strikwerda, D. Shrekenhamer, W. J. Padilla, X. Zhang, and R. D. Averitt, "A dual band terahertz metamaterial absorber," *Journal of Physics D: Applied Physics*, vol. 43, no. 22, p. 225102, 2010.

[50] Q.-Y. Wen, H.-W. Zhang, Y.-S. Xie, Q.-H. Yang, and Y.-L. Liu, "Dual band terahertz metamaterial absorber: Design, fabrication, and characterization," *Applied Physics Letters*, vol. 95, no. 24, p. 241111, 2009.

[51] J. Brown, "Artificial dielectrics having refractive indices less than unity," Oct.

[52] W. Rotman, "Plasma simulation by artificial dielectrics and parallel-plate media," *IRE Trans. Antennas Propag.*, vol. 10, pp. 82–95, Jan. 1962.

[53] R. Ulrich, "Far-infrared properties of metallic mesh and its complementary structure," *Infrared Phys.*, vol. 7, pp. 37–55, Jul. 1967.

[54] R. Sauleau, P. Coquet, J. P. Daniel, T. Matsui, and N. Hirose, "Study of fabry-perot cavities with metal mesh mirrors using equivalent circuit models. comparison with experimental results in the 60 ghz band," *International Journal of Infrared and Millimeter Waves*, vol. 19, pp. 1693–1710, 1998. 10.1023/A:1021771327991.

[55] N. Engheta, A. Salandrino, and A. Alù, "Circuit elements at optical frequencies: Nanoinductors, nanocapacitors, and nanoresistors," *Phys. Rev. Lett.*, vol. 95, p. 095504, Aug 2005.

[56] D. F. Sievenpiper, L. Zhang, R. F. J. Broas, N. G. Alexopoulos, and E. Yablonovich, "High-impedance electromagnetic surfaces with a forbidden frequency band," *IEEE Trans. Microw. Theory Tech.*, vol. 47, pp. 2059–2074, Nov 1999.

[57] W. McKinzie and S. Rogers, "A multi-band artificial magnetic conductor comprised of multiple fss layers," *Proc. IEEE Int. Symp. Antennas Propag.*, pp. 423–426, Jun. 2003 (Columbus, OH).

[58] Fabry and A. Perot *Ann. Chim. Phys.*, vol. 16, p. 115, 1899.

[59] J. A. Gordon, C. L. Holloway, and A. Dienstfrey, "A physical explanation of angle-independent reflection and transmission properties of metafilms/metasurfaces," *IEEE Antennas Wireless Propag. Lett.*, vol. 8, pp. 1127–1130, Sep. 2009.

[60] D. R. Smith, W. J. Padilla, D. C. Vier, S. C. Nemat-Nasser, and S. Schultz, "Composite medium with simultaneously negative permeability and permittivity," *Phys. Rev. Lett.*, vol. 84, pp. 4184–4187, May 2000.

[61] M. G. Silveirinha, "Broadband negative refraction with a crossed wire mesh," *Phys. Rev. B*, vol. 79, p. 153109, Apr 2009.

[62] P. A. Belov, Y. Hao, and S. Sudhakaran, "Subwavelength microwave imaging using an array of parallel conducting wires as a lens," *Phys. Rev. B*, vol. 73, p. 033108, Jan 2006.

[63] M. G. Silveirinha, P. A. Belov, and C. R. Simovski, "Subwavelength imaging at infrared frequencies using an array of metallic nanorods," *Phys. Rev. B*, vol. 75, p. 035108, Jan 2007.

[64] P. A. Belov, R. Marqués, S. I. Maslovski, I. S. Nefedov, M. Silveirinha, C. R. Simovski, and S. A. Tretyakov, "Strong spatial dispersion in wire media in the very large wavelength limit," *Phys. Rev. B*, vol. 67, p. 113103, Mar 2003.

[65] M. G. Silveirinha, C. A. Fernandes, and J. R. Costa, "Electromagnetic characterization of textured surfaces formed by metallic pins," *IEEE Trans. Antennas Propag.*, vol. 56, pp. 405–415, Feb 2008.

[66] M. G. Silveirinha, C. A. Fernandes, and J. R. Costa, "Additional boundary condition for a wire medium connected to a metallic surface," *New J. Phys.*, vol. 10, p. 053011, 2008.

[67] M. G. Silveirinha, "Additional boundary condition for the wire medium," *IEEE Trans. Antennas Propag.*, vol. 54, pp. 1766–1780, Feb 2006.

[68] S. I. Maslovski, T. A. Morgado, M. G. Silveirinha, C. S. R. Kaipa, and A. B. Yakovlev, "Generalized additional boundary conditions for wire media," *New J. Phys.*, vol. 12, p. 113047, 2010.

[69] M. G. Silveirinha and A. B. Yakovlev, "Negative refraction by a uniaxial wire medium with suppressed spatial dispersion," *Phys. Rev. B*, vol. 81, p. 233105, Jun 2010.

[70] A. Demetriadou and J. B. Pendry, "Taming spatial dispersion in wire metamaterial," *Journal of Physics: Condensed Matter*, vol. 20, no. 29, p. 295222, 2008.

[71] O. Luukkonen, M. G. Silveirinha, A. B. Yakovlev, C. R. Simovski, I. S. Nefedov, and S. A. Tretyakov, "Effects of spatial dispersion on reflection from mushroom-type artificial impedance surfaces," *IEEE Trans. Microw. Theory Tech.*, vol. 57, pp. 2692–2699, Nov. 2009.

[72] A. B. Yakovlev, M. G. Silveirinha, O. Luukkonen, C. R. Simovski, I. S. Nefedov, and S. A. Tretyakov, "Characterization of surface-wave and leaky-wave propagation on wire-medium slabs and mushroom structures based on local and nonlocal homogenization models," *IEEE Trans. Microw. Theory Tech.*, vol. 57, pp. 2700–2714, Nov. 2009.

[73] C. S. R. Kaipa, A. B. Yakovlev, and M. G. Silveirinha, "Characterization of negative refraction with multilayered mushroom-type metamaterials at microwaves," *Journal of Applied Physics*, vol. 109, no. 4, p. 044901, 2011.

[74] A. B. Yakovlev, Y. R. Padooru, G. W. Hanson, A. Mafi, and S. Karbasi, "A generalized additional boundary condition for mushroom-type and bed-of-nails-type wire media," *IEEE Trans. Microw. Theory Tech.*, vol. 59, pp. 527–532, Mar. 2011.

[75] C. S. R. Kaipa, A. B. Yakovlev, S. I. Maslovski, and M. G. Silveirinha, "Indefinite dielectric response and all-angle negative refraction in a structure with deeply-subwavelength inclusions," *Phys. Rev. B*, vol. 84, p. 165135, Oct 2011.

[76] G. W. Hanson, "Dyadic green's functions and guided surface waves for a surface conductivity model of graphene," *Journal of Applied Physics*, vol. 103, no. 6, p. 064302, 2008.

[77] J. B. Pendry, D. Schurig, and D. R. Smith, "Controlling electromagnetic fields," *Science*, vol. 312, no. 5781, pp. 1780–1782, 2006.

[78] U. Leonhardt, "Controlling electromagnetic fields," *Science*, vol. 312, no. 5781, pp. 1777–1780, 2006.

[79] D. Schurig, J. J. Mock, B. J. Justice, S. A. Cummer, J. B. Pendry, A. F. Star, and D. R. Smith, "Metamaterial electromagnetic cloak at microwave frequencies," *Science*, vol. 314, no. 5801, pp. 977–980, 2006.

[80] J. Valentine, J. Li, T. Zentgraf, G. Bartal, and X. Zhang, "An optical cloak made of dielectrics," *Nat. Mater*, vol. 8, pp. 568–571, 2009.

[81] T. Ergin, N. Stenger, P. Brenner, J. B. Pendry, and M. Wegener, "Three-dimensional invisibility cloak at optical wavelengths," *Science*, vol. 328, pp. 337–339, 2010.

[82] A. Alù and N. Engheta, "Achieving transparency with plasmonic and metamaterial coatings," *Phys. Rev. E*, vol. 72, p. 016623, Jul 2005.

[83] P. Alitalo, O. Luukkonen, F. Bongard, J.-F. Zrcher, J. R. Mosig, and S. A. Tretyakov, "A multi-band artificial magnetic conductor comprised of multiple fss layers," *Proc. IEEE Int. Symp. Antennas Propag.*, pp. 423–426, 2009.

[84] H. A. Yousuf, R. E. Mattis, and K. Kozminskir, "Light scattering at oblique incidence on two coaxial cylinders," *Appl. Opt*, vol. 3, pp. 4013–4024, Jun. 1994.

[85] A. Alù, D. Rainwater, and A. Kerkhoff, "Plasmonic cloaking of cylinders: finite length, oblique illumination and cross-polarization coupling," *New Journal of Physics*, vol. 12, no. 10, p. 103028, 2010.

[86] A. Alù and N. Engheta, "Cloaking a sensor," *Phys. Rev. Lett.*, vol. 102, p. 233901, Jun 2009.

[87] A. Alù and N. Engheta, "Cloaked near-field scanning optical microscope tip for noninvasive near-field imaging," *Phys. Rev. Lett.*, vol. 105, p. 263906, Dec 2010.

[88] B. Edwards, A. Alù, M. E. Young, M. Silveirinha, and N. Engheta, "Experimental verification of epsilon-near-zero metamaterial coupling and energy squeezing using a microwave waveguide," *Phys. Rev. Lett.*, vol. 100, p. 033903, Jan 2008.

[89] S. Tretyakov, P. Alitalo, O. Luukkonen, and C. Simovski, "Broadband electromagnetic cloaking of long cylindrical objects," *Phys. Rev. Lett.*, vol. 103, p. 103905, Sep 2009.

[90] D. Rainwater, A. Kerkhoff, J. C. Soric, G. Moreno, and A. Alù, "Experimental verification of three-dimensional plasmonic cloaking in free-space," *New Journal of Physics*, vol. 15, p. 013054, 2012.

[91] G. W. Milton and N. A. P. Nicorovicir, "On the cloaking effects associated with anomalous localized resonance," *Proc. R. Soc. London*, vol. Ser. A 462, pp. 3027–3059, 2006.

[92] C. A. Balanis, *Advanced Engineering Electromagnetics*. New York: Wiley, ed., 1989.

[93] S. Paulotto, P. Baccarelli, P. Burghignoli, G. Lovat, G. W. Hanson, and A. B. Yakovlev, "Homogenized green's functions for an aperiodic line source over planar densely-periodic artificial impedance surfaces," *IEEE Trans. Microw. Theory Tech.*, vol. 58, pp. 1807–1817, July 2010.

# APPENDIX

# Appendix A

# ANALYTICAL GRID IMPEDANCE EXPRESSIONS FOR THE PLANAR 1-D AND 2-D SUB-WAVELENGTH PERIODIC ELEMENTS

Based on the full-wave solution of a scattering problem from a dense grid of wires, with the averaged impedance boundary conditions, analytical dynamic models for the grid impedances $Z_s$ of various 1-D and 2-D sub-wavelength periodic elements [] have been obtained in terms of effective circuit parameters (capacitance and inductance). Several periodic patterns such as parallel strips, mesh grids, patches, Jerusalem crosses, cross dipoles, slotted Jerusalem crosses, and slotted cross dipoles are considered here, with the assumption that in each case, the sub-wavelength elements are at the air-dielectric interface, with $\varepsilon_1 = \varepsilon_0$ and $\varepsilon_2 = \varepsilon_0\varepsilon_r$.

## A.1 1-D elements

### A.1.1 Vertical strips

For the vertical strips as in Fig. 4.2(d) with electric field along the direction of strips [34, 35]

$$Z_{\mathrm{s}}^{\mathrm{TE,Vstrips}} = \frac{j\omega\eta_0 D}{2c\pi} \ln \csc\left(\frac{\pi w}{2D}\right) , \tag{A.1.1}$$

$$Z_s^{\mathrm{TM,Vstrips}} = \frac{j\omega\eta_0 D}{2c\pi} \ln\csc\left(\frac{\pi w}{2D}\right)\left(1 - \frac{\sin^2\theta_s}{\varepsilon_r + 1}\right) , \tag{A.1.2}$$

where $\theta_s = 90° - \theta$, $\eta_0$ is the free-space wave impedance, $\theta$ is the incidence angle, $D$, $g$, $w$ are the geometrical parameters shown in Fig. 4.1, and $c$ is the speed of light in vacuum.

### A.1.2 Horizontal Strips

For the horizontal strips as in Fig. 4.6(d) [34]

$$Z_s^{\mathrm{TE,Hstrips}} = \frac{-j\eta_0 c\pi}{\omega\left(\varepsilon_r + 1\right) D} \frac{1}{\ln\csc\left(\frac{\pi g}{2D}\right)} \frac{1}{\left(1 - 2\frac{\sin^2\theta_s}{\varepsilon_r + 1}\right)} , \tag{A.1.3}$$

$$Z_s^{\mathrm{TM,Hstrips}} = \frac{-j\eta_0 c\pi}{\omega\left(\varepsilon_r + 1\right) D} \frac{1}{\ln\csc\left(\frac{\pi g}{2D}\right)} . \tag{A.1.4}$$

## A.2 2-D elements

### A.2.1 Mesh grid array

For the mesh grid array shown in Fig. 4.9(a) [34]

$$Z_{\mathrm{s}}^{\mathrm{TE,Mesh}} = \frac{j\omega\eta_0 D}{2c\pi} \ln\csc\left(\frac{\pi w}{2D}\right) , \tag{A.2.5}$$

$$Z_s^{\mathrm{TM,Mesh}} = \frac{j\omega\eta_0 D}{2c\pi} \ln\csc\left(\frac{\pi w}{2D}\right)\left(1 - \frac{\sin^2\theta_s}{\varepsilon_r + 1}\right) . \tag{A.2.6}$$

These expressions are same as that of the vertical strips (Eqs. A.1.1 and A.1.2).

### A.2.2 Jerusalem cross array

For the Jerusalem cross as shown in Fig. 4.14(b) [40, 41]

$$Z_s^{\mathrm{TE,JC}} = j\omega L_g^{\mathrm{TE}} + \frac{1}{j\omega C_g} , \tag{A.2.7}$$

$$Z_s^{\mathrm{TM,JC}} = j\omega L_g^{\mathrm{TM}} + \frac{1}{j\omega C_g} , \tag{A.2.8}$$

where

$$L_g^{\mathrm{TE}} = \frac{\eta_0 D}{2c\pi} \ln \csc\left(\frac{\pi w}{2D}\right)\left(1 - 2\frac{\sin^2\theta_s}{\varepsilon_r + 1}\right) , \tag{A.2.9}$$

$$L_g^{\mathrm{TM}} = \frac{\eta_0 D}{2c\pi} \ln \csc\left(\frac{\pi w}{2D}\right) , \tag{A.2.10}$$

$$C_g = \frac{\varepsilon_0 \varepsilon_r d}{\pi}\left[\ln \csc\left(\frac{\pi g}{2D}\right) + F\right] , \tag{A.2.11}$$

with

$$F = \frac{\sqrt{1 - \left(\frac{d}{\lambda}\right)^2}\, u^2}{1 + \sqrt{1 - \left(\frac{d}{\lambda}\right)^2}\,(1-u)^2} + \left[\frac{du(3u-2)}{4\lambda}\right]^2 , \tag{A.2.12}$$

$$u = \cos^2\left(\frac{\pi g}{2d}\right) , \tag{A.2.13}$$

$$\lambda = \frac{2\pi}{k_0\sqrt{\left(\frac{\varepsilon_r + 1}{2}\right)}} . \tag{A.2.14}$$

### A.2.3 Cross dipole array

For the cross dipole arrays, shown in Fig. 4.14(c) [42],

$$Z_s^{\mathrm{TE,Dipole}} = j\omega L_g^{\mathrm{TE}} + \frac{1}{j\omega C_g} , \tag{A.2.15}$$

$$Z_s^{\mathrm{TM,Dipole}} = j\omega L_g^{\mathrm{TM}} + \frac{1}{j\omega C_g} , \tag{A.2.16}$$

where $L_g^{\mathrm{TE}}$, $L_g^{\mathrm{TM}}$ are given by Eqs. A.2.9 and A.2.10, and

$$C_g = \frac{1}{\left(\frac{1}{C} - \frac{0.3595 l_{\mathrm{eff}}^2}{\varepsilon_0\left(\frac{\varepsilon_r + 1}{2}\right)D^3}\right)} , \tag{A.2.17}$$

with

$$C = \frac{\pi\varepsilon_0\varepsilon_{\mathrm{eff}} l}{4\ln\left(\frac{4l}{w}\right)} , \tag{A.2.18}$$

and $l$ being twice as large as the dipole's effective length, $l_{\mathrm{eff}}$.

### A.2.4 Patch array

For the patch array structure (as shown in Fig. 4.14(a)), which is obtained by considering the mesh grid array and then applying the approximate Babinet principle, results in the capacitive grid impedance of the complementary structure (i.e., array of printed square patches) [34]

$$Z_s^{\text{TE,Patch}} = \frac{\eta_0^2}{2\left(\varepsilon_r + 1\right) Z_s^{\text{TM,Mesh}}} \ , \tag{A.2.19}$$

$$Z_s^{\text{TM,Patch}} = \frac{\eta_0^2}{2\left(\varepsilon_r + 1\right) Z_s^{\text{TE,Mesh}}} \ , \tag{A.2.20}$$

with $Z_s^{\text{TM,Mesh}}$, and $Z_s^{\text{TE,Mesh}}$ given by Eqs. A.2.6 and A.2.5.

### A.2.5 Slotted Jerusalem cross and slotted cross dipole arrays

Similarly, the slotted Jerusalem cross and slotted cross dipole arrays (shown in Figs. 4.9(b) and 4.9(c)), are obtained by considering the array of printed Jerusalem crosses and cross dipoles, and by employing the approximate Babinet principle, the grid impedances can be written as,

$$Z_s^{\text{TE,Slot JC}} = \frac{\eta_0^2}{2\left(\varepsilon_r + 1\right) Z_s^{\text{TM,JC}}} \ , \tag{A.2.21}$$

$$Z_s^{\text{TM,Slot JC}} = \frac{\eta_0^2}{2\left(\varepsilon_r + 1\right) Z_s^{\text{TE,JC}}} \ , \tag{A.2.22}$$

$$Z_s^{\text{TE,Slot Dipole}} = \frac{\eta_0^2}{2\left(\varepsilon_r + 1\right) Z_s^{\text{TM,Dipole}}} \ , \tag{A.2.23}$$

$$Z_s^{\text{TM,Slot Dipole}} = \frac{\eta_0^2}{2\left(\varepsilon_r + 1\right) Z_s^{\text{TE,Dipole}}} \ , \tag{A.2.24}$$

where $Z_s^{\text{TM,JC}}$, $Z_s^{\text{TE,JC}}$, $Z_s^{\text{TM,Dipole}}$, and $Z_s^{\text{TE,Dipole}}$ are given by Eqs. A.2.8, A.2.7, A.2.16, and A.2.15.

# VITA

Yashwanth Reddy Padooru was born in Hyderabad, India, in 1985. He received Bachelors of Technology in Electronics and Communications Engineering from Jawaharlal Nehru Technological University (JNTU), Hyderabad, India in 2006. In 2006 he joined the Department of Electrical Engineering at the University of Mississippi, and received M.S. degree in 2009. From 2009-2012, he worked as a research assistant and pursed Ph.D. degree.

His research interests include electromagnetic wave interaction with wire media, absorbers, periodic structures, and cloaking structures. Mr. Padooru has contributed to over twenty peer reviewed technical journal and conference publications. He is the recipient of the 2012 National Radio Science Fellowship Award for the paper presentation in URSI conference held in Boulder, Colorado. He also received the Summer Research Assistantship from the Graduate School during the summer of 2012. While doing his PhD, he worked as an intern at Intel Corporation, California from May 2011 to Nov. 2011.

# Publications List

## Book Chapters

[B1] A. B. Yakovlev, Y. R. Padooru, G. W. Hanson, C. S. R. Kaipa, "Multilayered wire media: generalized additional boundary conditions and applications," InTech Publishers (In press).

## Journal Publications

[J1] A. B. Yakovlev, Y. R. Padooru, G. W. Hanson, A. Mafi, and S. Karbasi, "A Generalized Additional Boundary Condition for Mushroom-Type and Bed-of-Nails-Type Wire Media," *IEEE Trans. on Microw. Theory Tech.*, Vol. 59, No. 3, March 2011.

[J2] Y. R. Padooru, A. B. Yakovlev, C. S. R. Kaipa, F. Medina, and F. Mesa, "Circuit modeling of multiband high impedance surface absorbers in the microwave regime," *Phys. Rev. B*, Vol. 84, 035108, July 2011.

[J3] C. S. R. Kaipa, A. B. Yakovlev, G. W. Hanson, Y. R. Padooru, F. Medina, and F. Mesa, "Enhanced transmission with a graphene-dielectric microstructure at low-terahertz frequencies," *Phys. Rev. B*, Vol. 85, 245407, June 2012.

[J4] Y. R. Padooru, A. B. Yakovlev, C. S. R. Kaipa, G. W. Hanson, F. Medina, F. Mesa, and A. W. Glisson, "New Absorbing Boundary Conditions and Homogenization Model for Multilayered Mushroom-Type Metamaterials: Applications to Wideband Absorbers," (*Accepted in IEEE Trans. on Antennas Propagat.*).

[J5] Y. R. Padooru, A. B. Yakovlev, P. Y. Chen, and A. Alù , "Analytical modeling of conformal mantle cloaks for cylindrical objects using sub-wavelength printed and slotted arrays," *J. Appl. Phys*, Vol. 112, 034907, August 2012.

[J6] Y. R. Padooru, A. B. Yakovlev, P. Y. Chen, and A. Alù, "Line-Source Excitation of Realistic Conformal Metasurface Cloaks," *J. Appl. Phys*, Vol. 112, 104902, November 2012.

[J7] Y. Mao, Y. R. Padooru, K. F. Lee, A. Z. Elsherbeni, and F. Yang, "Aperture Coupled and Stripline Feed Rectangular Patch Antennas with Adjustable Air Gap," (*Under Review*).

## Conference Abstracts and Proceedings

[C1] Y. R. Padooru, A. B. Yakovlev, P. Y. Chen, and A. Alu, "Analytical modeling of conformal metasurface mantle cloaks for cylindrical objects," 2012 *Metamaterials*, St. Petersburg, Russia, September 17-22, 2012.

[C2] Y. R. Padooru, A. B. Yakovlev, C. S. R. Kaipa, G. W. Hanson, F. Medina, F. Mesa, and A. W. Glisson, "Generalized Additional Boundary Conditions and Analytical Model for Multilayered Mushroom-Type Wideband Absorbers," 2012 *IEEE AP-S Symposium and USNC/URSI National Radio Science Meeting*, Chicago, Illinois, USA, 8-14 July 2012.

[C3] Y. R. Padooru, A. B. Yakovlev, P. Y. Chen, and A. Alu, "Mantle Cloaking Using Sub-Wavelength Conformal Metallic Meshes and Patches," 2012 *IEEE AP-S Symposium and USNC/URSI National Radio Science Meeting*, Chicago, Illinois, USA, 8-14 July 2012.

[C4] C. S. R. Kaipa, A. B. Yakovlev, G. W. Hanson, Y. R. Padooru, F. Medina, and F. Mesa, "Low-Terahertz Transmissivity and Broadband Planar Filters using Graphene-Dielectric Stack," 2012 *IEEE AP-S Symposium and USNC/URSI National Radio Science Meeting*, Chicago, Illinois, USA, 8-14 July 2012.

[C5] A. B. Yakovlev, M. G. Silveirinha, S. I. Maslovski, C. S. R. Kaipa, P. A. Belov, G. W. Hanson, O. Luukkonen, I. S. Nefedov, C. R. Simovski, S. A. Tretyakov, and Y. R. Padooru, "Recent Advances in the Homogenization Theory of Wire Media with Applications at Microwaves, THz, and Optical Frequencies," 2012 *IEEE AP-S Symposium and USNC/URSI National Radio Science Meeting*, Chicago, Illinois, USA, 8-14 July 2012.

[C6] Y. R. Padooru, A. B. Yakovlev, C. S. R. Kaipa, G. W. Hanson, F. Medina, F.

Mesa, and A. W. Glisson, "Absorbing Boundary Conditions and Homogenization Model for Multilayered Wire Media," 2012 *USNC/URSI National Radio Science Meeting*, CO, USA, 4-7 Jan. 2012.

[C7] Y. R. Padooru, A. B. Yakovlev, C. S. R. Kaipa, F. Medina, and F. Mesa, "Multi-band High-Impedance Surface Absorbers with a Single Resistive Sheet: Circuit Theory Model," 2011 *IEEE AP-S Symposium and USNC/URSI National Radio Science Meeting*, Washington, USA, 3-8 July 2011.

[C8] Y. Mao, Y. R. Padooru, K. F. Lee, A. Z. Elsherbeni, and F. Yang, "Stripline and Aperture Coupled Feed Rectangular Patch Antennas with Air Gap," 2011 *IEEE AP-S Symposium and USNC/URSI National Radio Science Meeting*, Washington, USA, 3-8 July 2011.

[C9] C. S. R. Kaipa, A. B. Yakovlev, F. Medina, F. Mesa, and Y. R. Padooru, "Sub-wavelength Transmission Through Stacked Two-dimensional Metallic Patches: A Circuit Model Perspective," 2011 *IEEE AP-S Symposium and USNC/URSI National Radio Science Meeting*, Washington, USA, 3-8 July 2011.

[C10] A. B. Yakovlev, G. W. Hanson, A. Mafi, Y. R. Padooru, and S. Karbasi, "Modal Propagation on Thin Metal Mushroom-Type Surfaces in the Transition to Bed-of-Nails-Type Wire Media," 2011 *IEEE AP-S Symposium and USNC/URSI National Radio Science Meeting*, Washington, USA, 3-8 July 2011.

[C11] P. Nayeri, Y. R. Padooru, F. Yang, A. B. Yakovlev, and A. Z. Elsherbeni, "Sub-wavelength Multi-layer Elements for Broadband Reflectarray Antennas," 2010 *IEEE AP-S Symposium and CNC-USNC/URSI Radio Science Meeting*, Toronto, Canada, 11-17 July 2010.

[C12] A. B. Yakovlev, Y. R. Padooru, S. Karbasi, G. W. Hanson, and A. Mafi, "Non-local Homogenization Model for the Analysis of Absorbing Properties of Mush-room Structures with Graphene Patches at Microwaves," 2010 *IEEE AP-S Symposium and CNC-USNC/URSI Radio Science Meeting*, Toronto, Canada, 11-17 July 2010 (invited paper to special session).

[C13] A. B. Yakovlev, C. S. R. Kaipa, Y. R. Padooru, F. Medina, and F. Mesa, "Dynamic and Circuit Theory Models for the Analysis of Sub-wavelength Transmission Through Patterned Screens," *Third International Congress on Advanced Electromagnetic Materials in Microwaves and Optics* Metamaterials 2009, London, UK, 30 Aug. - 4 Sep. 2009.

[C14] A. B. Yakovlev, C. S. R. Kaipa, Y. R. Padooru, F. Medina, and F. Mesa, "Sub-wavelength Transmission Through Multilayered Arrays of Patches/Slots: Analytical and Circuit Theory Models," *USNC/URSI National Radio Science Meeting*, Charleston, SC, USA, 1-5 June 2009.